A COLD Vacuum Chamber for Beam Heat Load DIAGnostics (COLDDIAG)

Zur Erlangung des akademischen Grades eines
DOKTORS DER NATURWISSENSCHAFTEN
von der Fakultät für Physik
des Karlsruher Instituts für Technologie (KIT)

genehmigte

DISSERTATION

von

Dipl.–Phys. Stefan Gerstl
aus München

Tag der mündlichen Prüfung : 22.11.2013
Referent : Prof. Dr. Tilo Baumbach
Korreferent : Prof. Dr. Anke–Susanne Müller

Contents

1

Chapter 1

Introduction

In 1947 the first observation of synchrotron radiation at the General electric research laboratory opened up the possibility to produce high energy X-rays [1]. Although the first spectroscopy experiments with soft X-rays were carried out by D. Tomboulian and P. Hartmanit in 1956, it was not before the 1960s that scientists in the USA, Europe and Asia started to use synchrotron radiation for their experiments [2]. At this time, synchrotron radiation was mainly seen as an unwanted side effect limiting the energies of electrons and positrons in the storage rings of particle accelerators used for collision experiments. These "first generation" synchrotron light sources only allowed parasitic use of the generated light. While most first generation light sources were upgraded to allow the use of the generated radiation, in 1981, the first "second generation" facility, which was dedicated to the production of synchrotron radiation, started operation in Daresbury, UK [3]. Second generation light sources primarily produce synchrotron light using bending magnets which guide the electron around the storage ring leaving only short straight sections between the magnets. In these straight sections, so-called insertion devices consisting of an array of several dipole magnets can be installed to generate X-rays with shorter wavelength and higher intensities. The European Synchrotron Radiation Facility (ESRF) in Grenoble, France began user operation in 1994 as the first synchrotron of the "third generation". The ESRF uses bending magnets with a smaller bending radius and longer straight sections between the magnets, allowing the installation of a large number of different kinds of insertion devices. With the growing demand for light with short wavelengths and higher intensities for investigating smaller objects and faster time–resolved measurements e.g. in soft condensed matter, nanoscience or noncrystalline structural biology [4, 5], the requirements for peak magnetic fields and field quality of the insertion devices are growing at the same time. Superconducting insertion devices and particularly undulators, open up the possibility of higher magnetic fields for a given vacuum gap and period length compared with the state of the art in-vacuum permanent magnet undulators [6] and even cryogenic permanent magnet devices [7–9]. A superconducting undulator installed at the Ångströmquelle Karlsruhe (ANKA) in March 2005 was the first cold-bore superconducting undulator installed and tested at an electron storage ring [10, 11]. The beam induced heat load observed in this device was much higher than expected from theoretical predictions taking into account synchrotron radiation from upstream bending magnets and wake field effects due to geometrical and resistive wall impedance [12, 13]. The discrepancy of the beam heat load calculated from theory compared to experimental results obtained at ANKA, as well as with the superconducting wigglers installed at MAX II and at the Diamond Light Source (DLS) [14] is still not understood. This is why at ANKA the decision was made to build a cold vacuum chamber for beam heat load diagnostics (COLDDIAG) with the aim of measuring the beam heat load and the hope of gaining a deeper understanding of the underlying mechanisms [14]. In this thesis the development of the experimental setup, the measurement layout and the first measurements and results of COLDDIAG are presented. This work is structured in six chapters, which are composed as follows.

After this introduction, the second chapter presents the fundamentals of synchrotron light sources and especially the DLS, and the magnetic structures used to produce synchrotron radiation. In addition, the advantages as well as the technical challenges of superconducting insertion devices are described.

The third chapter introduces the possible beam heat load sources, namely synchrotron radiation from upstream bending magnets, geometrical and resistive wall impedance along with electron and/or ion bombardment.

The fourth chapter focuses on the experimental setup and starts with the experimental challenges followed by the vacuum and cryogenic layout, the diagnostics, the control system and data acquisition and concludes with the changes made between the first and the second installation of COLDDIAG at the DLS.

In the fifth chapter the measurements and analysis beginning with the beam heat load for different beam conditions, including variable beam current, bunch length, beam position and fill pattern are presented. Additionally, the flux and energy spectrum of electrons impinging on the chamber walls and the influence of a solenoidal field on these particles as well as the total pressure and residual gas content during the installation period is shown.

The work closes with a summary of the experiments performed before providing an outlook on future measurements and possible improvements of COLDDIAG.

2

Chapter 2

Fundamentals

The following chapter starts with a short introduction to synchrotron light sources. The devices used to produce synchrotron radiation, including bending magnets and insertion devices (IDs) are also introduced. Insertion devices create radiation with higher flux, higher brilliance and eventually different polarizations with respect to bending magnets. Section three focuses on the advantages of superconducting insertion devices, in particular of undulators. Subsequently, the challenges and questions still to be solved regarding design and construction of superconducting undulators are addressed.

2.1 Synchrotron light sources

Nowadays synchrotron light sources can be divided into two groups, storage rings and free electron lasers. This thesis focuses on storage rings. The stored particles are generated and then accelerated in a linear accelerator and/or a booster synchrotron before being injected into the storage ring. Here the particles are guided on a roughly circular path by focusing and deflecting magnets. Due to the the deflection of the particles, they emit synchrotron radiation. The radiated power from one particle can be written as [15]:

$$P_0 = \frac{(Ze^2)c}{6\pi\varepsilon_0 R^2}\frac{E^4}{(m_0c^2)^4} \tag{2.1}$$

with e the electron charge and Z the number of charges, c the speed of light, ε_0 the vacuum permittivity, as well as the bending radius R, the particle energy E and the rest mass m_0. The fourth-power dependence of the radiated power on the rest mass of the charged particle explains why only electrons and in some cases positrons are used to produce synchrotron radiation. The power lost by the beam on each turn is recovered by a voltage oscillating in the radio frequency (RF) range. The RF-frequency used is an integer multiple of the revolution frequency, so that a particle traveling around the storage ring always sees an accelerating voltage. Because of the RF-system, the particles are not homogeneously distributed in the storage ring, but packed into so-called bunches. The spacing between two subsequent bunches is also defined by the RF-frequency. The ratio of revolution frequency to RF-frequency is the harmonic number of a synchrotron. The harmonic gives the number of segments, which can be filled with bunches. These segments are normally referred to as buckets. Storage rings are classified in two groups. While in second generation light sources synchrotron radiation is mainly produced by bending magnets, third generation light sources use so-called insertion devices (IDs), installed in straight sections between the bending magnets.

Diamond Light Source

An example of a third generation light source is the Diamond Light Source (DLS) which is located on the Harwell Science and Innovation Campus in the UK. The DLS is a 3 GeV storage ring currently with a maximum beam current of 350 mA [16]. The machine circumference is 561.6 m which is divided into 24 cells, comprising arcs and straight sections to be equipped with insertion devices. The installed RF-system works at a frequency of 500 MHz [17]. The storage ring has in total 936 buckets, where normally 900 are filled with electrons. The DLS storage ring runs in user operation for 24 h and 6 days per week. During this time the beam conditions are kept as constant as possible to provide a stable radiation source for the experimental stations. However, due to collisions with residual gas molecules in the beam pipe or defocusing effects from electric and magnetic fields, electrons get lost and the beam current decays. To maintain a constant beam current, DLS operates in top-up mode. This means that the amount of lost electrons is reinjected typically every 10 min [18, 19]. After each user run a machine development day is scheduled. This time is used for small maintenance work and experiments, which cannot be performed during user operation.

2.2 Synchrotron radiation sources

In third generation light sources, different magnetic structures are used to produce radiation from a stored beam. Depending on the required energy, intensity and brilliance, the radiation is generated either by bending magnets, wigglers or undulators.

2.2.1 Bending magnets

In circular machines, dipole magnets are used to guide the electron beam on its path around the storage ring. While being deflected, the electrons emit a wide fan of light with continuous spectrum. The vertical opening angle of the synchrotron radiation is $\approx 1/\gamma$, where gamma is the Lorentz factor. Compared to wigglers and undulators, bending magnets radiate the lowest photon flux. Figure 2.1 shows a typical bending magnet and radiation fan. A useful parameter to compare different bending magnet sources is the

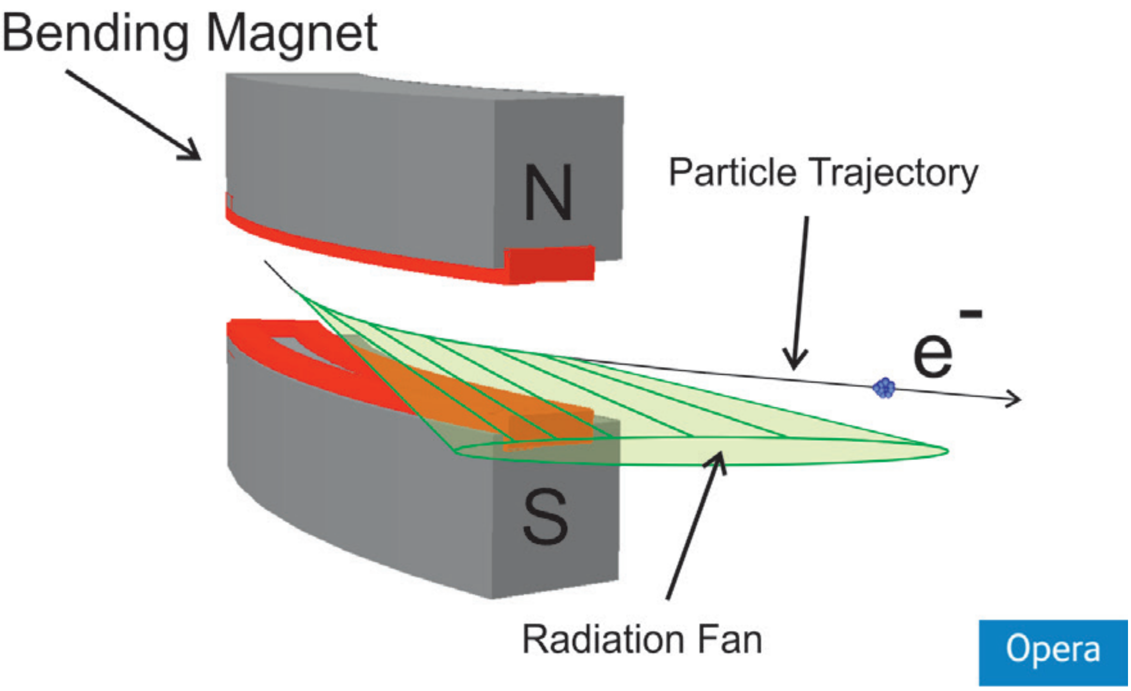

Figure 2.1: Schematic view of a bending magnet and radiation fan.

critical frequency ω_c or critical energy E_c, which divides the power spectrum into two equal parts [20]:

$$\omega_c = \frac{3c\gamma^3}{2R} \qquad \text{and} \qquad E_c = \hbar\omega_c = \frac{3hc\gamma^3}{4\pi R} \tag{2.2}$$

where h is the Planck constant and $\hbar = h/2\pi$. Figure 2.2 shows a comparison of the typical spectra of a bending magnet, a wiggler and an undulator.

2.2.2 Wigglers

Wigglers can be described as a linear array of alternating dipole magnets. At each pole, the electron gets deflected by the magnetic field and emits synchrotron radiation. The radiated flux sums up and thus scales with the number of poles. An electron on its path around the storage ring sees a sinusoidal field generated by the wiggler and starts to oscillate. The angular deflection caused by the field can be described as:

$$\dot{x}(s) = \frac{B_0 e}{m_0 c} \frac{\lambda_u}{2\pi} \frac{1}{\gamma} \cos\left(\frac{2\pi s}{\lambda_u}\right) \tag{2.3}$$

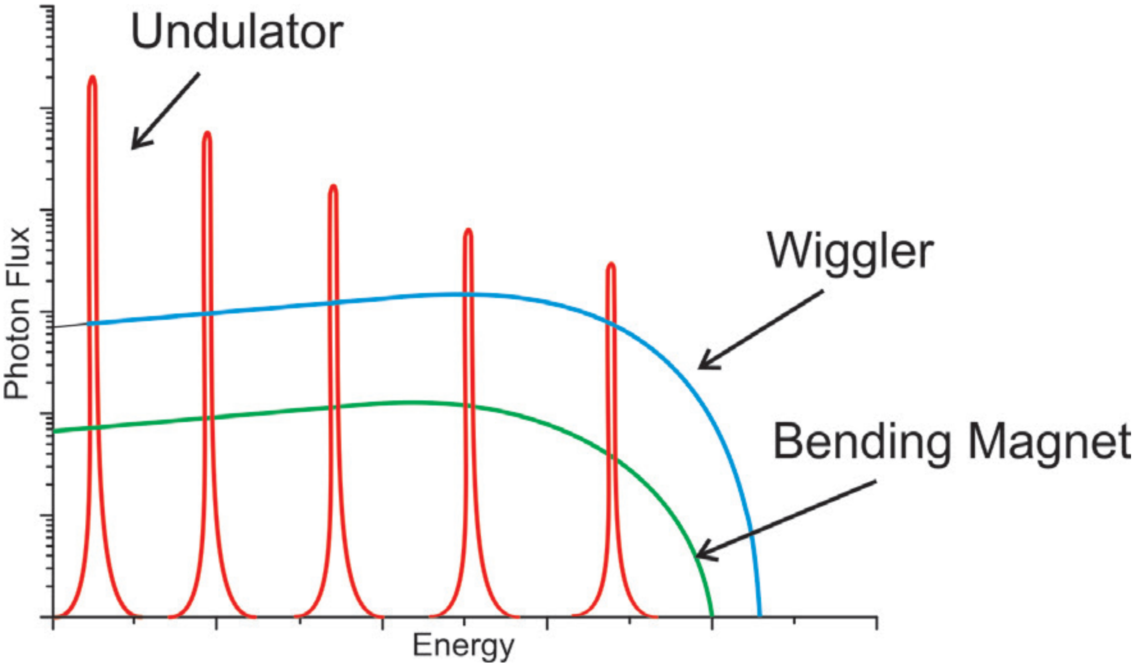

Figure 2.2: Schematic spectra of a bending magnet, a wiggler and an undulator.

with s the position along the beam axis, B_0 the peak magnetic field at the pole, e the electron charge, m_0 the rest mass and λ_u the period length of the sinusoidal magnetic field. By defining the so–called deflection parameter [21]:

$$K = \frac{B_0 e}{m_0 c} \frac{\lambda_u}{2\pi} \tag{2.4}$$

the maximum deflection can be written as

$$\dot{x}(s) = \frac{K}{\gamma}. \tag{2.5}$$

For a $K > 1$ the angular deflection becomes larger than the opening angle of the radiation $\approx 1/\gamma$. Hence the radiation cones emitted at each magnet of the linear array do not overlap anymore [20]. This results in a continuous spectrum similar to a bending magnet and a horizontally enlarged radiation cone. Figure 2.3 shows a schematic array of magnets used for a wiggler. The typical shape of a photon spectrum from a wiggler can be found in Fig. 2.2. Compared with bending magnets, wigglers offer a higher energy and flux of the emitted radiation. In addition, unlike the fixed magnetic field of a bending magnet, the magnetic field and period length and thus the produced radiation of the wiggler can be adjusted to the needs and limitations of the experimental stations.

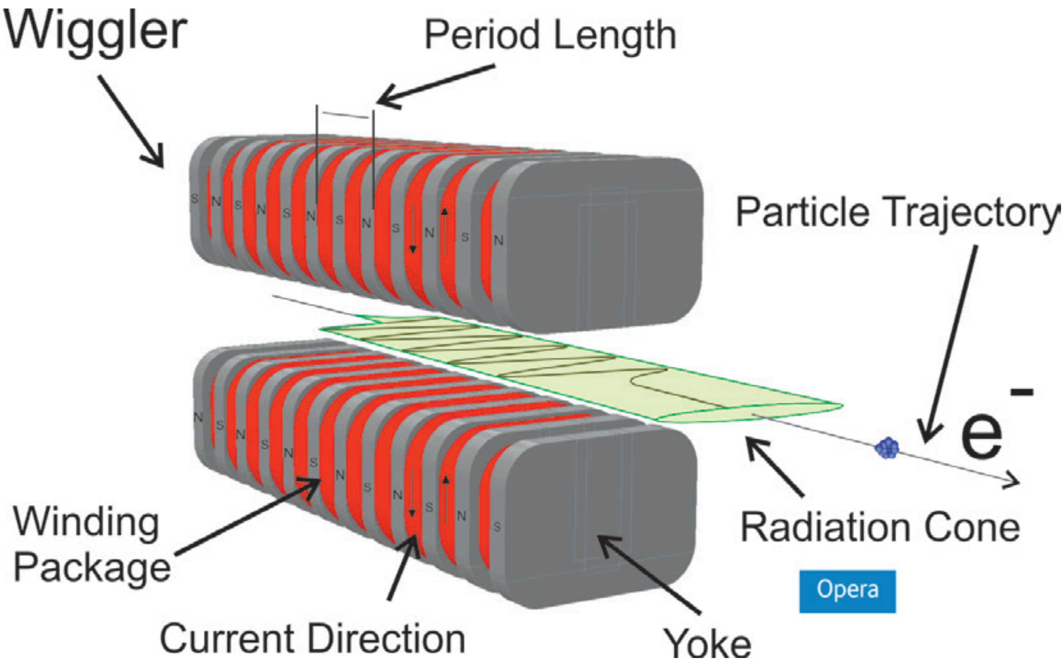

Figure 2.3: Schematic view of an wiggler and of it's radiation cone.

2.2.3 Undulators

Undulators are similar to wigglers and consist of a series of dipole magnets with alternating magnetic fields. In contrast to wigglers, the emitted radiation from the oscillating electrons interferes constructively because of the smaller deflection angle. The resulting spectrum of the radiated light shows a largely enhanced flux and a narrow bandwidth at the harmonic frequencies of the undulator. The wavelength of the emitted radiation at the n^{th} harmonic is given by the undulator equation:

$$\lambda = \frac{\lambda_u}{2n\gamma^2}\left(1 + \frac{K^2}{2} + \Theta^2\gamma^2\right), \tag{2.6}$$

where Θ is the angle between the beam axis and the observer [20]. By changing the magnetic field, which is typically achieved by varying the gap in a permanent magnet device or by changing the electric current in an electromagnetic device, the frequency of the emitted radiation at the different harmonics can be tuned. To fulfill the interference condition, the requirements on the mechanical precision of an undulator are much higher compared with those needed for a wiggler. Figure 2.4 shows a schematic picture of an undulator and Fig. 2.2 the corresponding typical spectrum.

Nowadays most insertion devices in third generation light sources are built using permanent magnets. The demand for insertion devices which produce light with shorter

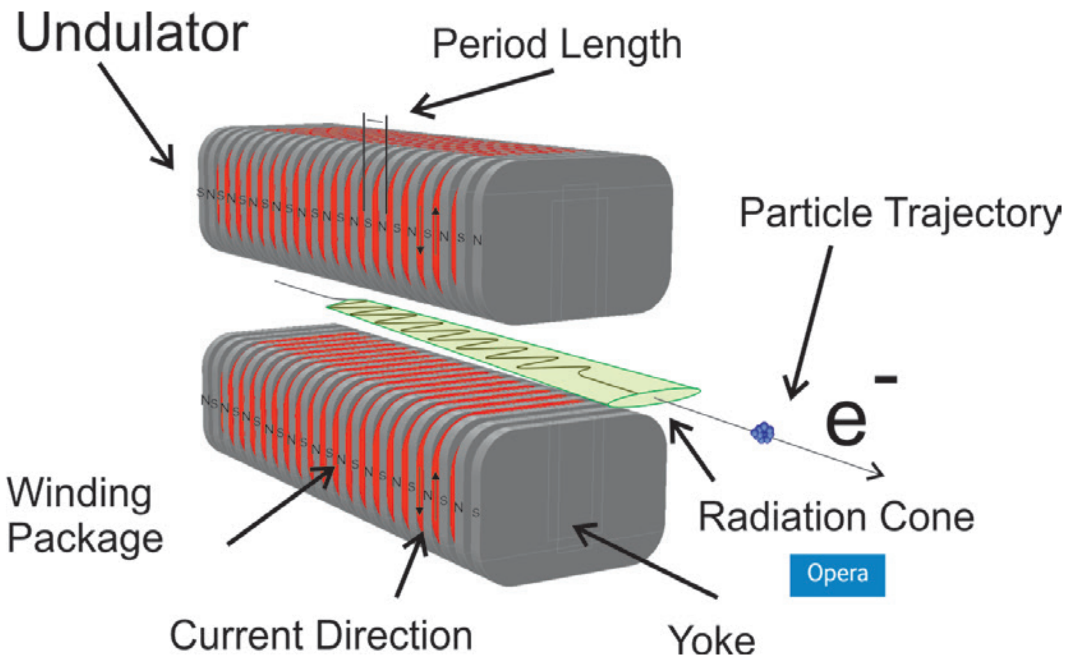

Figure 2.4: Schematic view of an undulator and of it's radiation cone.

wavelengths and higher flux pushes the requirements for new types of insertion devices. At the present the highest peak fields for a given period length are created by cryogenic permanent magnet undulators [22], which are still under development. Similar to the so-called in-vacuum insertion devices in these undulators, the magnets are placed inside the beam vacuum. This makes it possible to reduce the magnetic gap and increase the magnetic field strength as no intermediate vacuum vessel is needed. In addition, the magnets are cooled to around 140 K which further increases the peak magnetic field [22]. Another possibility to increase the peak magnetic, which is presented in the next section is using superconducting coils.

2.3 Superconducting insertion devices

In superconducting insertion devices the permanent magnets are replaced by superconducting coils. The advantages and technical challenges, as well as the open issues are addressed in the following.

2.3.1 Advantages

Superconducting insertion devices open up the possibility to reach higher magnetic fields for a given vacuum gap and period length compared to permanent magnet undulators [6] and even cryogenic permanent magnet undulators [7–9]. This provides an increase in flux and extends the spectrum to higher energies opening up the possibility for storage rings with energies of the order of 3 GeV to reach photon energies in the hard X-ray regime.

In addition, permanent magnet devices can suffer from partial or total demagnetization when exposed to high doses of hard X-rays. Radiation damage has been reported by the Advanced Photon Source (APS) in Argonne, where two small vacuum gap devices show a loss in peak magnetic field [23] and by the European Synchrotron Radiation Facility (ESRF) in Grenoble [24], where two insertion devices have accidentally been irradiated and demagnetized during the commissioning phase of the machine. Radiation damage can be a problem, especially for high energy storage rings and free electron lasers (FELs). Although the FEL group in Stanford reported that superconducting magnets can quench under exposure of electron showers, the quench sensitivity depends on different parameters like field margin and intensity of the shower [24]. The only objection concerning permanent damage of superconducting IDs is the possible degradation of the epoxies or other organic materials which are most commonly used to fix the wire position of the superconducting coil [25]. However, the radiation resistance of many organic materials has been investigated e.g. at CERN for the Large Electron Positron Collider (LEP) as well as for the Large Hadron Collider(LHC) both at room temperature and at cryogenic temperatures [26, 27].

2.3.2 Technical challenges and open issues

Although a lot of progress has been made concerning the development of superconducting undulators [9, 10, 28], some technical issues still need to be solved.

Shimming concepts, which are used to compensate for magnetic field errors and improve the field quality, are difficult to apply to superconducting undulators. Although several approaches have been proposed [29–32], a working concept has not been developed yet. Therefore, high requirements on the mechanical tolerances of the winding and the yoke, as well as on the assembly of the magnets are required. At the same time, the restrictive tolerances achieved at room temperature have to be maintained during cool down over the full length of the magnet.

Additionally, precise measurements of the field quality at around 4 K, in vacuum and in small bores, are much more complex than measurements in air and at room temperature. No commercial system is available and several instruments are under development [33, 34].

Another main difficulty for the development of superconducting insertion devices is the necessity to keep the superconducting coils at a constant temperature of around 4 K to operate the magnets with a safety margin below the critical curve determined by the critical current surface. Especially for a conduction cooled system or a system with small liquefaction capacity, the known heat intake from the beam deposited on the cold beam tube is crucial for the cryogenic layout. In March 2005, a cryogen free cold bore undulator was installed at the storage ring of the Ångströmquelle Karlsruhe (ANKA)[10, 35]. The beam induced heat load observed in this device was higher than expected and resulted in a higher operating temperature of the coils, which reduced the magnetic performance. Possible beam heat load sources are synchrotron radiation from upstream bending magnets, wakefield effects due to geometrical and resistive wall impedance and electron and/or ion bombardment [12, 36]. The discrepancy of the beam heat load calculated from theory compared to experimental results obtained at ANKA, as well as with the superconducting wigglers installed at MAX II and at the DLS [14] is still not understood. This is why at ANKA the decision was made to build a cold vacuum chamber for beam heat load diagnostics (COLDDIAG) [14].

3

Chapter 3

Beam heat load sources

Among the possible sources for the beam heat load are synchrotron radiation from upstream magnets, wake field effects and electron and/or ion bombardment. In the following, the different underlying mechanisms of these sources of beam heating are described.

3.1 Synchrotron radiation from upstream bending magnets

In storage rings, superconducting insertion devices are typically installed in straight sections. These straight sections are enclosed by two bending magnets, one upstream and one downstream. The upstream bending magnet radiates a large fan of synchrotron radiation tangentially to the direction of flight of the circulating particle. Thereby, part of the insertion device which is on the outside of the storage ring, can be located in this radiation fan. The power emitted by a bending magnet per mrad of arc and integrated over all vertical angles is given by [37]

$$P_s = \frac{eI}{10^3 6\pi\varepsilon_0}\frac{\gamma^4}{R}, \tag{3.1}$$

where e is the charge, I the average beam current, ε_0 the vacuum permittivity, γ the Lorentz factor and R the bending radius of the magnet. Equation 3.1 shows the linear dependence of the radiated power with respect to the beam current. For an electron beam at the DLS with an energy of 3 GeV, average current of 300 mA and a bending radius of 7.15 m, the total radiated power is about 300.7 kW, which corresponds to $P_s = 47.9\,\mathrm{W/mrad}$. Assuming a point–like uniform electron beam, the angular power distribution in the vertical can be calculated using [37, 38]:

$$\frac{\partial P}{\partial \psi} = P_s \frac{21}{32}\frac{\gamma}{(1+\gamma^2\psi^2)^{5/2}}\left[1 + \frac{5}{7}\frac{\gamma^2\psi^2}{(1+\gamma^2\psi^2)}\right]. \tag{3.2}$$

Here ψ is the vertical opening angle between the horizontal plane defined by the particle motion and the observation point. In order to screen insertion devices from the hard X-ray radiation produced by the upstream bending magnet, a collimator system is normally installed. However, reflected synchrotron radiation can still shine onto the cold section of the insertion device. The amount of reflected synchrotron radiation hitting the cold chamber walls depends on the geometry of the beam pipe in front of the ID, the collimator, but also on the material and on the roughness of the surfaces. The complex geometry and surface properties of the different materials used in the beam pipe make it very difficult to evaluate the influence of reflected synchrotron radiation on the beam heat load.

3.2 Geometrical and resistive wall impedance

Another source of beam induced heating is the electromagnetic interaction of the beam with the surrounding chamber. In the time domain, this interaction is referred to as wake fields and as impedance in the frequency domain. Wake fields and impedance are related to each other by a Fourier transform [39, 40]. For a circular machine, the energy loss per turn or the power loss of a single bunch can be expressed in general as [36, 41]:

$$P_{loss_b} = I_b^2 \sum_{n=-\infty}^{\infty} ReZ_{||}\left(n\omega_0\right) \left|S\left(n\omega_0\right)\right|^2, \tag{3.3}$$

where I_b is the bunch current, $\omega_0 = 2\pi/T_0$ is the revolution frequency and $S\left(n\omega_0\right)$ is the frequency spectrum of the bunch. $ReZ_{||}$ is the real part of the longitudinal impedance. For a Gaussian bunch profile, S can be written as

$$S\left(n\omega_0\right) = exp\left(-\frac{(n\omega_0)^2\sigma_z^2}{2c^2}\right). \tag{3.4}$$

In the case where the time between the bunches is much longer than the bunch duration, assuming N_b identical and equally spaced bunches and in the absence of resonant modes, the sum can be replaced by an integral and Eq. 3.3 can be transformed to [36]:

$$P_{loss} = \frac{I^2}{N_b \pi f_0} \int_0^{\infty} ReZ_{||}(\omega) exp\left\{(-\frac{\sigma_z}{c})^2\omega^2\right\} d\omega, \tag{3.5}$$

where I is the average beam current. Commonly, one distinguishes resistive impedance from geometrical impedance. Resistive impedance is caused by the resistance of the chamber walls, whereas geometrical impedance is caused by changes of the beam pipe cross–section like steps, gaps, tapers or surface roughness. In contrast to the heat load caused by synchrotron radiation, heat coming from geometrical and resistive wall impedance depends on I^2/N_b in the absence of resonances, and shows a strong dependence on the bunch length (see Eq. 3.5 and Eq. 3.7). In the next section more details of geometrical and resistive impedance are given.

3.2.1 Geometrical impedance

Geometrical impedance is caused by changes of the beam pipe geometry like steps, gaps, tapers and surface roughness. The electric field generated in the vacuum chamber walls by a point–like charge traveling with a velocity of $v \approx c$ is contracted in the direction of flight. In the limit $v \to c$ the field of the particle is given by a ring with zero angular spread [42]. Every time the diameter or the shape of the beam pipe is changed, the particle changes and usually loses energy. This energy is given by the amount of work required to change the charge distribution in the chamber walls. A charged particle trailing within a short distance is affected by the field of the leading one and correspondingly changes its energy [40, 42]. By knowing the longitudinal impedance $ReZ_{||}$, the power loss per turn of all particles can be calculated using Eq. 3.5. From literature analytical expressions and approximations of $ReZ_{||}$ can be found for many geometrical problems including steps, tapers, gaps, cavities [40, 43]. Although the exact surface properties of the beam pipe are difficult to determine, there are different approaches for including the influence of the beam power loss due to surface roughness [36, 44–46]. The values for the power which can be obtained from analytical formulas are in good agreement with simulations performed with CST PARTICLE STUDIO [36]. However, not all of the power dissipated by the beam is directly converted into heat. An unknown fraction of the power is reflected in the forward or backward direction into the beam pipe. In addition, the power can also be transferred to other bunches. Therefore, an exact determination of the heat intake from geometrical impedance is not possible, but an upper limit can be given [36, 47].

3.2.2 Resistive impedance

Resistive impedance is caused by the surface resistance of the chamber walls. According to the theory of image charges, the particle beam generates an image current with the opposite charge in the chamber walls. This current produces heat in the beam pipe due to the electrical resistance. In a synchrotron, the surfaces seen by the beam are mostly made from stainless steel or aluminum. Copper, with its high electrical conductivity is used whenever low amount of resistive wall heating is desired. For resistive wall heating the longitudinal impedance is given by [48]

$$ReZ_{||}(\omega) = \frac{L}{l} R_s, \tag{3.6}$$

where L is the length of the vacuum chamber, l the circumference of the beam pipe and R_s is the surface resistance of the beam pipe. Equation 3.5 can now be written as

$$P_{wall} = \frac{L}{\pi l} \frac{I^2}{N_b f_0} \int\limits_0^\infty exp\left\{ (\frac{\sigma_z}{c})^2 \omega^2 \right\} R_s(\omega) d\omega. \tag{3.7}$$

The high velocity of the particles leads to short revolution times and thus high frequencies of the current. Therefore, for highly energetic particles the skin effect needs to be taken into account [48]. The skin depth is given by

$$\delta(\omega) = \sqrt{\frac{2\rho}{\mu_0 \mu_r \omega}}, \tag{3.8}$$

with ρ the D.C. resistance of the material, μ_r the relative permeability and μ_0 the vacuum permeability. In case of normal skin effect, the surface resistance can be written as

$$R_s = \frac{\rho}{\delta} = \sqrt{\frac{\mu_0 \mu_r \omega}{2}}. \tag{3.9}$$

The mean free path of an electron inside a bulk metal is given by [49]

$$l = \frac{1}{2} \frac{ne^2}{m_e v_F \rho} \tag{3.10}$$

where n is the number of electrons in the metal, ρ the resistance and $v_F = \sqrt{2E_F/m}$ the Fermi velocity with E_F the Fermi energy of the metal. The RRR value is defined as the ratio between the resistance at room temperature and the residual resistance at very low temperatures, where only the impurities in the material contribute to the resistance and the lattice contribution can be neglected [50]

$$RRR \simeq \frac{\rho_{300K}}{\rho_{4K}} \qquad \text{and thus} \qquad l_{4K} \simeq RRR \cdot l_{300K}. \tag{3.11}$$

Typically the RRR value for electroplated copper on stainless steel which is used for the beam pipe in the superconducting ID at ANKA and MAX-II, are between 10 and 200 [37, 51]. For low temperatures and conducting materials with high purity as used in cold bore insertion devices, the mean free path length l of the electrons in the material becomes larger then the skin depth. As a consequence, only a small fraction of the electrons with a velocity almost parallel to the surface contributes to the conduction of the A.C. current [52]. The underlying theory of this phenomena, the anomalous skin effect, was developed by H. London [53], A. B. Pippard [52], E. H. Sondheimer and G. E. H. Reuter [54] and R. Chambers [55]. The surface resistance in the anomalous skin effect regime can be expressed as

$$R_s = R_\infty (1 + 1.157\alpha^{-0.276}) \text{ , for } \alpha \geq 3 \tag{3.12}$$

with

$$\alpha = \frac{3}{2} \left(\frac{l_{4K}}{\delta_{4K}} \right)^2 = \left(\frac{3}{4} \omega \mu_r \mu_0 (\rho l)^2 \rho_{4K}^{-3} \right) \tag{3.13}$$

and

$$R_\infty = \left(\frac{\sqrt{3}}{16\pi} \rho l (\omega \mu_r \mu_0)^2 \right)^{\frac{1}{3}} . \tag{3.14}$$

In a real device, the conductivity and therefore the RRR value of the beam tube or the copper coating is normally not directly measured. However, by using the anomalous skin effect theory, the range and the dependency can be given for the contribution of resistive wall heating to the overall heat load of a cold bore insertion device.

3.3 Electron and/or ion bombardment

In addition to synchrotron radiation and wake field effects, electron and/or ion bombardment are also possible sources of beam induced heating. In the ultra high vacuum chamber of a storage ring, the gases with non–negligible partial pressure are typically H_2, H_2O, CO, CO_2 and CH_4 [13]. In superconducting insertion devices, the beam pipe is normally at a temperature of around 4-20 K to minimize thermal radiation to the coils. At these temperatures, the beam pipe acts as an efficient cryopump. The origin of the cryopumped gases are either molecules from the surface oxide which were desorbed by energetic particles like photons, electrons or ions, or residual gas molecules from adjacent room temperature parts of the storage ring. These physisorbed molecules are only loosely bound by Van der Waals forces with binding energies of a few meV. Particles with kinetic energies of only a few eV are needed to desorb the molecules covering the surface. In the literature this repeated process of desorption and adsorption is called ‘recycling‘ [56]. Taking into account this recycling process, the cryosorbed surface layers are potentially a large source of particles. In an electron storage ring some molecules in the gas phase can be ionized by photons produced by direct or reflected synchrotron radiation, or by the electron beam directly. The electrons and ions created are repelled or attracted by the beam and accelerated towards the chamber walls. By hitting the walls they either desorb other particles or deposit some heat.

A phenomenon which was first detected at machines with positive particle beams, but later also observed in electron machines, is the electron cloud [57–59]. In the case where the secondary emission yield (SEY) of the electrons becomes greater than one, i.e., for one incident particle more than one electron is released from the chamber walls, an avalanche like effect is created. This localized effect leads in the worst case to beam instabilities [58] which have up to now only been observed in machines with positive beams. The electron cloud build up has a large influence on the local gas distribution and is a source of electrons which can again impinge on the chamber walls. These electrons possibly contribute to the heating process of the cold beam tube [59]. A rough estimate of the heat deposited onto the chamber walls by electrons or ions is given in Eq. 3.15 to 3.20.

For a round beam traveling in the center of a circular beam pipe the electric field [60] can be expressed as

$$E(r) = \frac{\lambda}{2\pi\varepsilon_0 r} \tag{3.15}$$

where r is the radial position and ε_0 the vacuum permittivity. λ is the line charge of the bunch, given by

$$\lambda = \frac{eN_p}{c\tau} \tag{3.16}$$

with the bunch duration τ and the number of particles per bunch

$$N_p = \frac{IT_0}{qN_b} \tag{3.17}$$

for I the average beam current, T_0 the revolution time and N_b the number of bunches. The momentum transfer from one passing bunch to a stationary particle with distance r [12, 60] can be written as

$$\mathit{\Delta} p = qE(r)\tau = \frac{qeN_b}{2\pi\varepsilon_0 cr}. \tag{3.18}$$

and the corresponding energy increase of the particle, of of mass m is given by

$$\mathit{\Delta} W = \frac{\mathit{\Delta} p^2}{2m}. \tag{3.19}$$

As a relatively simple approximation, the power induced by particle bombardment to the chamber can be assumed as the energy gained from the momentum kick of the bunch times $\dot{N}$ the number of particles hitting the walls per unit time [12]

$$P_{bomb} \approx \mathit{\Delta} W \cdot \dot{N} = \frac{I^2 T_0^2}{N_b^2} \frac{\left(\frac{q}{2\pi\varepsilon_0 cr}\right)^2}{2m} \cdot \dot{N}. \tag{3.20}$$

Equation 3.19 shows that the energy gain of the particle is inversely proportional to the particle mass. This involves that only electrons or positrons can effectively contribute to the beam heat load and the contribution of the much heavier ions can be neglected. The dependence on the various beam parameters is unknown and strongly affected by the interaction of the bombarding particles with the electromagnetic fields created by the beam, which still needs to be understood.

Chapter 4

4 Experimental setup

In the context of superconducting insertion device development at ANKA, the issue of measuring and investigating the beam heat load from the electron beam has been addressed. A cold vacuum chamber for diagnostics (COLDDIAG) was designed and manufactured together with the company Babcock Noell GmbH [61]. With the wide range of instruments, including temperature sensors, pressure gauges and residual gas analysers, as well as retarding field analysers, it is possible to measure the beam heat load, total pressure and gas content, as well as the flux of charged particles hitting the chamber walls. COLDDIAG was installed in the Diamond Light Source (DLS) in November 2011. After only one week of operation it had to be removed. It was installed again with some modifications in August 2012. Figure 4.1 shows COLDDIAG installed in straight 8 of the storage ring of the DLS shortly after the second installation. In this chapter, first the major challenges concerning the design and instrumentation setup are described, then the vacuum and cryogenic layout, installed diagnostics, and changes after the first installation.

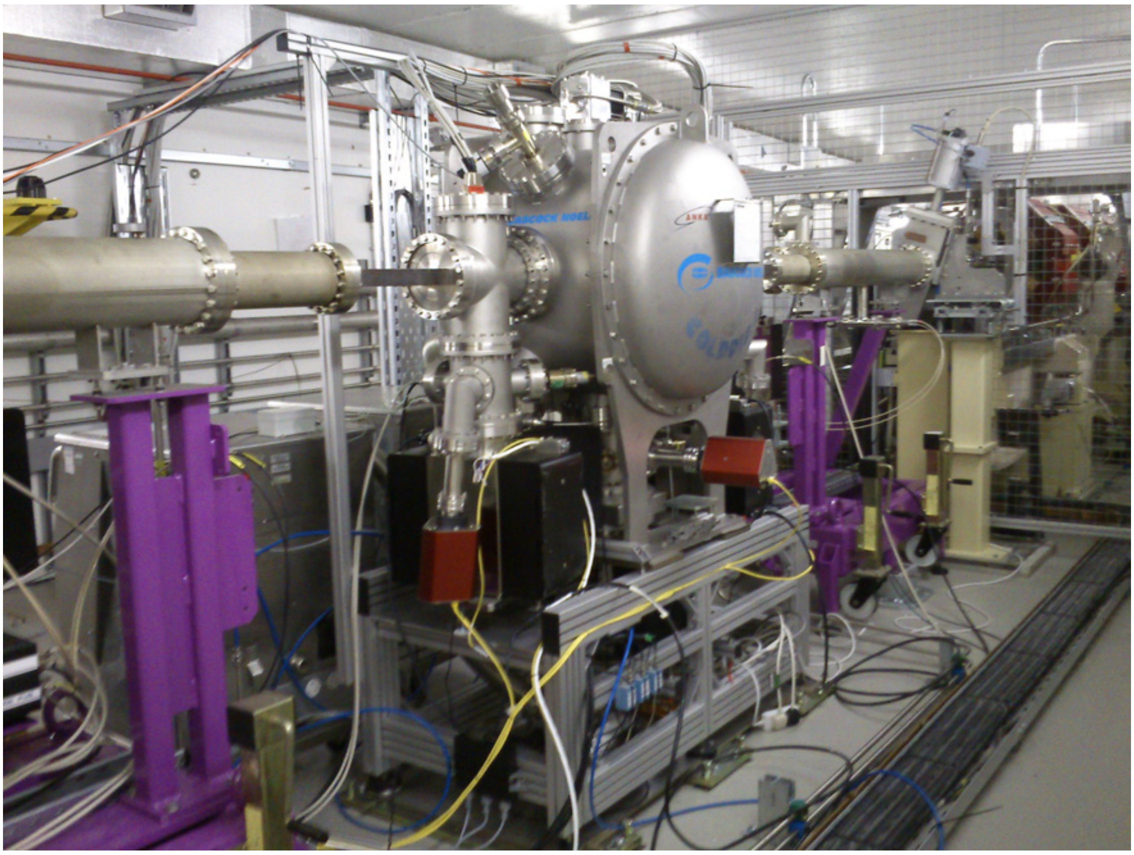

Figure 4.1: COLDDIAG experiment installed in straight 8 of the DLS storage ring in August 2012.

4.1 Experimental challenges

Some basic points about the cryostat and the installed diagnostics of COLDDIAG had been fixed in an early stage of the experiment. The cryostat should fulfill the following requirements (see Fig. 4.2):

- The cryostat should be a cryogen-free system with an operating temperature around 4 K and the possibility to operate at higher temperatures up to 300 K.
- The length should be about 1.4 m to fit in one of the two short straight sections at ANKA.
- The cold liner section in the cryostat should be situated between two warm sections with identical geometry and instrumentation.
- The beam pipe should be exchangeable to test different geometries and materials and to allow installation in other storage rings.

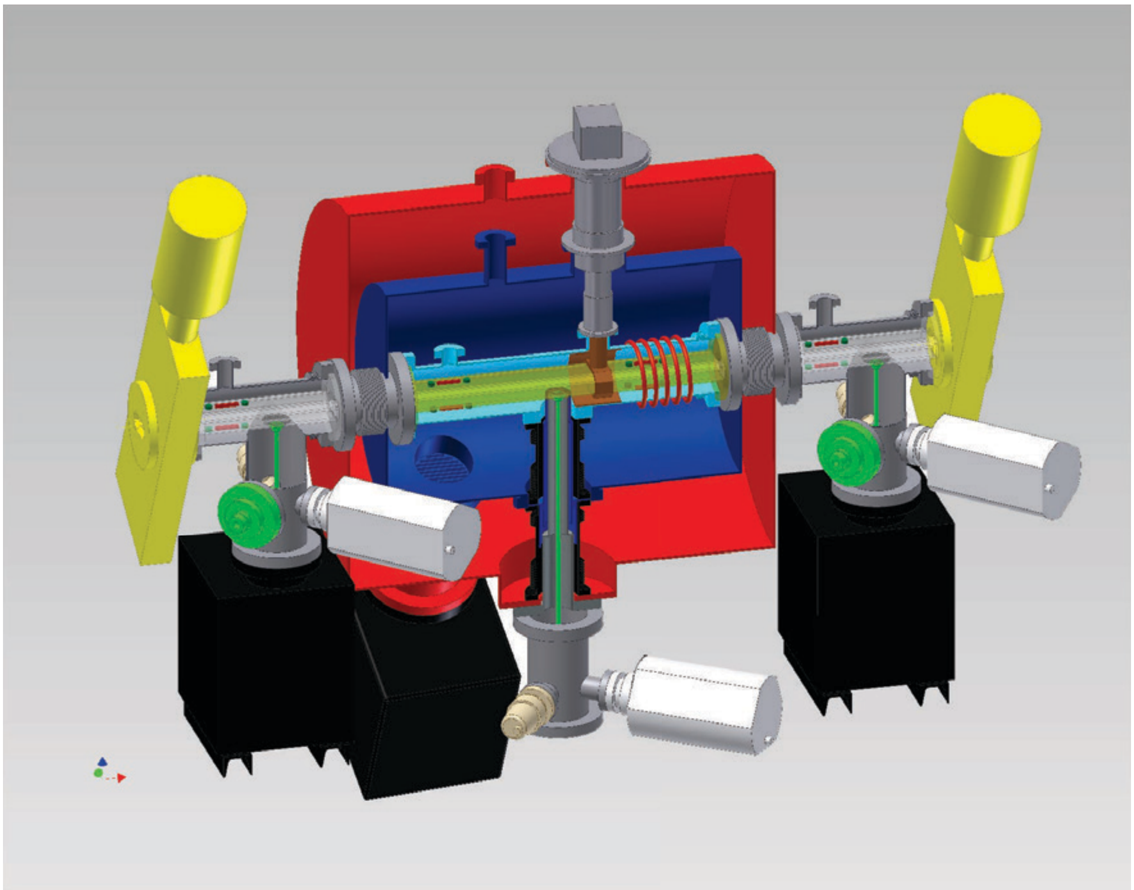

Figure 4.2: First sketch of the COLDDIAG experimental setup. A more detailed overview is presented in the following figures.

- For the measurements at ANKA the gap of the vacuum pipe was aimed to be 25 mm [14].

The diagnostic instrumentation should include:

- Temperature sensors and heaters to measure the beam heat load.
- Pressure gauges and residual gas analysers to measure the total pressure and the residual gas composition.
- Retarding field analysers to investigate the flux and possibly the energy of charged particles hitting the chamber walls.
- A precise leak valve to inject different gases and control the surface coverage and composition of the cold liner section [14].

This instrumentation should be present in all three sections of COLDDIAG to simultaneously compare the measurements in the upstream and downstream warm sections with those in the cold section [14].

Because of the limited cooling power of a cryogen-free system on the one hand and limitations on the total length on the other, the thermal transitions in the cryostat had to be relatively short and much thinner than in other cryogenic devices used in synchrotron storage rings. Those limitations on the thermal transition, and the desire to reach a base temperature of the cold liner section in the range of 4 K made it impractical to build the beam pipe in one piece. Thus, several gaps and steps had to be introduced into the beam pipe design. In order to avoid heating effects from geometric impedance which could influence the amount of the measured beam heat load, gaps and steps in the transitions had to be minimized. Analytical calculations [36], which were later confirmed by 3D simulations with CST PARTICLE STUDIO [62], showed that the steps in the warm regions should be smaller than100 µm while those in the cold section should be below10 µm. Reaching these mechanical tolerances was extremely challenging but proved achievable within the central region of ±10 mm horizontally from the beam axis, where most of the image currents are flowing.

The decision to install COLDDIAG at DLS put additional constrains on the materials and instrumentation available to be used in the beam vacuum. In general, the beam vacuum specifications of DLS prohibit the use of all organic materials. Cabling for the sensors and all adhesives had to be specially tested for outgassing under ultra high vacuum (UHV) conditions and in the presence of radiation.

4.2 Vacuum layout

The vacuum system of the COLDDIAG experiment shows two major volumes: the insulation vacuum and the beam vacuum (UHV) (Fig. 4.3). The two spaces will be described in the following section including their properties and purposes.

4.2.1 Insulation vacuum

The volume of the insulation vacuum is hermetically sealed from the beam vacuum and from atmosphere. It surrounds the beam vacuum parts in the cold section to inhibit heat transfer by convection from ambient temperature to the cold parts in COLDDIAG. For practical reasons, the insulation vacuum pressure was targeted to be in the region of 10^{-7} mbar. This allows the use of ion getter pumps, after prepumping the cryostat with a combination of scroll and turbo pumps. In terms of operational safety, ion pumps are advantageous compared to turbo pumps as in case of a malfunction the vacuum is still maintained. In addition, the absence of moving parts further improves the reliability. The separation of the insulation and the beam vacuum and the relatively relaxed requirements on outgassing rates to reach a pressure around 10^{-7} mbar put a lot fewer constrains on the allowable materials and the cleaning processes. The insulation vacuum is pumped with a 150 l/s Varian (now Agilent Technologies [64]) ion pump and reaches a base pressure of 10^{-8} mbar during cold operation with beam.

4.2.2 Synchrotron beam vacuum

The beam vacuum chamber consists of a cold chamber section between two warm sections. Each of the three sections contains a beam pipe that includes the same diagnostic instruments. This liner is made out of an oxygen-free high conductivity copper (OFHC) which is electroplated with 50 µm copper to simulate the beam tube of the superconducting undulator SCU14 at ANKA. For the installation at the DLS, an ellipse with 60 mm horizontal and 10 mm vertical cross-section was chosen for the bore of the beam pipe, which is similar to the liner used in the superconducting wigglers installed at the DLS. In the cold section, the beam vacuum is separated from the insulation vacuum by a six-way DN100 CF stainless steel cross. This cross is supported by threaded rods, which are connected to the insulation vacuum chamber. Bellows between the cryostat and the six-way cross minimize the heat transfer from ambient temperature and allow for thermal shrinkage during cool-down. The bellows through which the beam travels are equipped with RF–fingers. The synchrotron beam vacuum of COLDDIAG reaches a pressure in the range of 10^{-9} mbar.

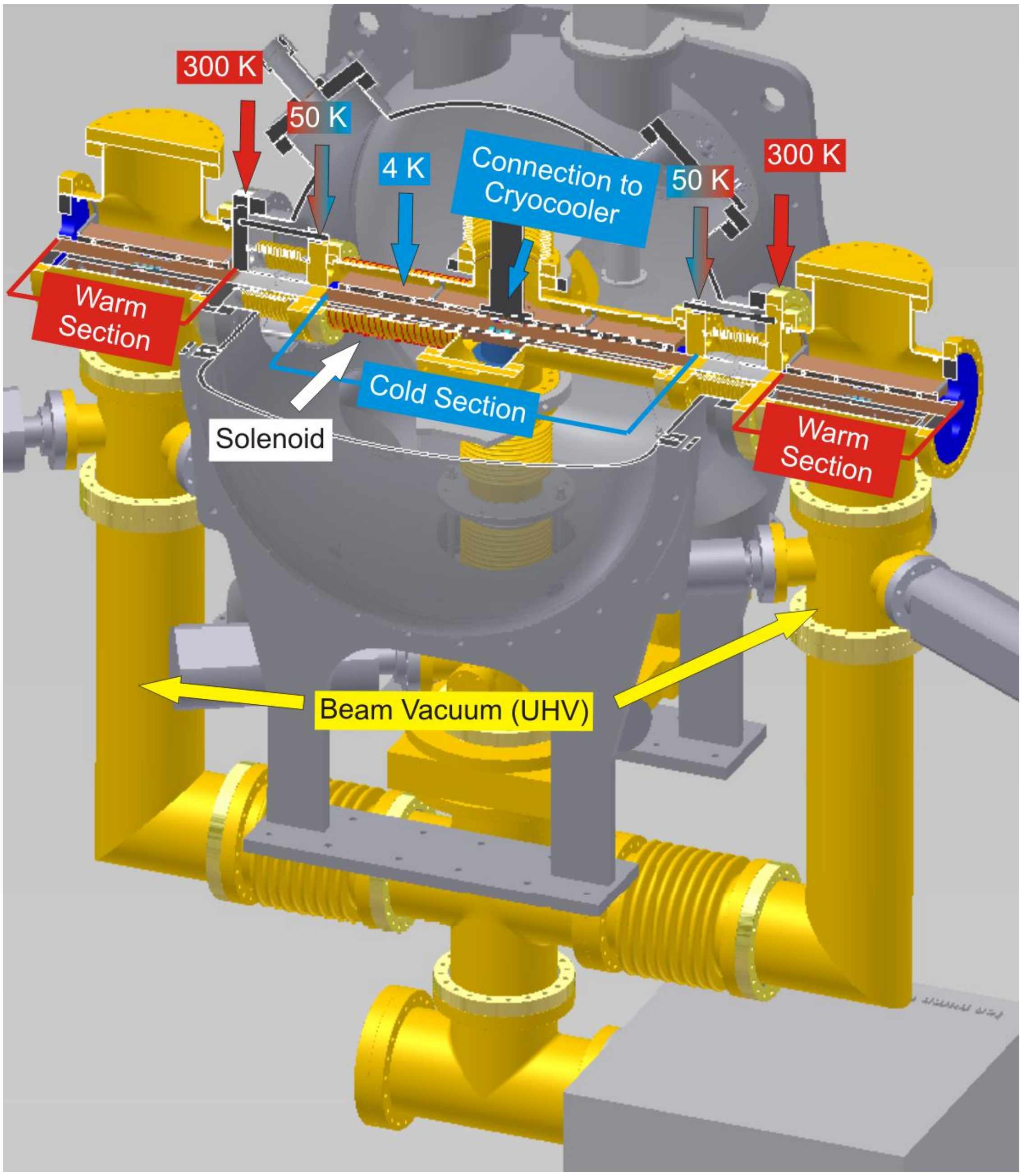

Figure 4.3: Overview of cryostat and vacuum chamber [63].

4.3 Cryogenic layout

To simulate the beam pipe of superconducting insertion devices, the cold liner section of COLDDIAG has to be maintained stable at a specific temperature in the range of 4 - 20 K. COLDDIAG is a cryogen-free system and cooled by one Sumitomo RDK-415D cryocooler. This two-stage Gifford-McMahon cooler has a specified maximum cooling power of 35 W at 50 K on the warm stage and 1.5 W at 4.2 K on the cold stage [65]. The typical cooling power at different operating temperatures provided by the cooler can be seen in Fig. 4.4. As a consequence of the limited cooling power of the conduction cooled system, the heat intake from thermal radiation and conduction must be minimized as much as possible. The following section describes the cryogenic layout and the heat intake path from conduction and radiation. Heat transfer by convection is neglected as it is very efficiently suppressed by the insulation vacuum.

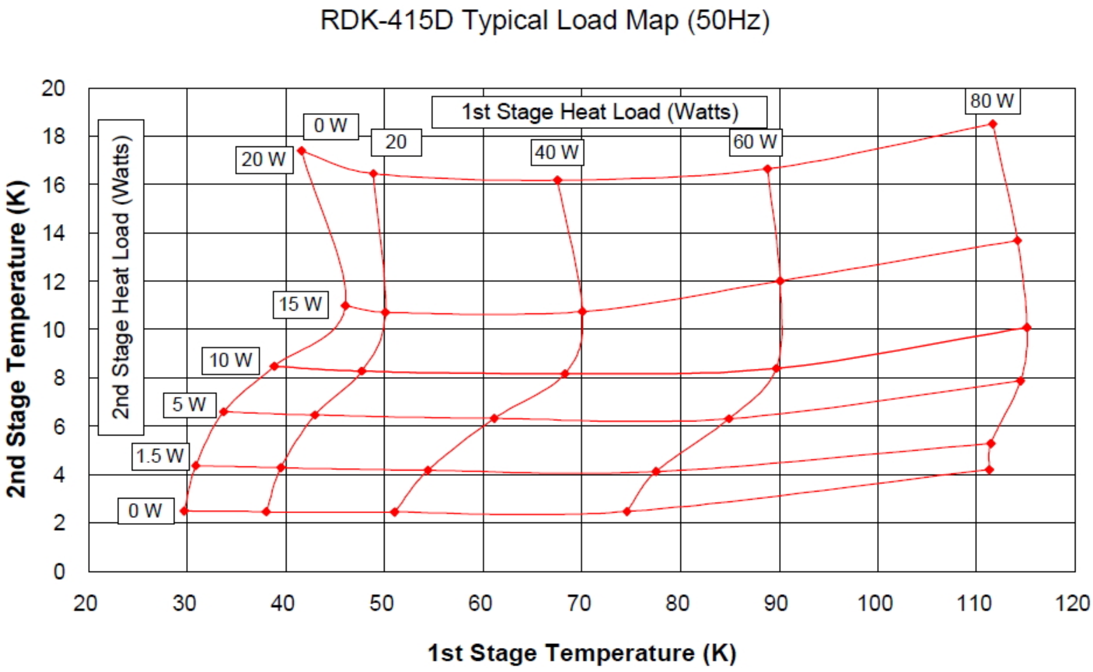

Figure 4.4: Cryocooler load map [65].

4.3.1 Heat intake from thermal radiation

To reduce the heat transfer by means of thermal radiation from the cryostat at ambient temperature to the cold inner surfaces, a shield is installed. This thermal shield screens almost all radiated heat as it is covered with superinsulation. A thermal connection to the the warm stage of the cryocooler allows active cooling of the shield. Another radiation path in COLDDIAG where heat is irradiated to the shield and the cold liner at the same time, is the central diagnostics tube (see Fig. 4.5). The design of this tube is based on the one used for the COLDEX experiment [66] which was installed at the super proton synchrotron (SPS) at the Conseil Européen pour la Recherche Nucléaire (CERN). This tube connects the inside of the cold beam pipe with the residual gas analyser and pressure gauges. To avoid molecules from getting frozen on their way from the beam pipe to the residual gas diagnostic instruments, this tube needs to be at ambient temperature and has to sit as close as possible to the liner without direct contact. Although the radiated heat from this diagnostics tube is reduced by a shield at floating temperature, this warm insert deposits heating power on both the thermal shield and the cold beam pipe. Together with the elliptical apertures on the liner ends, the thermal shield is the main thermal radiation source to the cold beam pipe and the cold stage of the cryocooler.

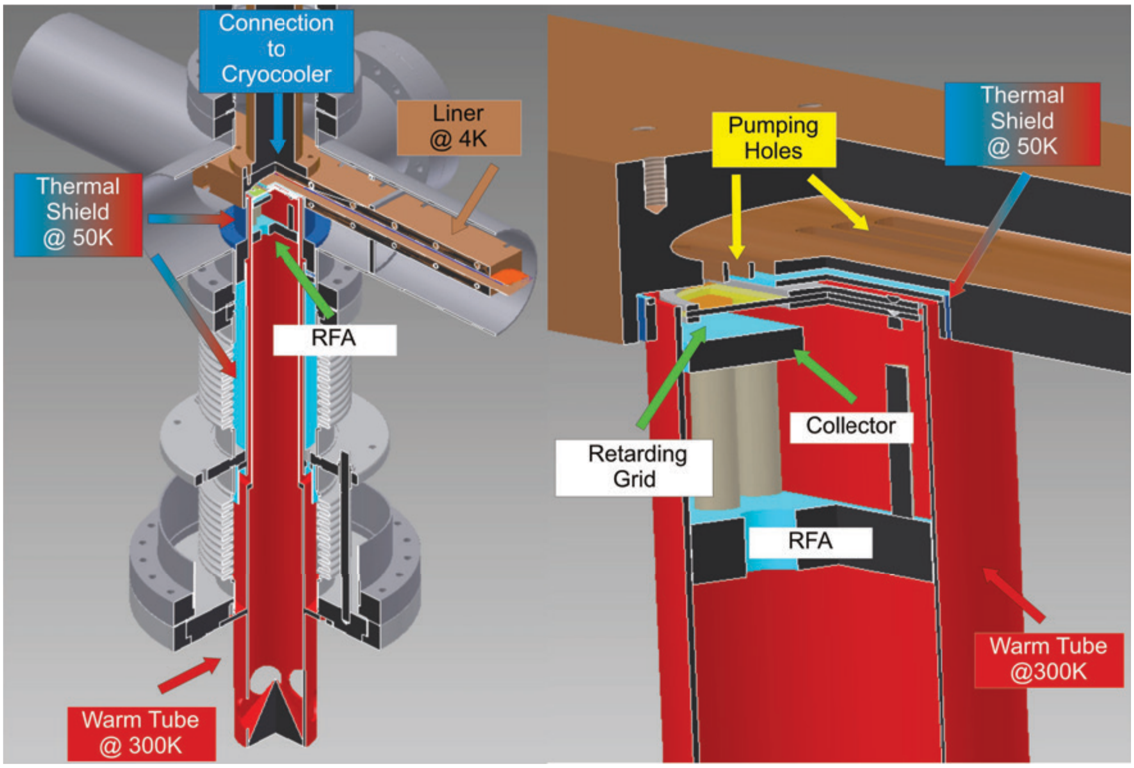

Figure 4.5: Drawing of the diagnotics tube [63].

4.3.2 Heat intake from thermal conduction

Figure 4.6 shows the major components contributing to the heat transfer by means of thermal conduction inside of the cryostat. The outer cryostat vessel and the thermal shield are removed from the drawing for better visibility. The parts of the experiment

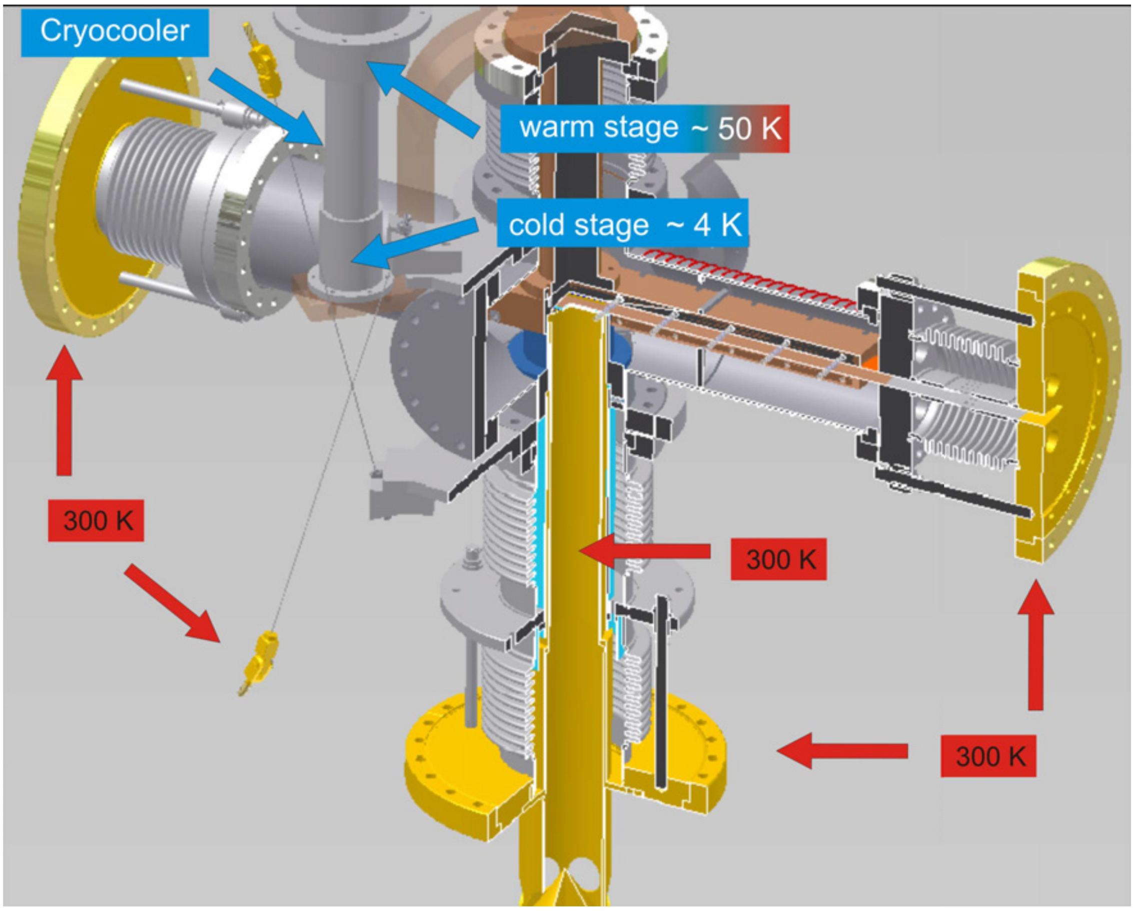

Figure 4.6: Highlighted in yellow are the 300K parts inside the cryostat [63].

which are at ambient temperature are highlighted in yellow. The heat transfer by thermal conduction from the cryostat outside at ambient temperature to the inner beam vacuum tube at 4 K is intercepted at several stages. The inner six-way DN100 CF stainless steel cross, which contains the cold liner section, is supported by eight stainless steel rods and has three connections to the outer part of the cryostat at room temperature.

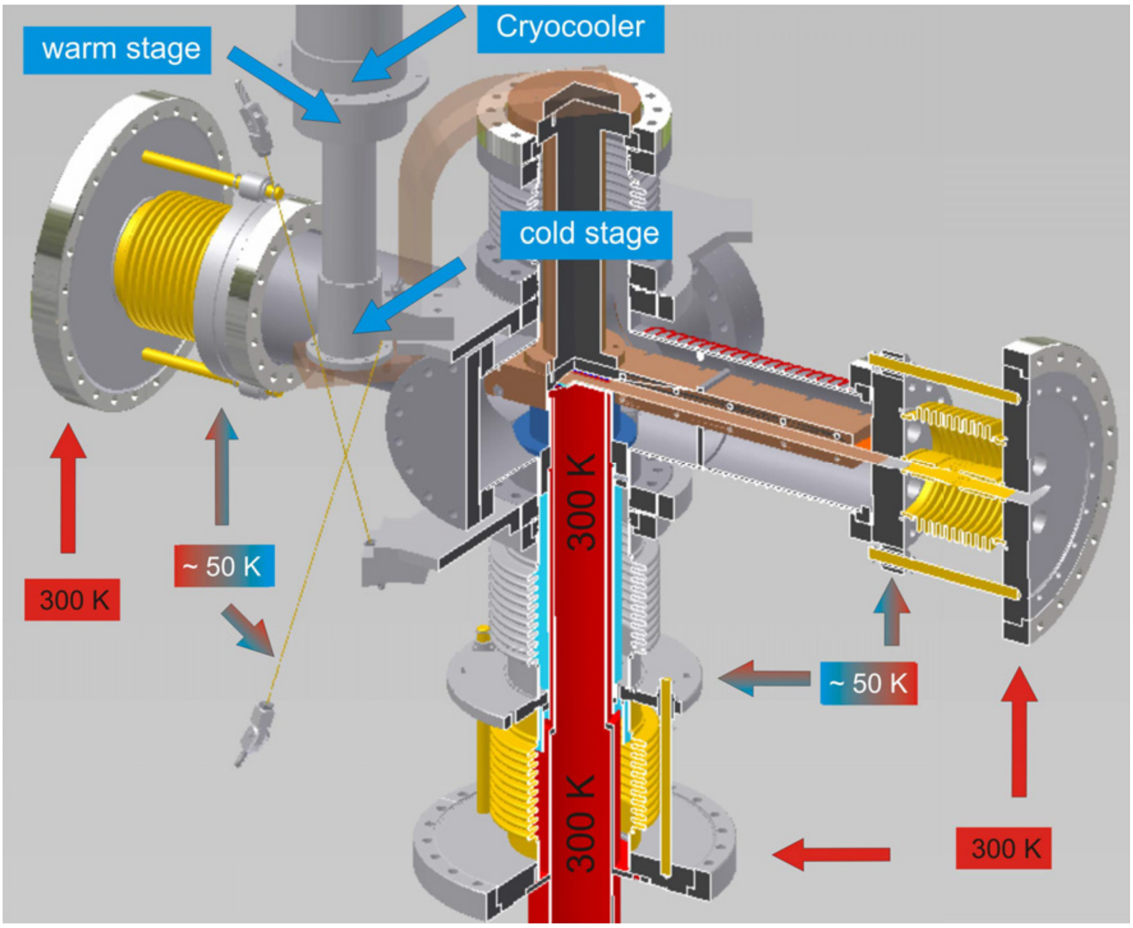

Figure 4.7: Highlighted in yellow are the transition from 300 K to 50 K [63].

The contribution to the heat transfer from ambient temperature to the inside of the cryostat coming from the stainless steel thread rods with a diameter of 2 mm and a length of more than 300 mm, can be neglected. The heat intake from other 300 K components to the inner parts is suppressed by stainless steel bellows (see Fig. 4.7). These bellows compensate the shrinkage of the cold cross during cool–down. In addition, they have a lower thermal conductivity compared to a normal CF pipe because of the thinner material and the longer heat path. The axial bellows are also equipped with RF–fingers to avoid cross–talk between the electric field generated by the electron beam with the periodic structure of the bellows. The RF–fingers also maintain the electrical continuity of the beam pipe needed for the electron beam.

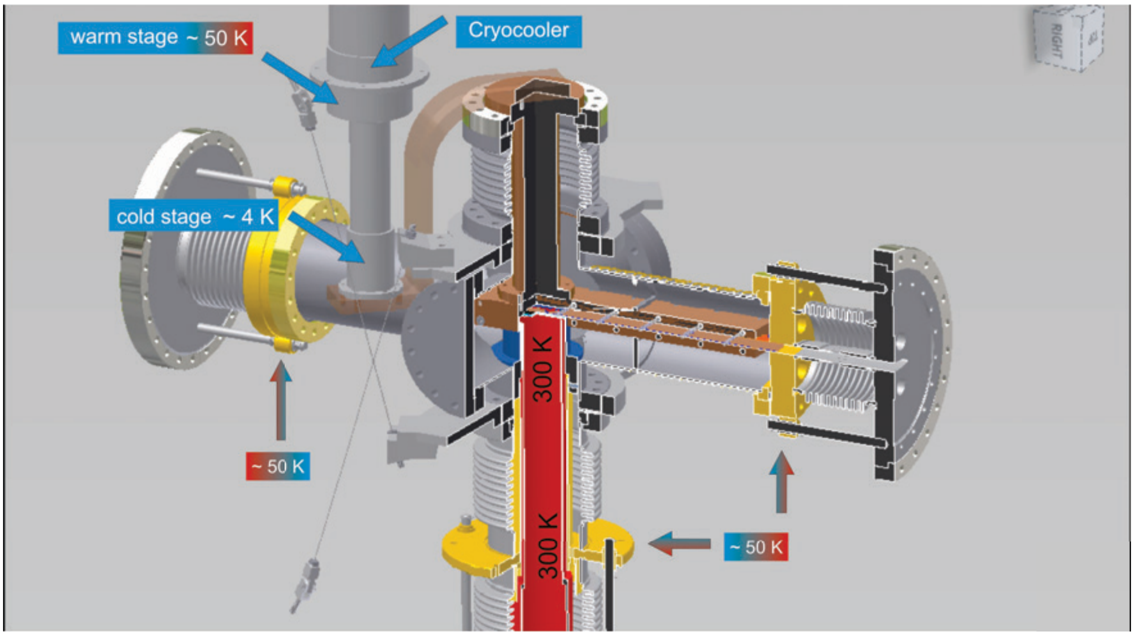

Figure 4.8: Highlighted in yellow are the components connected to the shield at 50 K [63].

To intercept the heat path from the bellows to the colder inner parts, the end of the three bellows are connected to the thermal shield at around 50 K. This can be seen in Fig. 4.8. The thermal shield acts as a heat link and conducts the heat to the warm stage of the cryocooler and out of the cryostat.

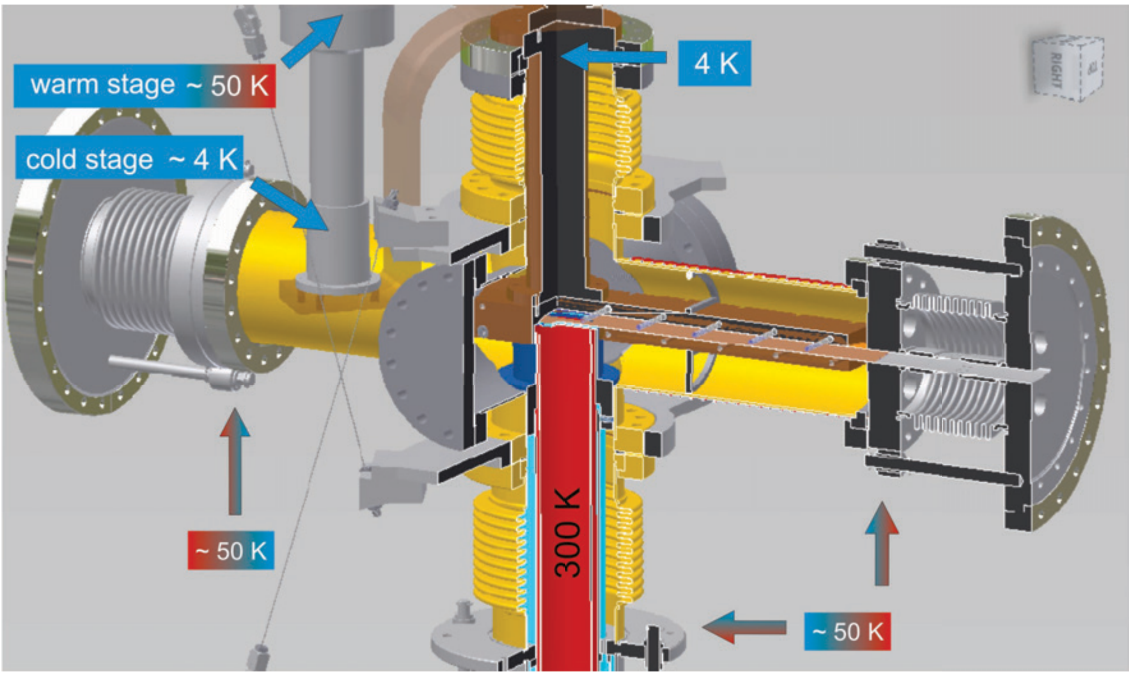

Figure 4.9: Highlighted in yellow are the components at intermediate temperature from 50 K to 4 K [63].

The six-way cross, which contains the cold beam pipe, is connected to the thermal shield as well as to the cold stage of the cryocooler via bellows. The steepest temperature gradient is at both ends of the cold liner section (see Fig. 4.9), where it touches the innner flange of the axial bellows. To minimize the heat transfer, this transition was made out of a 50 µm thin stainless steel foil (see Fig. 4.10). It is covered with 5 µm electro-deposited copper to enhance the electrical conductivity for the image currents of the electron beam. On the warmer side the 20 mm long transition slides inside the flange of the bellows. On the colder side it is glued with a ceramic cement–like glue (Aremco Ceramabond™ 571).

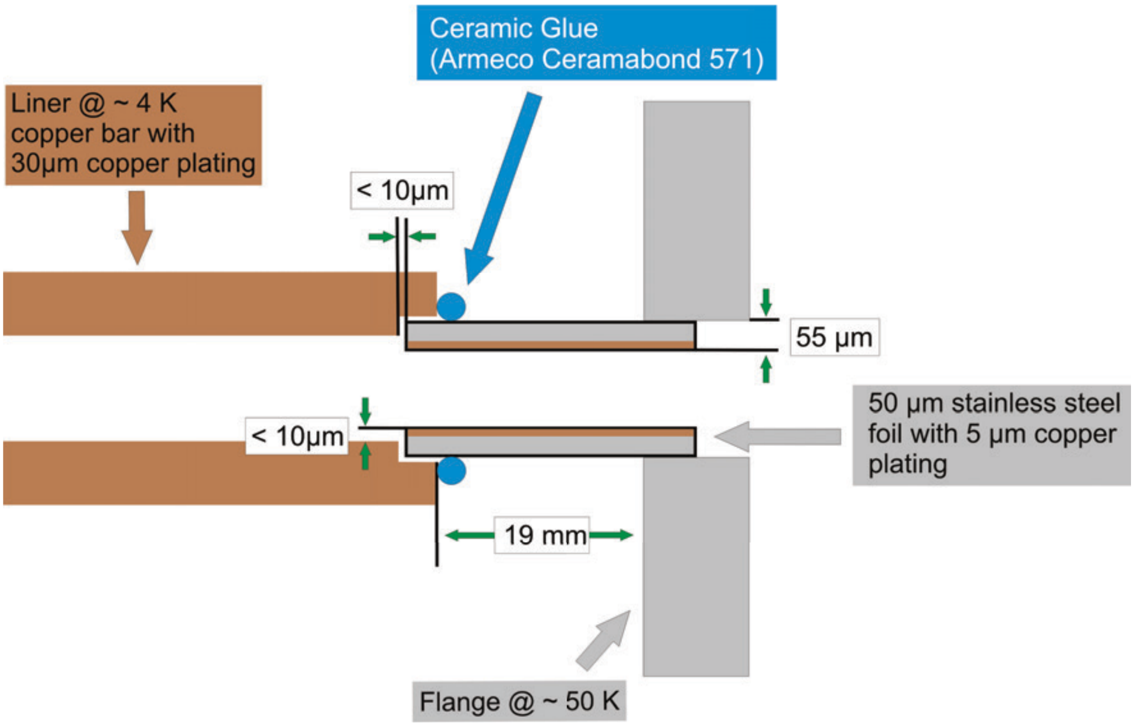

Figure 4.10: Thermal transition from RF–bellows to the cold liner section.

To reduce heating effects from geometrical impedance caused by changes of the beam pipe geometry (see Sec. 3.2.1), the transition foil is connected to the cold liner without steps and gaps bigger than 10 µm within the central region of ±10 mm from the beam axis, where most of the image currents are flowing.

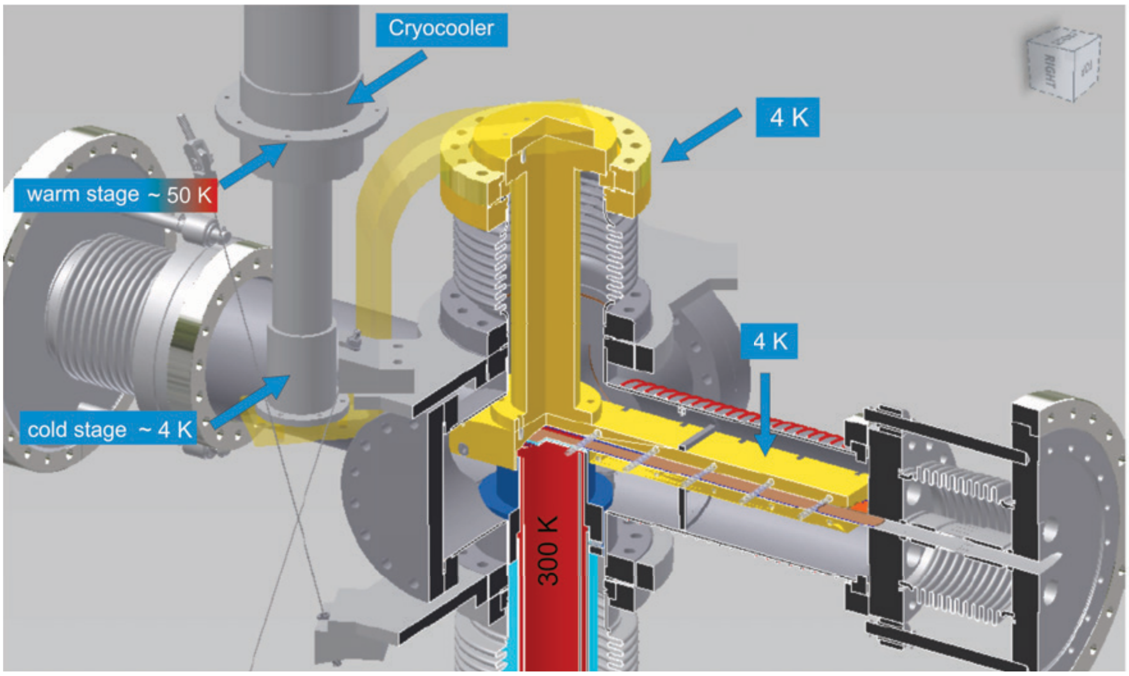

Figure 4.11: Cold mass at 4 K [63].

Figure 4.11 shows the cold mass comprising the 490 mm long cold liner section and the connection to the cryocooler. Both components are made out of oxygen-free high thermal conductivity copper (OFHC). To improve the thermal contact conductance between the two components, a 125 µm thick indium foil is clamped in the joints. On the top and bottom of the cold liner section, screened from the beam, temperature sensors and heaters are installed to measure the beam heat load.

4.4 Diagnostics

The COLDDIAG experiment was designed and built to measure and investigate the beam heat load on a cold vacuum chamber. For this purpose the cryostat was equipped with temperature sensors, pressure gauges and residual gas analysers as well as retarding field analysers (see Fig. 4.12), which are presented in the following sections.

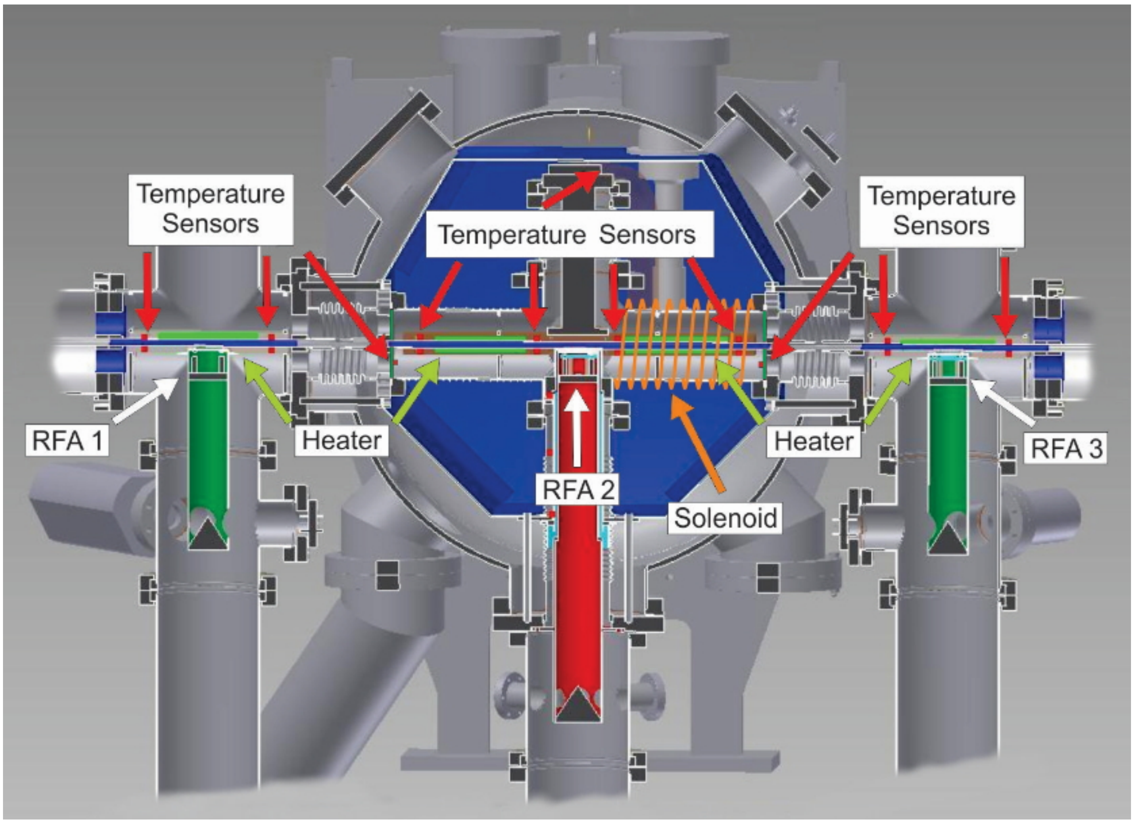

Figure 4.12: Overview of the installed diagnostics devices in COLDDIAG.

4.4.1 Retarding field analysers

To measure the flux and the energy distribution of charged particles hitting the chamber walls, there are Retarding Field Analysers (RFA)located at each of the pumping ports. The half moon shaped RFA in COLDDIAG consists of a tungsten mesh and a detector plate placed behind pumping holes in the beam tube (see Fig. 4.13). The beam tube is electrically grounded as it is connected to the cryostat. The tungsten mesh can be biased negatively or positively (against ground) with varying voltages. The detector plate can also be positively or negatively biased (against ground) opposite to the mesh to collect the charged particles passing through the repelling grid. The current of particles hitting the collector plate is measured by a Keithley 6514 electrometer [67]. With the installed Thurlby Thandar Instruments (TTI) power supply, a maximum retarding voltage of 250 V can be applied in steps as small as 10 mV. The collector voltage can be varied from 0 V to 60 V. Experiments with an RFA with similar design and readout were performed at the ANKA storage ring. During the calibration done at the Laboratori Nazionali di Frascati (LNF) it appeared that the proposed RFA setup might not be sensitive enough to determine the energies of the primary electrons passing the retarding grid. Instead, the measured spectra are dominated by secondary electrons created at the grid or the collector [68]. Therefore, to improve the signal to noise ratio, a lock-in technique was implemented in addition to the DC readout. A 3830 BNC multiplexer from Signal Recovery [69] is used to switch between the two measurement options. A sinusoidal voltage supplied by the 7230 dual phase lock-in amplifier from Signal Recovery is coupled via a microphone transformer on top of the retarding voltage. A battery pack with a fixed voltage of 85 V is used to bias the collector. With the lock-in amplifier, the current on the collector is measured versus frequency and phase. A comparison between the two measurement modes done with a hot filament in a laboratory experiment were promising (see Fig. 4.14). In this test setup, the electron spectrum obtained with the electrometer showed already some noise with steps of 1 V on the retarding grid. On the contrary, the data measured by using the lock-in amplifier exhibited the expected broad spectrum and less noise even with an energy resolution of 0.1 eV.

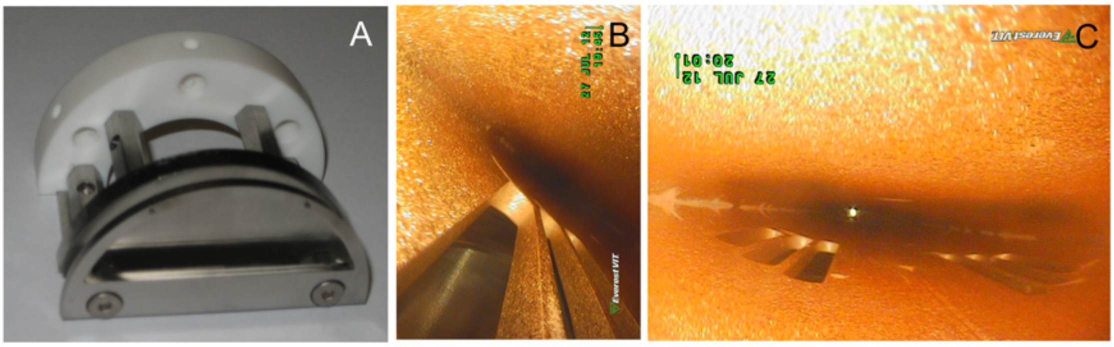

Figure 4.13: Picture of the half moon shaped RFA mounted into COLDDIAG without tungsten Grid (A), the tungsten grid of the RFA under the pumping holes and the pumping holes in the cold liner section (C).

4.4.2 Solenoid

Over the downstream long arm of the cold six-way cross, a magnet coil is installed to suppress charged particles impinging onto the liner walls. Electrons with a velocity component perpendicular to the beam direction are deflected on a helical path and guided

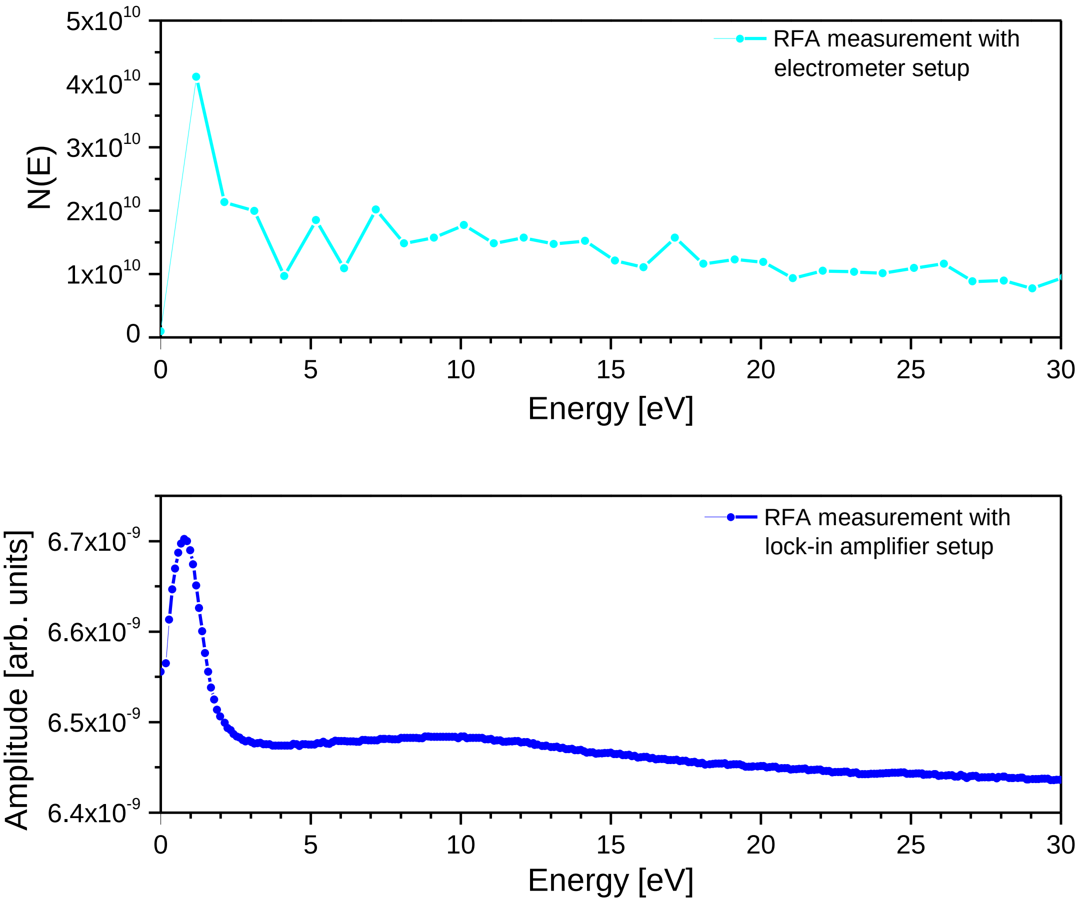

Figure 4.14: Comparision of the two RFA readout setups. Energy spectrum obtained by the electrometer (top), and with the lock in amplifier (bottom), of the low energy electrons hitting the detector and generated by a hot filament in a laboratory experiment.

out of the cold liner section. The magnet coil has a length of 160 mm and an inner diameter of 120 mm. To reach an on axis peak field of 5 mT, a current of 0.43 A is needed. To prevent overheating, the coil is connected directly to the warm stage of the cryocooler and a sensor is installed on the windings to monitor the temperature. Whereas currents below 0.43 A can be applied for long periods, currents up to 1 A corresponding to a field of more than 10 mT can be applied only for short times in the order of 30 min. This is due to the slow heating up of the solenoid which impacts on the temperature measurements.

4.4.3 Pressure gauges and residual gas analysers

Each of the three pumping ports also contains a MKS Inverted Magnetron gauge and a Pfeiffer Vacuum PrismaPlus™ QMG 220 residual gas analyser to monitor the total pressure and the gas content in the three sections of the UHV chamber. The lowest measurable pressure of the cold cathode gauges is below 10^{-10} mbar. The residual gas analyser covers a mass span from 0 to 100 amu and is equipped with a Faraday and a continuous secondary electron multiplier (C-SEM) detector. The minimum measurable partial pressure is below $5 \cdot 10^{-12}$ mbar with the Faraday and 10^{-14} mbar with the C-SEM detector [70].

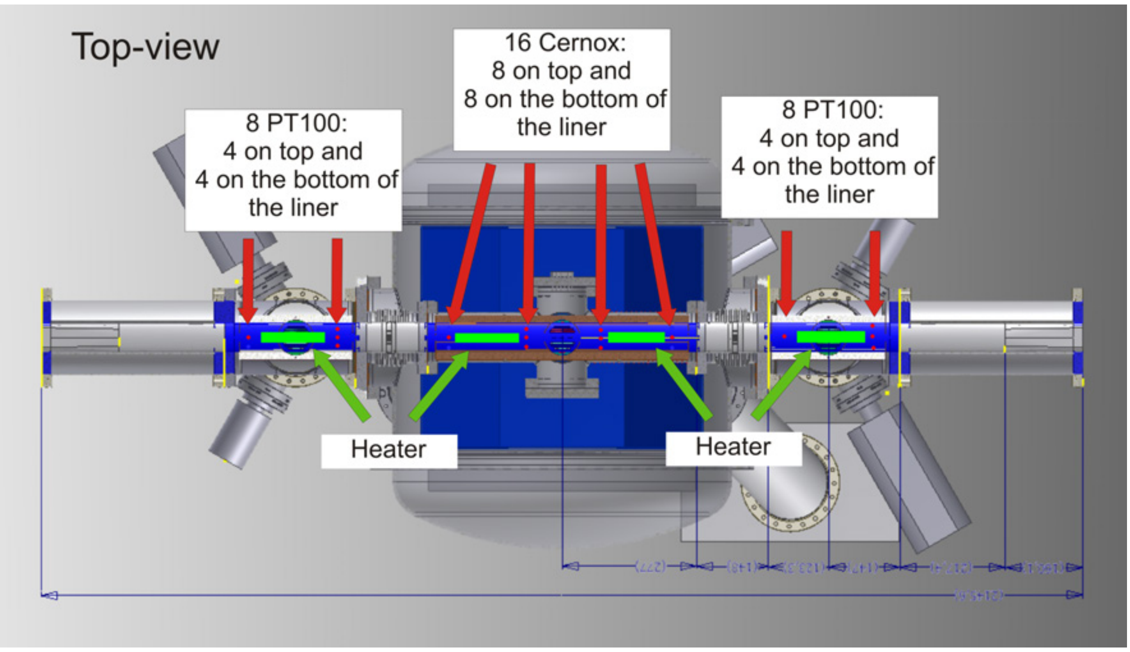

Figure 4.15: Locations of heaters and temperature sensors.

4.4.4 Gas injection system

COLDDIAG is also equipped with a gas dosing system to investigate the influence of different gases naturally present in the beam vacuum on the beam heat load. A DN40 CF 4-way-cross is connected to the middle diagnostic port and the beam vacuum chamber via a remotely controlled valve. For safety reasons, to avoid venting the synchrotron beam vacuum, this valve can only be opened when the main valves at the end of the section where COLDDIAG is installed are closed. To monitor and control the pressure, a full range gauge consisting of a penning and a hot cathode gauge as well as a precise stepper motor controlled leak valve from VSE Vacuum Technology are also installed at the 4-way cross. With the possibility to heat the valve seat, the leak valve offers a controlled leak rate down to $1 \cdot 10^{-9}$ mbar l/s [71]. The last port can be connected to a pump cart (see Fig 4.16). The gas dosing system can be used to prepare a defined amount of gas in the gas dosing chamber and release it into the beam vacuum or to provide a continuous gas flow through the middle diagnostic port onto the cold liner surface.

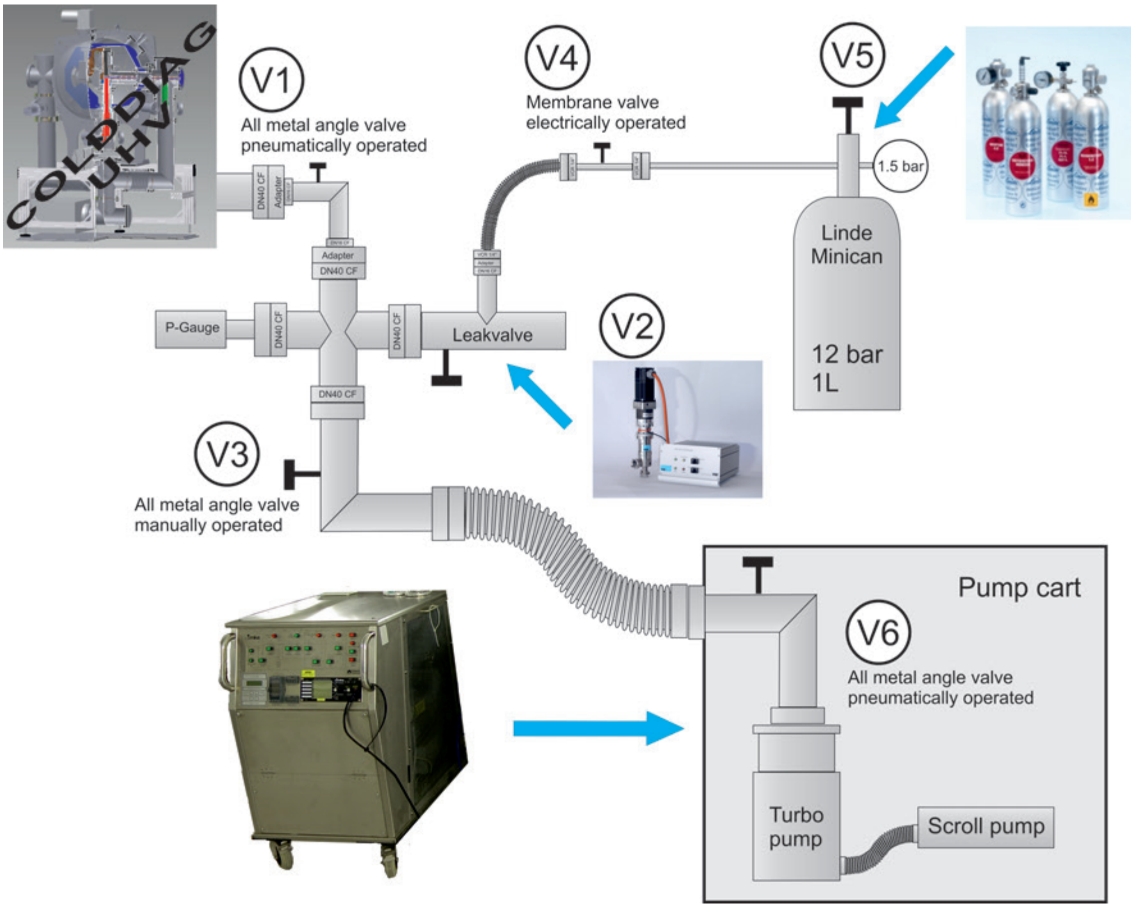

Figure 4.16: Sketch of the gas injection scheme.

4.4.5 Temperature sensors

The main aim of COLDDIAG, to measure the beam heat load, requires precise temperature measurements and the possibility to apply well defined heating powers. To measure the temperature increase due to the beam or the heaters and to monitor the functionality of COLDDIAG, the experiment is equipped with 42 temperature sensors. With five Lakeshore 218S temperature monitors, a maximum of 40 sensors can be used at the same time. Thirty two of these sensors are distributed on the three liner sections, with eight located in each of the warm parts and 16 in the cold (see Fig. 4.15). All temperature sensors are read out with the four wire measurement technique. Pt-100 sensors with a standard calibration curve are used in the warm sections and in the cryostat, where an operating temperature higher then 50 K is expected. On the cold liner and everywhere else in the cryostat, Lakeshore Cernox™ 1050SD sensors are used. The sensors located on the cryocooler have been calibrated by Lake Shore Cryotronics [72]. All other Cernox™

sensors have been calibrated with a setup supplied by the group of Prof. H. v. Löhneysen of the Physikalisches Institut of the Karlsruhe Institute of Technology (KIT). As suggested by Lake Shore Cryotronics Inc. a Chebyshev polynomial of 9th order which is defined by the recurrence relation

$$\begin{aligned} T_0(x) &= 1 \\ T_1(x) &= x \\ T_{n+1}(x) &= 2xT_n(x) - T_{n-1}(x) \end{aligned} \tag{4.1}$$

is fitted to the measured resistance values of the temperature sensors. Figure 4.17 shows the typical resistance behavior of an exemplary temperature sensor for the temperature range 4-300 K along with the parameters used for the fitted Chebyshev polynomial. The inset shows the residual of the fitted function, which indicates that the error of the calibration is less than ±0.25 K in the region of interest below 77 K.

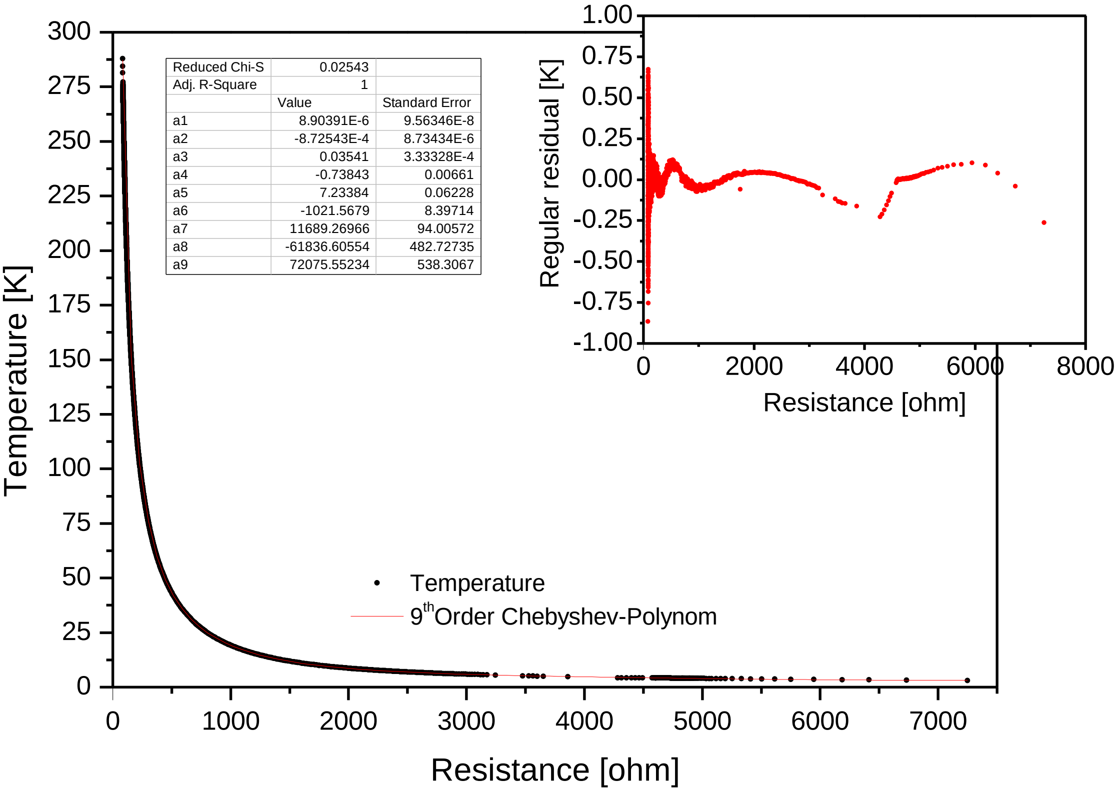

Reduced Chi-S	0.02543	
Adj. R-Square	1	
	Value	Standard Error
a1	8.90391E-6	9.56346E-8
a2	-8.72543E-4	8.73434E-6
a3	0.03541	3.33328E-4
a4	-0.73843	0.00661
a5	7.23384	0.06228
a6	-1021.5679	8.39714
a7	11689.26966	94.00572
a8	-61836.60554	482.72735
a9	72075.55234	538.3067

Figure 4.17: Resistance of a typical Cernox™ temperature sensor for the temperature range from 4-300 K, the inset shows the regular residual from the fitted Chebyshev polynomial.

4.4.6 Heaters

There are six heaters in COLDDIAG, one on the top of the liner in each warm part, with two on the top and two on the bottom of the cold liner. The heaters simulate the heat intake from the beam to calibrate the measured temperature to a defined heating power. It is also possible to use these heaters to maintain a well defined temperature and directly determine the heating power from the beam by the difference in power needed to stabilize the temperature with and without beam. The heaters are 120 mm long and 10 mm wide. They consist of a 0.125 mm diameter 99.99 % pure Ni-chrome wire clamped between a 1 mm thick thermal conducting Sapphire plate and a 3 mm thermal isolating MACOR™ plate. Ni-chrome wire has the advantage of a high resistance, which changes very little compared with stainless steel during cool–down [73]. With a resistance of 30 Ω and a current of 0.5 A, each one of the heaters can reach a maximum of around 7.5 W. Each individual heater is controlled by a TTI power supply with a maximum voltage of 60 V and a maximum current of 1.5 A. Two additional cartridge heaters, with 50 Ω resistance, are installed on the cold stage of the cryocooler head inside the insulation vacuum. These heaters can be used to apply larger amounts of heating power to the cryostat to change, for example, the operating temperature of COLDDIAG. Whereas the heater cables in the warm sections are made of copper, for the heaters inside the cryostat, feed cables with a low thermal conductivity and a relatively high electrical resistance had to be used (see Sec. 4.4.7). To obtain only the power consumed by the heaters, a four–wire measurement technique is used. The voltage drop over each heater is measured with a Keithley 2700 multimeter equipped with a 7700 20–channel differential multiplexer module.

4.4.7 Wiring

All sensors and heaters are placed in the beam vacuum. Therefore, the wiring has to be radiation resistant, suitable for cryogenic use and UHV compatible. With the decision to install COLDDIAG at the DLS, the use of any organic material in the beam vacuum was restricted or at least had to be avoided wherever possible. The limited available space in the beam vacuum and the number of wires needed made it impossible to use ceramic beaded wires, because of the relatively large size of the beads. An AWG 32 Nickel-Copper wire with a thin insulation layer of sintered ceramic was first used to connect the temperature sensors and heaters. The vacuum compability in a radiation environment was tested by the DLS vacuum group. To avoid noise pick up, the four wires of each sensor were twisted together. In the cold section, the wires have to be around 2.5 m and are much longer than in the warm sections to avoid additional heat intake from warm parts of the cryostat. In addition, the wires need to be thermally anchored to a heat sink to minimize heating of the temperature sensors through the wires. During assembly and thermal anchoring of the wire, several shorts occurred and the wire had to be replaced by an organic insulated wire because the ceramic insulation was too thin and not flexible enough. A Lake Shore AWG 36 Quad-Twist™ wire made of Phosphor Bronze was chosen after vacuum and radiation testing which was also performed by the DLS vacuum group. The wire is Formvar® isolated and consists of two twisted pair wires, which are again twisted together, to minimize noise pick-up.

The wires inside COLDDIAG are bundled to 50 pin connectors. In total, five 50 pin feedthroughs, three from the cold section and one from each warm section, provide the signals to the outside of the vacuum chamber. To minimize noise pickup on the 35 m long cables from the experiment to the control rack, all the cabling for the sensors is halogen-free UNITRONIC® LAN 1200 H CAT.7 cable from Lapp Kabel. The screened cable consists of four twisted pair cables, which are additionally screened. Similar to the wiring inside the cryostat, the voltage and the current path of the four wires attached to one sensor are twisted together and the signals of two sensors are transported in one cable. As the voltage and the current are much higher in the heater circuits compared with the temperature sensor circuit, a cable without additional screening but of thicker cross–section was chosen. UNITRONIC® LiHCH (TP) cable with a cross–section of $0.5\,\mathrm{mm}^2$ is used for the power cable and a thinner $0.25\,\mathrm{mm}^2$ cross–section cable for the sense circuit of the heaters.

4.5 Control system and data acquisition

For the control system and data acquisition of COLDDIAG some basic requirements had to be fulfilled. Data acquisition and data storage rates of 1 Hz were required and the control-system should be able to run reliably for at least one week. In addition, it needed to be possible to easily and quickly adapt the control system to different experimental needs and also to the control-system of different light sources. Taking into account these requirements, the decision was made to build a LabVIEW™ based stand-alone control system and a MySQL database to store the acquired data. To backup the acquired data, new database entries are dumped every 24 h and sent to a mirror database located at ANKA. At the DLS, access to the experiment is of course not possible and access to the control racks should be reduced to a minimum to not disturb the electronics and accidentally drop the beam during user beam time. For this reason, beside the readout of the installed electronics, the control system needed to offer full remote control of all installed power supplies, voltmeters, amperemeters and the lock-in amplifier. In March 2012, a temperature PID control loop was additionally implemented which makes it possible to measure the beam heat load at a constant temperature of the beam pipe. A blockdiagram of the signals in COLDDIAG can be seen in Fig. 4.18. Figure 4.19 shows the overview panel of the COLDDIAG control-system, which informs the operator about the status and any critical problems with cooling, temperatures and pressure of COLDDIAG.

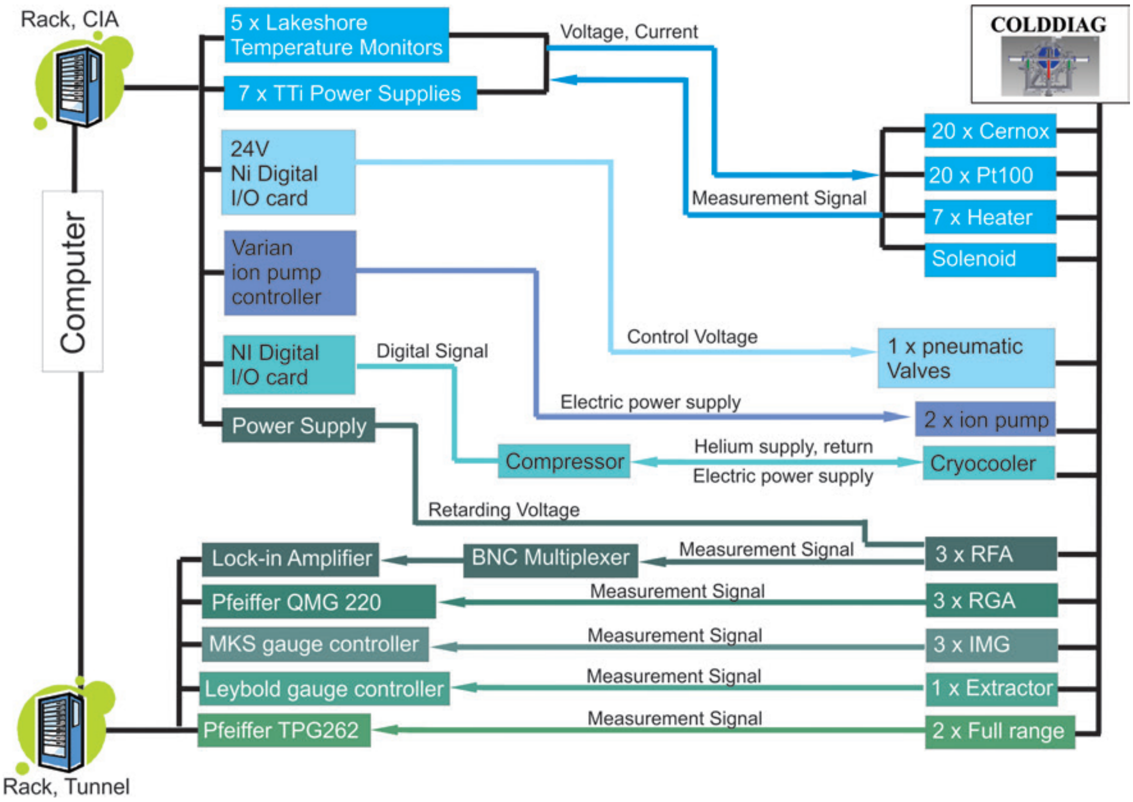

Figure 4.18: Blockdiagram of the signals in COLDDIAG.

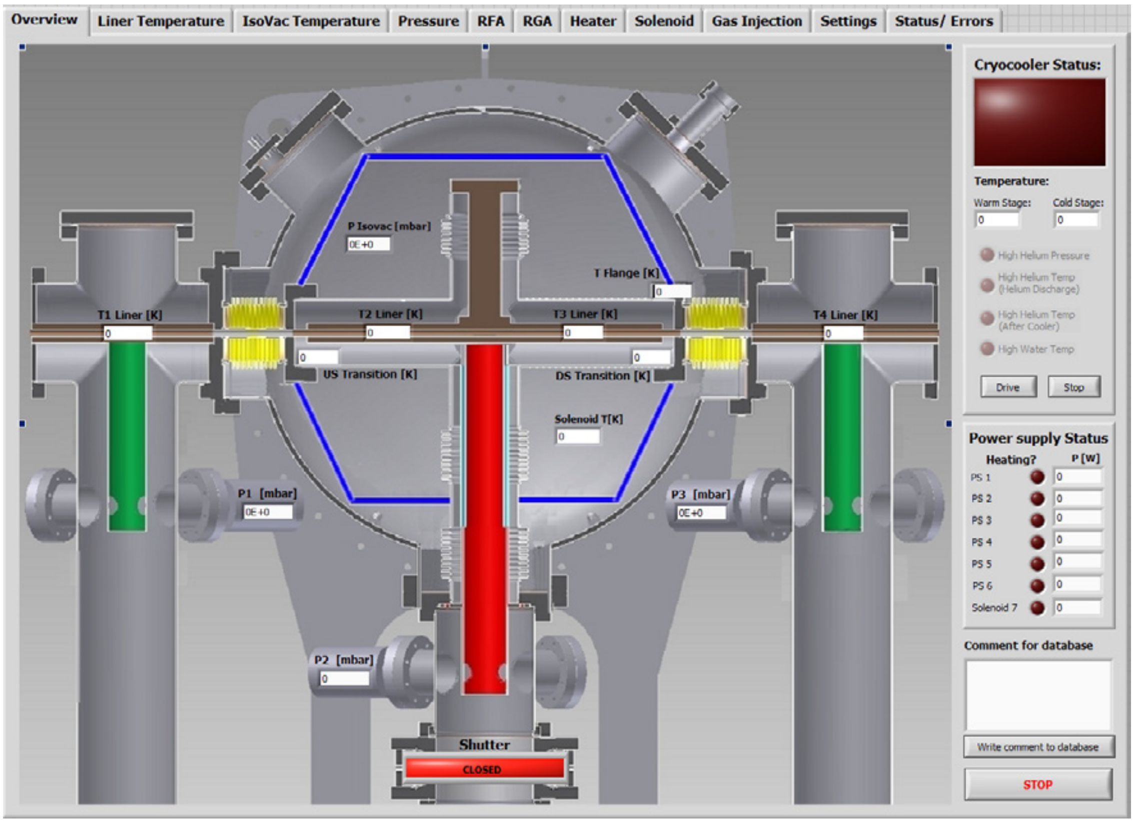

Figure 4.19: Overview panel of the COLDDIAG control-system.

4.6 Changes and tests before the second installation

COLDDIAG was installed in the storage ring of the DLS during a machine shutdown in November 2011. After the first successful tests and measurements with beam (see also Sec. 5), the downstream thin thermal transitions from the RF–bellows flange to the cold liner section failed and caused a beam dump (see Fig. 4.20). As the foil of the transition was bent into the beam stay clear it was only possible to use the storage ring by inserting a bump in the orbit of the electron beam. Consequently, COLDDIAG had to be removed after only one week of user beam. This section describes the failure analysis, the changes made to improve the thermal transition, as well as the experiment and the tests performed to guarantee proper functionality before reinstallation.

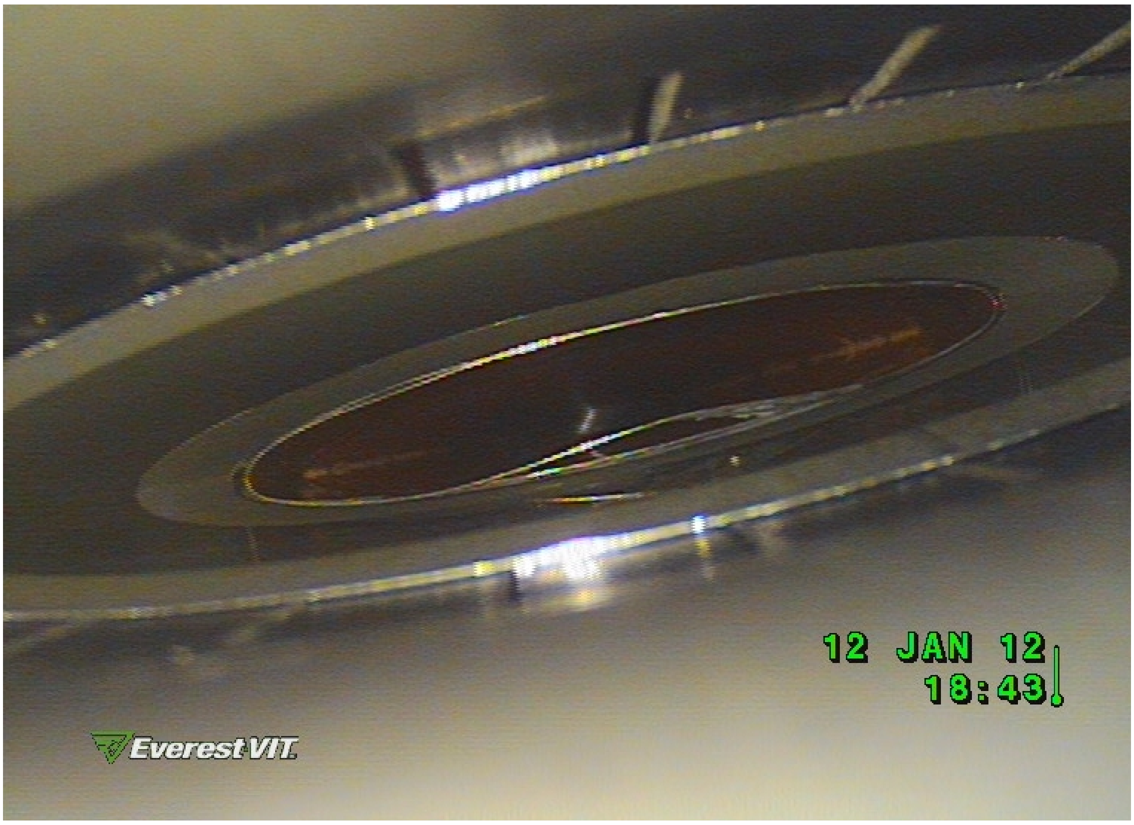

Figure 4.20: Endoscope picture of the broken downstream transition.

4.6.1 Failure Analysis

After removing COLDDIAG from the storage ring and disassembling of the cryostat and the two thermal transitions, a substantial failure analysis was performed. The investigation showed that on both the upstream and the downstream ends the ceramic glue which was used to secure the transition foils in place had failed. This happened most probably due to the vibrations during transport. In addition, a thick surface oxide layer, typical for stainless steel, and the lack of contact pressure made a bad electrical contact on the sliding joint between the transition foil and the RF–bellow flange. This caused an increased geometric impedance and consequently a temperature rise followed by a thermal expansion of the transition foil. The copper bracket holding the thermal transition in place did not expand, as it was in much better thermal contact with the cold liner section than the transition foil. This expansion of the transition foil, together with the different expansion coefficients of the stainless steel and the copper plating, in conjunction with the failed ceramic glue, forced the transition foil to bend towards the beam.

4.6.2 Changes to the thermal transition design

To make a second installation of COLDDIAG at the DLS feasible, the design of the thermal transition had to be completely revisited. The requirements on this part of the cryostat, from the RF–bellows to the cold liner section, are very high, as it is one of the most critical points concerning the functionality of COLDDIAG. To avoid heat transfer from the 50 K to the 4 K region, a only (50 µm) thin transition foil has to be used. Moreover, to minimize beam heating due to geometric impedance from a step, the foil should be very precisely connected within ±10 mm of the horizontal center of the cold liner. At the same time, electrical continuity needs to be maintained and the surface resistance of the foil has to be small to minimize heating from image currents. After the failures during the first installation, a much more rigid solution had to be found. To maintain the tight overall mechanical tolerances on the transitions and to minimize manufacturing time and costs, the cold liner section and the copper brackets holding the transition had to be used again.

The main concept of the improved thermal transition is to split the transition into two foils with different thicknesses. A copper–plated stainless steel foil is fixed to the copper liner and slides on a 200 µm thick copper foil fixed to the RF–bellow (Fig. 4.21). To minimize heating effects from a possible step from the thin to the thick foil, the edge of the copper foil is chamfered with a tapering angle of less than 6 °. To reduce the electrical resistance of the contacts, only copper to copper transitions are made. Moreover, to improve electrical contact, the two foils are pressed together by copper beryllium springs. Crucial for the new transition design is the use of a stronger connection method, which fulfills the DLS vacuum requirements and has a good cryogenic performance. The commonly used non-organic metal to metal bonding techniques for UHV and cryogenic conditions, including low temperature brazing, spot welding, vacuum soldering and ultrasonic soldering, have been investigated. All of these processes were ruled out because they include high temperature, which could deform the small transition parts, or in case of the ultrasonic soldering are not easily available. Soft solder is not normally used in UHV applications because of the relatively high vacuum pressure of lead and the unknown amount of residual

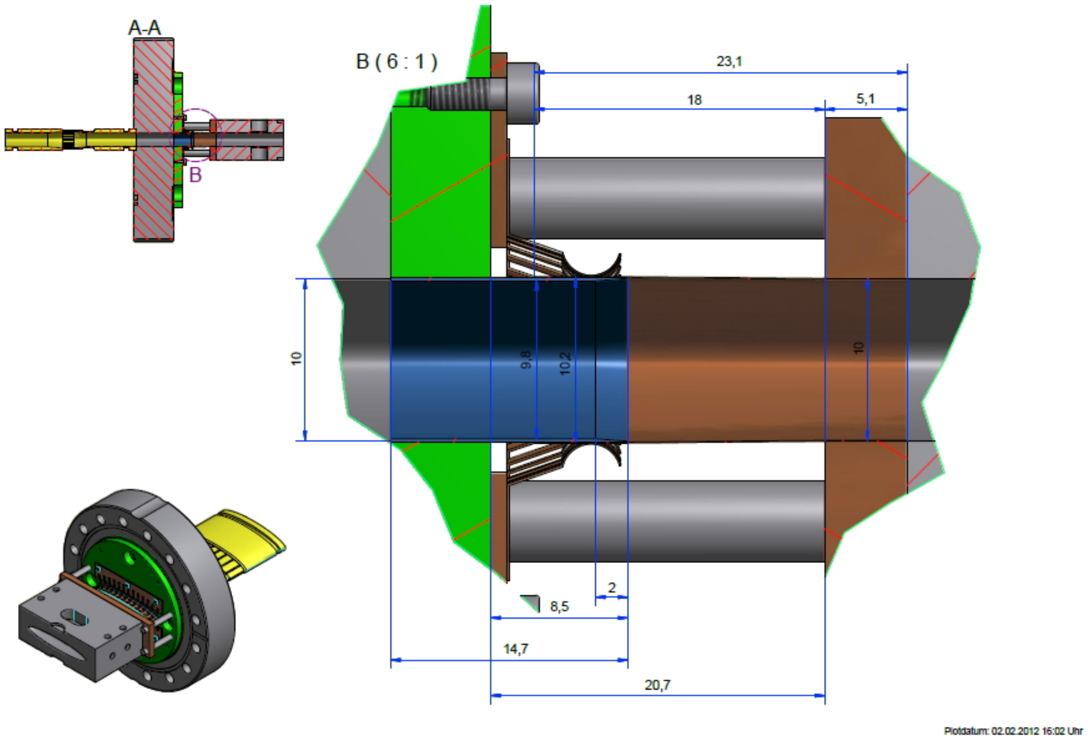

Figure 4.21: Drawing of the improved thermal transition foil.

flux. In addition, small cavities, which are created during the solder process, can possibly trap gas or flux bubbles that may corrode through the solder. For this reason, several experiments with different lead and tin based low temperature solder and brush plating techniques were conducted. A Sn60/Pb40 Multicore solder with Crystal™ 400 flux, which already performed well in preliminary vacuum tests done by the DLS vacuum group, was chosen for further investigations. The flux is a so called 'NO CLEAN' flux, which is only slightly corrosive and can be removed relatively easily with acetone and a isopropanol ultrasonic bath. The disadvantage of the mild resin in the flux is an insufficient removal of the surface oxide of the stainless steel which is required to create a good solder joint to the copper. In order to create a good bonding surface on the one hand, but only a thin layer which does not increase the thermal conduction over the thermal transition, the stainless steel foil was plated with a thin layer of Nickel, followed by a thin copper layer by using a brush plating technique. Soldering trials, carried out with different prototypes, showed that the best flow of the solder was achieved by using copper surfaces on both sides of the joint. Enclosure of any substances into the liquid solder was avoided by using a high vacuum solder oven especially built for this purpose (see Fig. 4.22). The oven

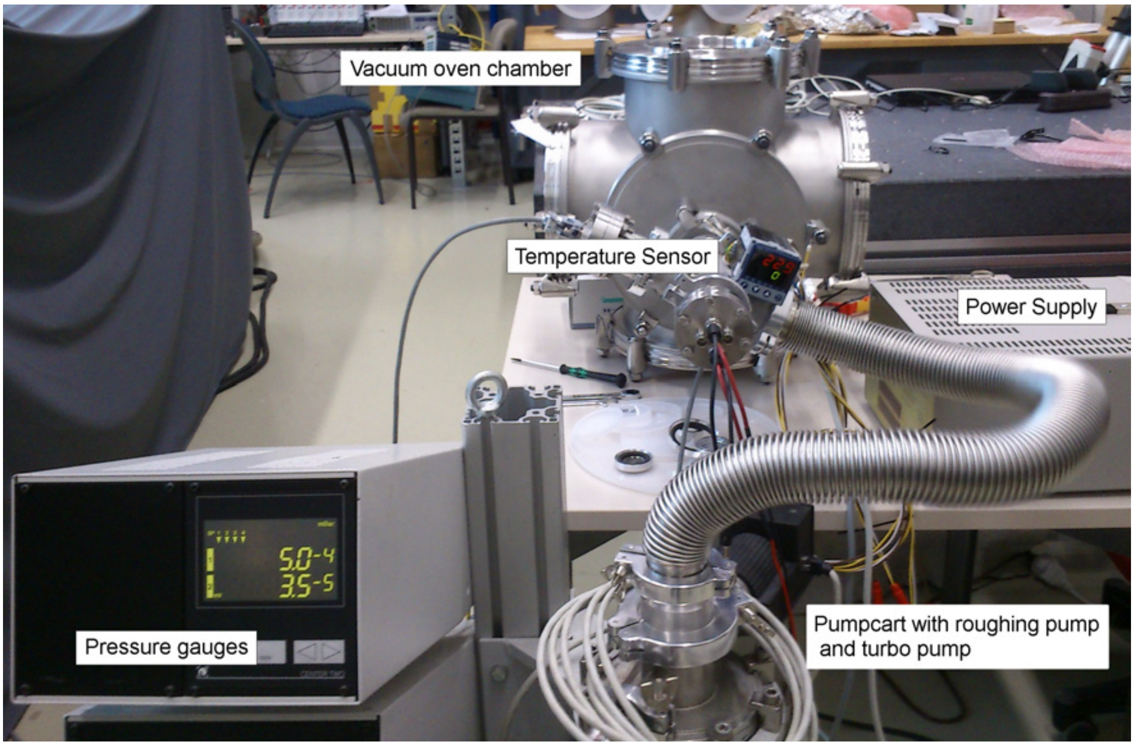

Figure 4.22: Vacuum soldering oven.

has a 100 mm x 100 mm hot plate with a maximum heating power of 100 W. At room temperature, a base pressure of $1.5 \cdot 10^{-6}$ mbar can be reached. The following procedure was used to produce several prototypes and also the final transition pieces:

- The transition foil is roughly cut into shape.
- The 200 µm thick copper foil is chamfered with fine sandpaper and isopropanol (see Fig. 4.23).

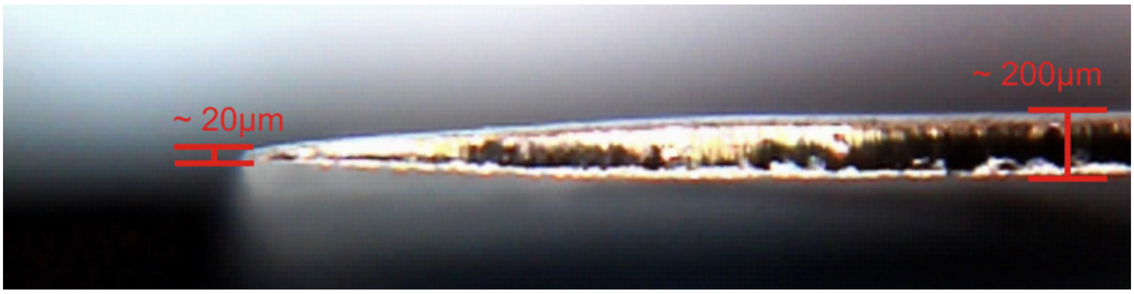

Figure 4.23: Chamfer on the copper foil

- Depending on which side of the transition piece is soldered, either the stainless steel foil or the bracket is cleaned with a mild acid and a fine polish.
- A layer of nickel followed by a thin layer of copper is applied by brush plating on the stainless steel surface of the transition pieces (see Fig. 4.24).

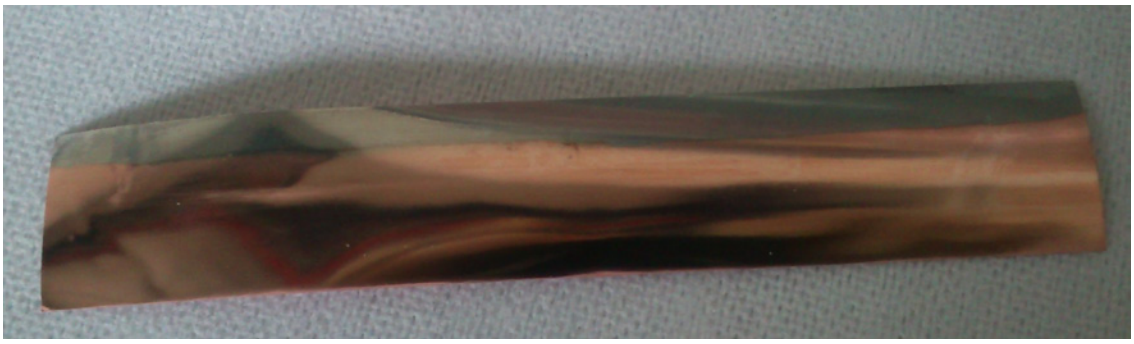

Figure 4.24: Stainless steel transition foil after brush plating with nickel and copper

- The copper foil or the 50 µm stainless steel foil is cut precisely to the desired width and length.
- The plated foil is inserted into the copper bracket and spread by a precisely adjusted wedge.
- Three turns of the Sn60/Pb40 solder are wound around the angle between the bracket and the foil.
- The whole assembly is put onto the hot plate in the vacuum oven (see Fig. 4.25), evacuated to a pressure below $1 \cdot 10^{-5}$ mbar and vented with nitrogen gas to avoid oxidation during the heating process.
- The hot plate is then powered with 100 W and heated above the solder melting point (183°-190°).
- After 30 min, a temperature of 210 °C is reached and the pumping of the vacuum chamber is started.
- At 230 °C, a pressure of $1 \cdot 10^{-4}$ mbar is reached, which decreases to $5 \cdot 10^{-5}$ mbar within the next 10 min while the temperature is held at a constant level.
- Now the heating is switched off and after 12 h a pressure of around $1.5 \cdot 10^{-6}$ mbar is reached.

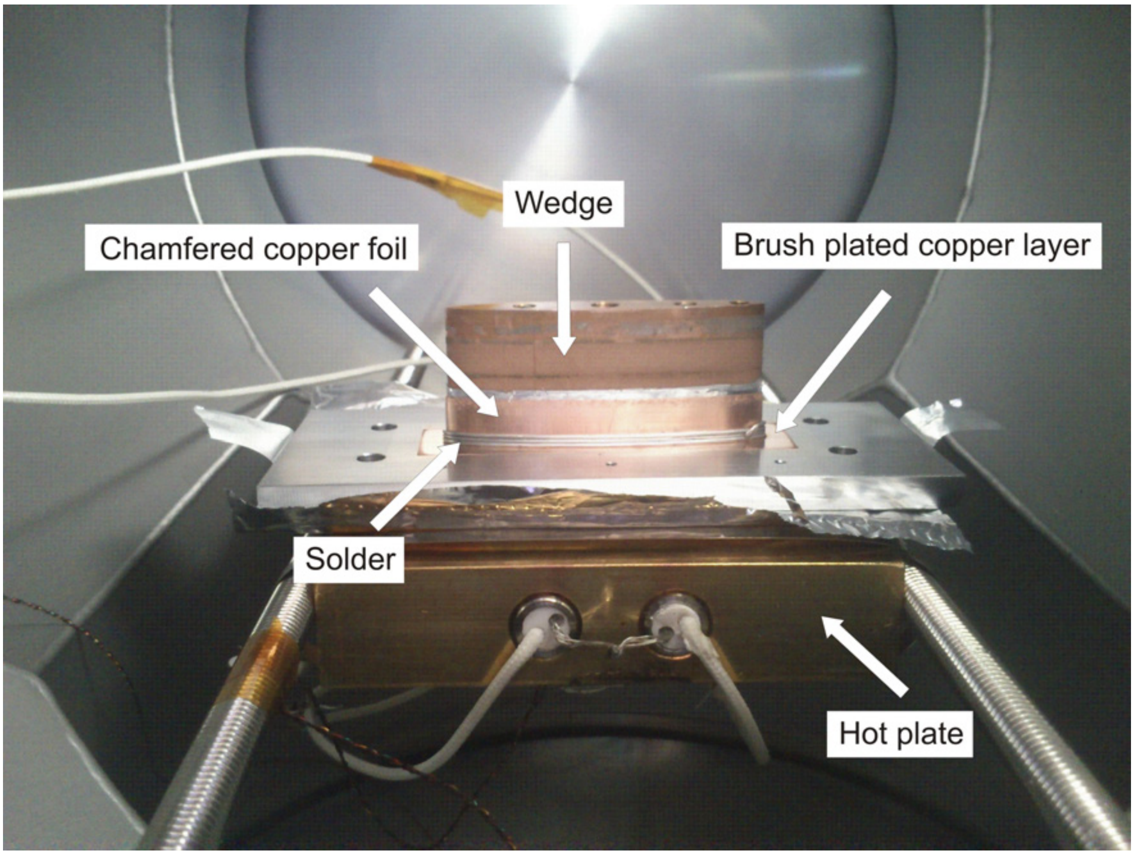

Figure 4.25: Prototype transition piece inside the solder oven

- The soldered pieces are first roughly cleaned with acetone and then put into a ultrasonic bath filled with isopropanol and finally rinsed with deionised water and dried with nitrogen.
- The pieces are then put into a UHV chamber and baked at 150 °C for at least 3 days.
- After cool down to room temperature, the vacuum quality is measured by checking the base pressure reached and a massspectrometer scan from 0 to 100 amu.

Before the original transition pieces were soldered, a full prototype transition had to undergo several tests to prove the cryogenic compatibility and rigidness to temperature shocks. For this reason, the test piece was exposed to thermal shocks in liquid nitrogen, each followed by fast warming to room temperature with a heat gun. Figure 4.26 shows the transition piece after 15 thermal cycles. No signs of degradation are visible, nor are thy seen after a prototype was put into liquid nitrogen for 7 days and heated up to 160 °C for more than 15 h. The final transition pieces which are installed in COLDDIAG are also

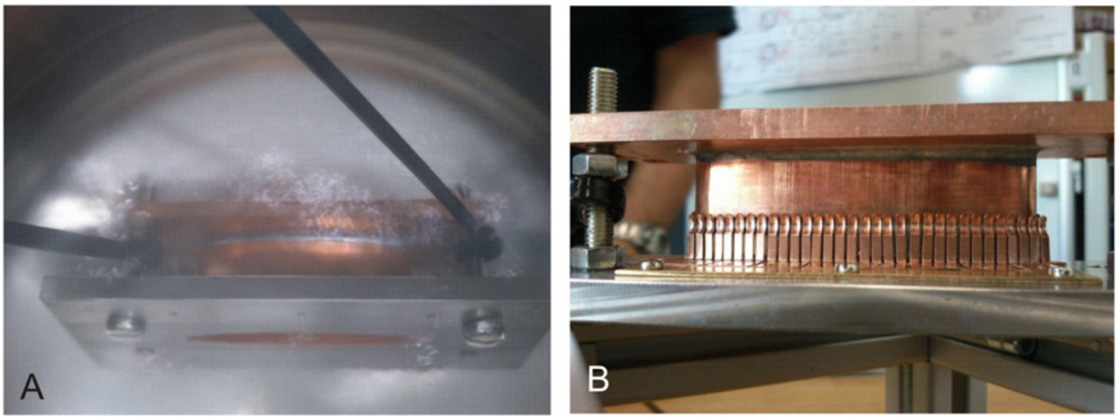

Figure 4.26: Prototype transition piece in liquid nitrogen (A) and after 15 thermal shocks (B).

equipped with a Pt–100 temperature sensor on the warm side of the transition to monitor the temperature in case of a cryocooler failure.

4.6.3 Changes to the UHV layout

During the first installation, the UHV vacuum of COLDDIAG was pumped with a Varian 300 l/s and a Gamma Vacuum [74] 500 l/s ion pump, both connected with a DN150 CF T-piece to a 4-way-cross which was connected to the three diagnostic ports (see Fig. 4.27 A). After 7 days of pumping in this configuration the beam vacuum reached a pressure

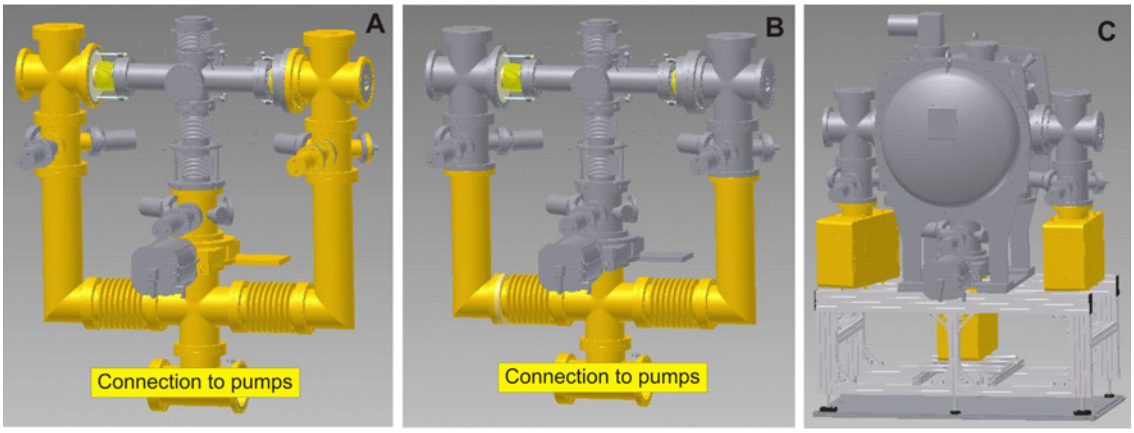

Figure 4.27: Warm parts of the UHV chamber (A), parts removed for after first installation (B) and new pump layout (C).

of $1.6 \cdot 10^{-7}$ mbar in the upstream section, and below $3 \cdot 10^{-7}$ mbar in the middle and the downstream sections before cool-down. With the inner liner section cooled down, the pressure decreased to $5.1 \cdot 10^{-9}$ mbar upstream, $6.9 \cdot 10^{-9}$ mbar on the middle gauge and $6.8 \cdot 10^{-9}$ mbar downstream without the electron beam present. For a possible reinstallation at the DLS, the base pressure of COLDDIAG, especially at room temperature, had to be improved. A bake out of the warm vacuum chamber would only be efficient in conjunction with a bake out of the UHV chamber surrounded by the isolation vacuum. The possibility to heat up the inner vacuum chamber was not planned. This is why several thermal connections in the insulation vacuum are done with Apiezon N grease, which has a melting point of only 42 °C to 52 °C. In addition, it appeared during the first pump down that the UHV and the insulation vacuum cannot be pumped separately without risking the thermal transitions breaking. As the cold liner acts like a cryopump, when cooled down, the base pressure is dominated by outgassing of the unbaked warm vacuum camber. Instead of connecting the three diagnostic ports together to two ion getter pumps, the room temperature connection was removed and each diagnostic port was connected to a separate 300 l/s pump (see Fig. 4.27 B,C). With the new vacuum layout, the pressure at room temperature before cooldown reached $3.7 \cdot 10^{-8}$ mbar at the upstream, $1.1 \cdot 10^{-7}$ mbar at the middle and $4.9 \cdot 10^{-8}$ mbar at the downstream diagnostic port. After cool down, the pressure is below $2 \cdot 10^{-9}$ mbar showing an improvement of more than half an order of magnitude.

4.6.4 Support structure

The connection of the unforeseen second ion pump before the first installation, and the resulting weight on the support structure, as well as the limited space for struts, made the support structure bend during alignment. This made it difficult to precisely adjust the position of COLDDIAG with respect to the vacuum vessels of the storage ring. With the new pump layout it became possible to put additional struts on the support structure and to improve the stiffness of the support structure. Figure 4.28 shows the changes made to the support structure. In addition, during assembly of the cryostat special care was taken to align the liner sections to the support structure.

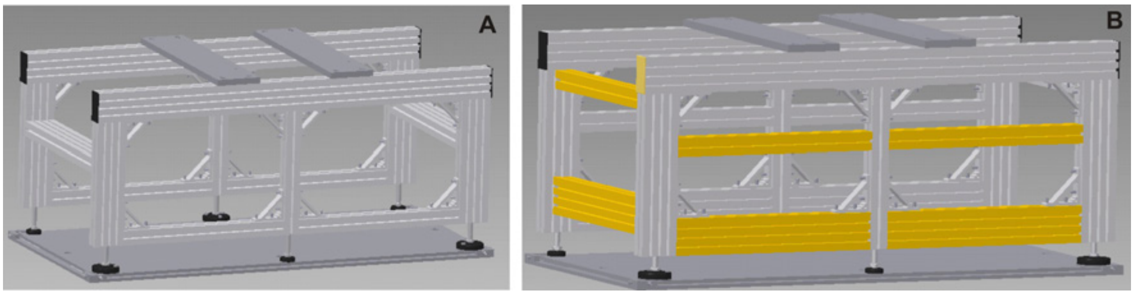

Figure 4.28: Support structure before (A) and after the modification (B). The changed parts are marked in yellow.

4.6.5 Liner movement during pumping and cool down

During several cool downs between the first and the second installation, a vertical movement of the liner had been observed. After these cool downs, different tensions on the thread rods, supporting the cold mass, were measured. This indicated that the thermal contraction of the upper part of the shield, which is fixed to the six-way cold cross, or a possible plastic dilatation of the stainless steel M2 thread rods during cool down was responsible for the movement. To fix this problem, stronger thread rods were used and in addition, the force from the copper shield to the cold cross had to be minimized. The stainless steel M2 thread rods were replaced by Ti6-4Al-V thread rods. This titanium alloy has a higher yield strength, as well as a smaller thermal contraction and thermal conductivity compared with stainless steel [73]. The new rods have the same thread size so that the old support of the thread rods and the cold cross could be used. The copper shield was cut upstream and downstream after the first cool down at the factory, as one of the thermal transitions broke during an unbalanced pump down of UHV and insulation vacuum. With the shield cut, it was possible to remove the RF–bellows without removing the shield and the cold cross. After the repair, the shield was connected again with bent copper strips (see Fig. 4.29 A). This already removed some of the force from the upper copper shield to the cold cross. To make the cooling connections more flexible, but maintain the thermal conductivity, they were replaced with wide copper braids (see Fig. 4.29 B). In the course of the failure analysis, the motion of the cold liner section during cool down had to be investigated before a second installation could be considered. For this purpose, a 6 mm diameter round optical target was manufactured out of Polyether Ether Ketone (PEEK) (see Fig. 4.31 A). A thin wire was glued in a small groove along the length of the target. This allowed the target to be pulled through the beam pipe

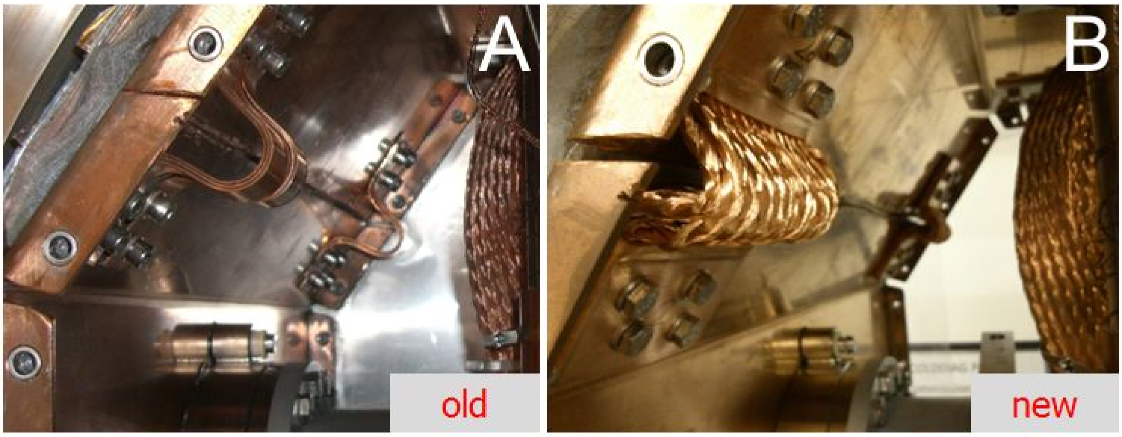

Figure 4.29: Copper connection at the thermal shield before (A) and after the modification(B).

and prevented the target from rolling sideways. The edges of the cylindrical target were chamfered to gently slide over the sensitive transitions. A Leica NA2 level with parallel plate micrometer fitted over the telescope objective was used to measure relative height differences when the target was cooled down or moved through the beam pipe. To pump down COLDDIAG, windows were mounted on the ends of the warm sections. To avoid too much pressure on the copper liner, the beam vacuum chamber and the insulation vacuum chamber are connected from atmospheric pressure down to about 10 mbar. Although the cooling connection at the thermal shield and the thread rods were already replaced, the first cool down, with the target placed in the middle of the cold liner section, showed an upwards movement of almost 700 µm. Subsequent cool downs performed with different tensions on the thread rods coming from the top and the bottom of the cryostat, did not show any improvement. These cool downs also showed that the cold copper beam tube was not bending, but the movement is taking place in the RF–bellows. The consequences from this bend of the RF–fingers are described in subsection 4.6.7. The origin of the liner movement was found to be the lateral aluminum shields (see Fig. 4.30 A, B). These shields are connected to the copper shield and the bottom aluminum shield to act as cooling connection between the two components. The shields were screwed into the top part of the copper shield, the cut parts and the lower aluminum shield. This made the flexible copper braids useless and explains the upwards movement of the liner when shrinking during cool down. As a consequence, the screws in the top half of the lateral shields were removed. A successive cool down showed a movement of less than 50 µm and no influences on the cryogenic system.

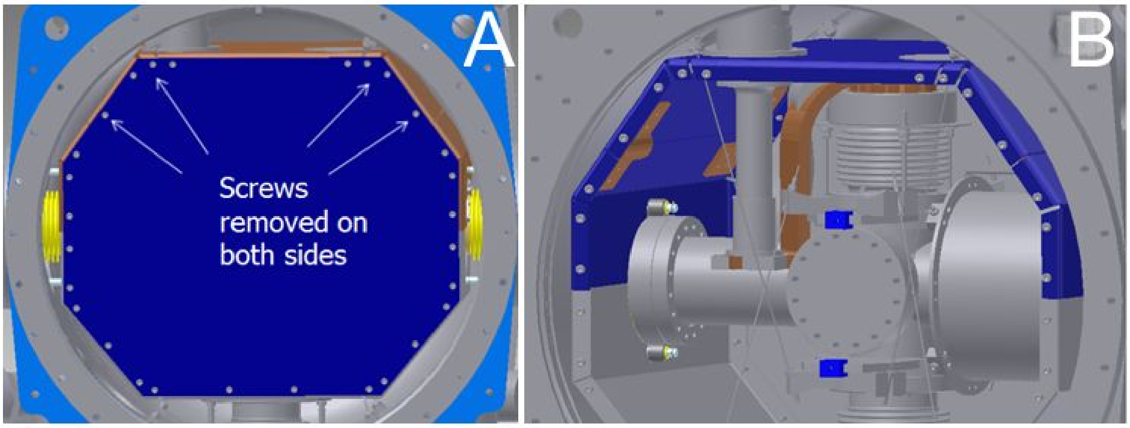

Figure 4.30: Lateral aluminum shield (marked in blue) and removed screws (A) and top copper shield (blue) and bottom aluminum shield (shown in grey) (B)

4.6.6 Measurement of the beam pipe profile

Together with the measurement of the movement of the inner liner section during cool down, the beam pipe profile of the COLDDIAG experiment was also measured with the help of the Leica NA2 level. The optical target described in subsection 4.6.5 was pulled through the liner with the help of a thin wire. This method allowed a more precise alignment and leveling of the warm parts with respect to the cold section, which was only done by eye before. Figure 4.31 B shows two different measurements of the beam pipe profile in COLDDIAG. The blue points show the profile measured from RF–bellow to RF–bellow without the warm parts installed, and the black points are the last measurement before the installation from the upstream warm part to the downstream warm part. The dashed lines are just meant as guidance for the eye. In both cases, the deviation is within about ±270 µm from the nominal position given by a line defined by the end flanges of the RF–bellows, which were leveled before the measurement.

4.6.7 Changes to the RF–bellows

During the first installation of COLDDIAG, shortly after a beam dump, the downstream flange of the RF–bellows showed a temperature much higher than ambient. Investigations of the RF–fingers located in the transition from ambient to shield temperature (see also Fig. 4.7) clearly showed that the fingers were not in contact. The lack of electrical continuity for the image currents caused the observed heating of the outside flange of the RF–transition (see Fig. 4.32 A). The RF–fingers are made out of stainless steel and show only limited springiness. Therefore, the displacement of the inner liner section during cool down plastically deformed them. As the RF–transition is welded into bellows, it was not possible to change the RF–fingers without new manufacturing. Instead of redoing the RF–bellows on both transitions, upstream and downstream, a clamp made out of two stainless steel strips connected with two thread rods was inserted into the space between the RF–fingers and bellows through the four pumping holes located in the flange (see Fig. 4.32 D,E). Figure 4.32 B shows the contact at the RF–fingers from inside the beam tube. In figure 4.32 C the fingers are illuminated from the back side, and one can see that the middle two fingers are in contact. After the modification of the RF–transition, COLDDIAG was cooled down, to check the contact of the fingers at cold and to verify that the additional force of the clamp does not limit the sliding of the fingers required for thermal contraction and expansion.

4.6.8 Measurement and alignment of the straight section during installation

During the installation of COLDDIAG in the DLS storage ring, the cryostat and the upstream and downstream pumping stations, which connect COLDDIAG to the storage ring, were positioned with respect to the nominal electron beam orbit. For the alignment and the check of the positioning of the different components, the DLS alignment team used a laser tracker to measure the position of the CF flanges in the straight section. To

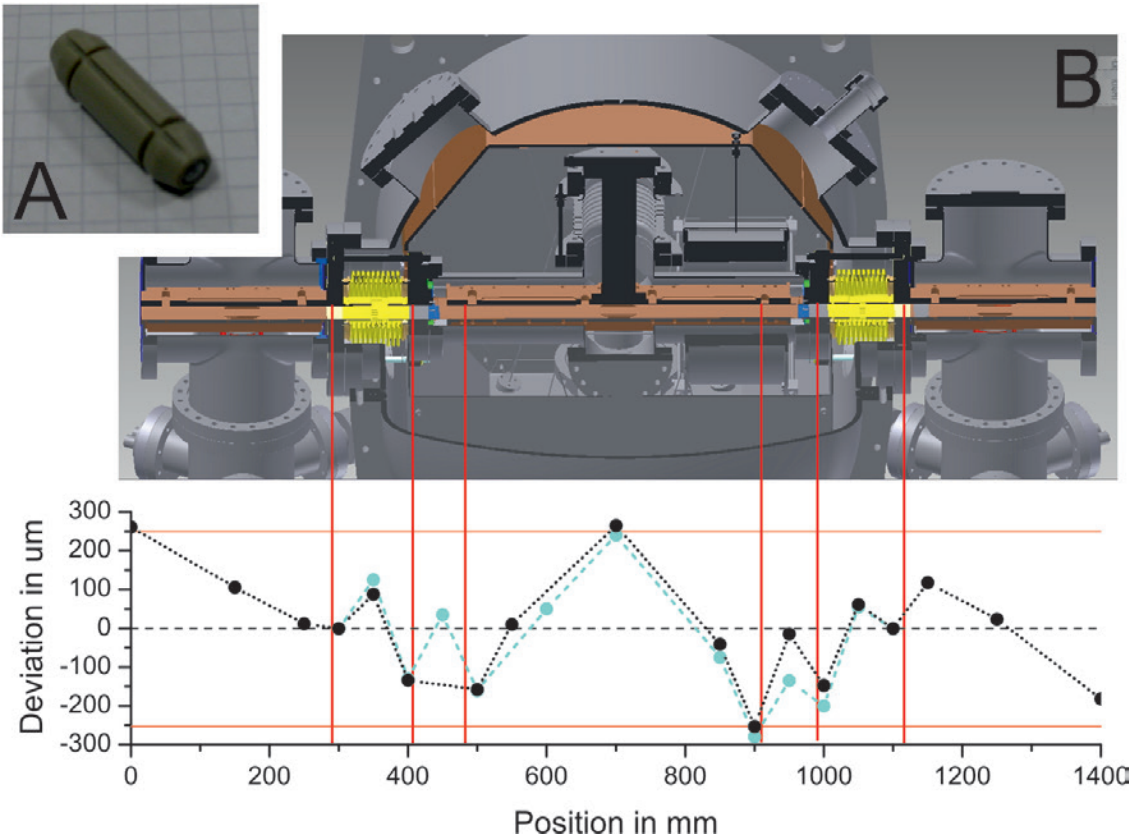

Figure 4.31: Optical target used to determine the liner position (A). Measurement of the beam pipe profile in COLDDIAG (B). The blue points show a measurement from RF–bellow to RF–bellow, the black points from upstream warm part to downstream warm part. The dashed lines are just for guidance. The typical error of the technique can be seen by the difference of the two measurements.

determine the center point of the CF flanges, several points where taken on the flange outside and the tracker software calculated the center point with a cylindrical fit function. Although the center of a CF flange determined in this way does not perfectly match the center of the beam pipe, the measured position agree typically within ± 250 µm. Special care had to be taken on the alignment of the upstream make-up assembly and the upstream taper. This taper acts as radiation mask and shadows COLDDIAG from direct synchrotron radiation from upstream bending magnets, which could possibly damage the cryostat and influence the measurements. During the alignment, the focus was on adjusting the taper and COLDDIAG positions as well as possible. In order to do so, larger deviations from the nominal position, which were caused by mechanical tolerances on the flanges of the vacuum components, were tolerated at the gate valves located at the ends of the upstream and downstream pumping stations. Figure 4.33 shows the horizontal and vertical position

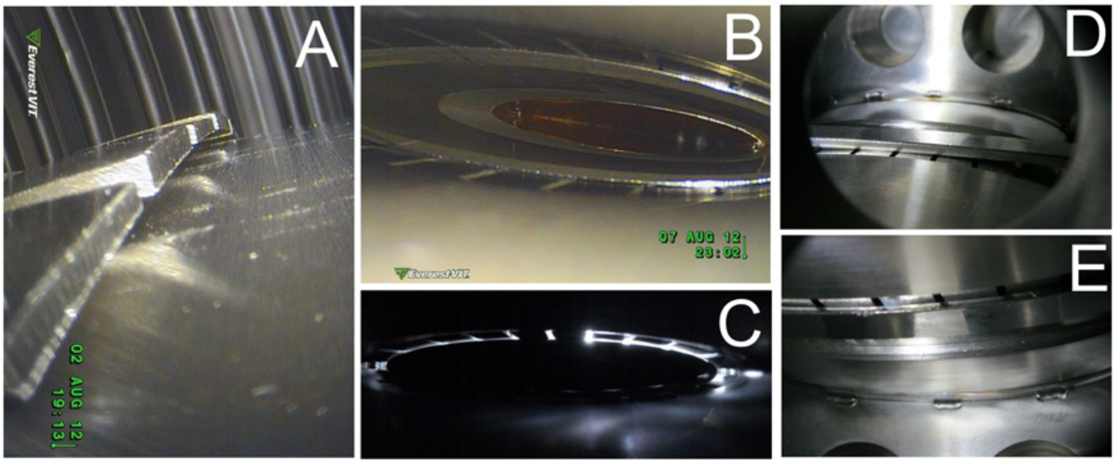

Figure 4.32: RF–fingers before (A) and after installation of the clamp (B). (C) shows the fingers illuminated from the backside. (D) clamp through one of the top pumping holes and (E) through one of the bottom holes

of the components in the straight section where COLDDIAG is installed. The horizontal position of the upstream taper and COLDDIAG is within ± 250 µm of the nominal beam axis. The vertical position has only a small negative offset of around 300 µm compared to nominal beam position. The deviations in the nominal position of the gate valves and the downstream components are much bigger and can only be tolerated because of the larger beam aperture of these components.

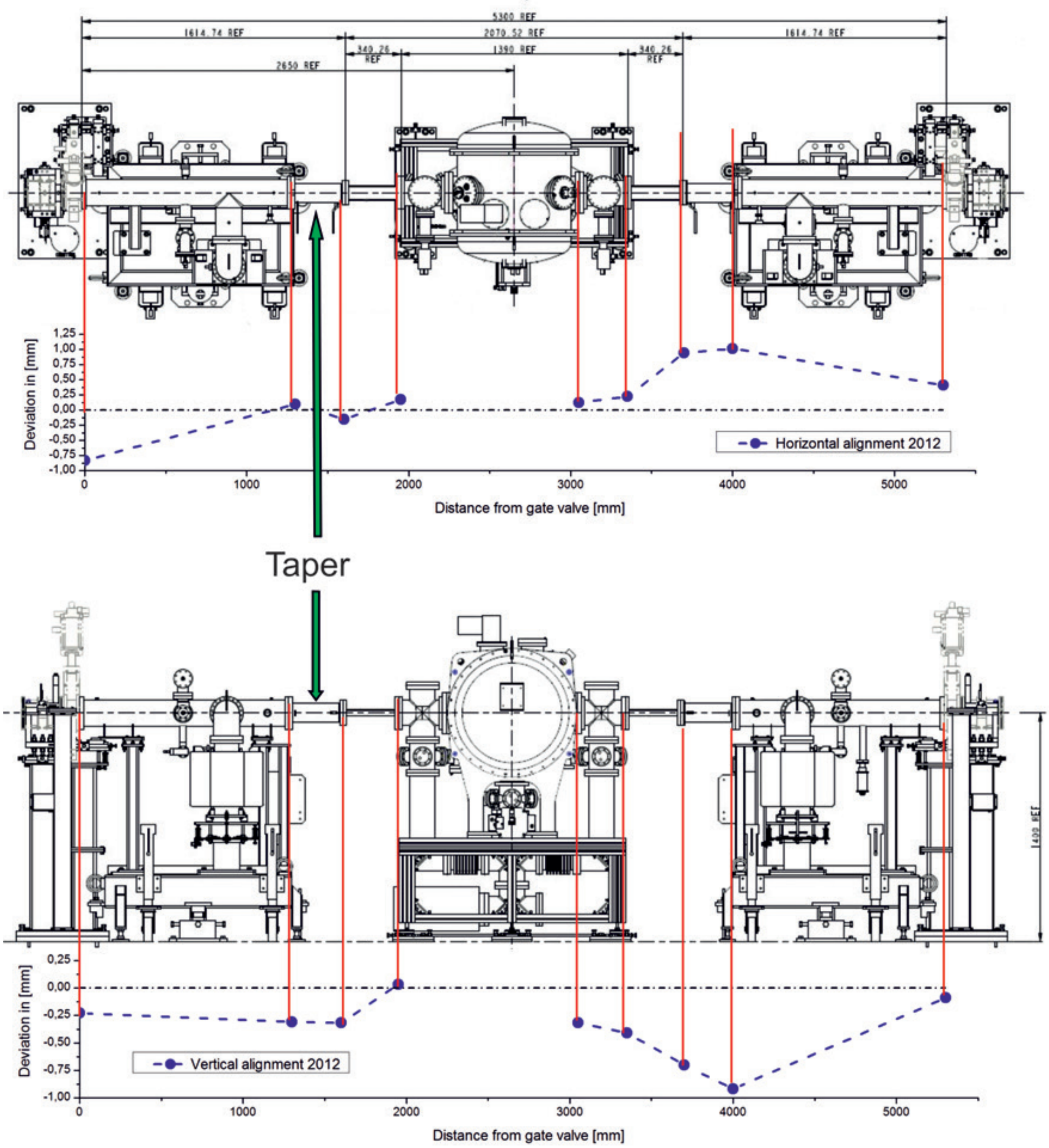

Figure 4.33: Measurement of the position of the components in the COLDDIAG straight. The upper picture shows the horizontal alignment, the bottom one the vertical alignment.

5

Chapter 5

Measurements and analysis

The experimental setup described in chapter 4 was used to measure the beam heat load under different beam conditions, including variable beam current, bunch length, beam position and fill pattern. Additionally, the total flux of charged particles impinging on the chamber walls, the energy spectrum of electrons and the influence of a solenoidal field on these particles, as well as the residual gas content were measured. While COLDDIAG was installed at the DLS in November 2011, only a small amount of data was collected. This happened mainly during the start up periode of the machine, before the thermal transition failed and COLDDIAG had to be removed. After reinstallation in August 2012 with a slightly modified vacuum chamber (see Sec. 4.6), data are now continuously taken during user beam operation. While in dedicated machine development times it has also been possible to set special beam conditions for measurements with COLDDIAG. In the following, the measurements and results obtained are presented and analysed.

5.1 Beam heat load

With COLDDIAG installed in the DLS storage ring, the main aim is to measure the heat deposited by the electron beam into the cold beam tube of the experiment. After a calibration procedure, the heat intake was measured for different beam conditions. This section presents the calibration, the beam heat load measurements and the results of the heat intake dependence on beam current, bunch length, vertical beam position and fill pattern. In order to determine the beam heat load, the temperature sensor located on the cooling connection between cryocooler and liner (see Fig. 4.12) is used. Small temperature gradients between the sensors located on the liner, which are due to unequal contact pressures, are responsible for different temperature sensor readings (always within ±0.2 K) without beam.

5.1.1 Calibration

In order to relate the measured temperature to the heat intake from the beam, the following calibration has been performed without beam. The cold liner sections and the cryostat were cooled down to the minimum base temperature reachable. After this, the heaters simulating the beam heating, which are mounted on the outside of the beam tube, were used to warm up the liner (see Fig. 4.12, 4.15 and Sec. 4.4.6). A similar procedure was used to perform the calibration for the warm sections. The lowest temperature reached during the first and second installations was 4.02 ± 0.25 K and 5.28 ± 0.25 K, respectively. The difference of around 1.3 K is caused by the thermal transition, which had to be redesigned for more rigidity, and thus gives less thermal insulation from the cryostat components at intermediate temperature at around 50 K to the liner at about 4 K. Figure 5.1 shows a calibration performed in November 2012 in the first shutdown during

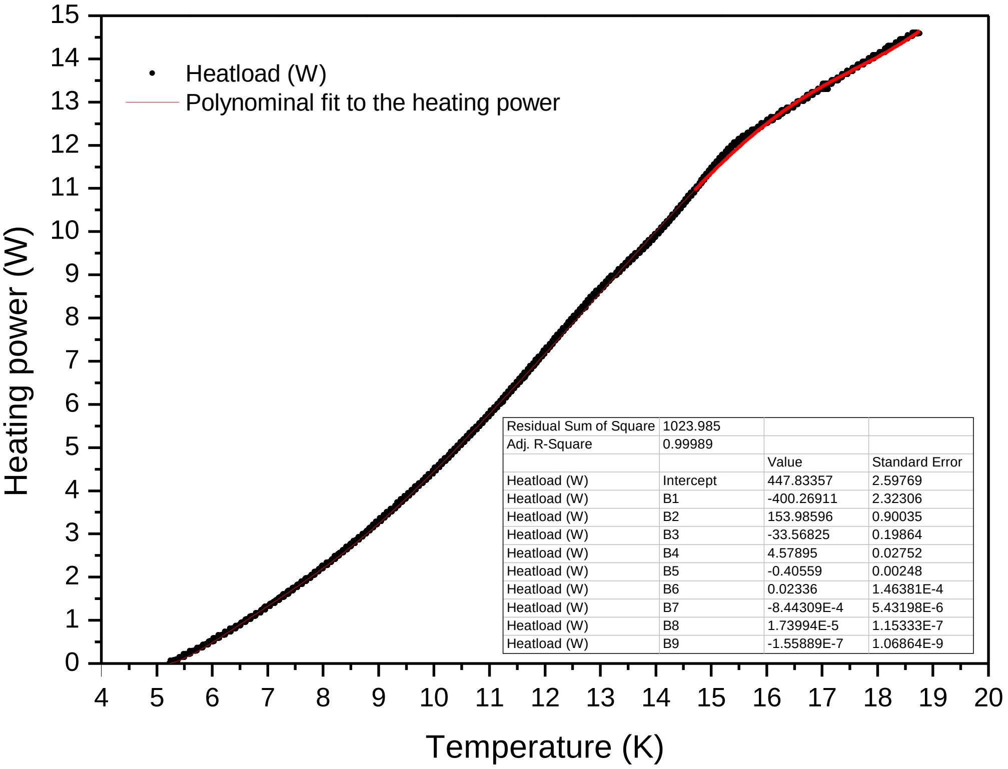

Residual Sum of Square	1023.985		
Adj. R-Square	0.99989		
		Value	Standard Error
Heatload (W)	Intercept	447.83357	2.59769
Heatload (W)	B1	-400.26911	2.32306
Heatload (W)	B2	153.98596	0.90035
Heatload (W)	B3	-33.56825	0.19864
Heatload (W)	B4	4.57895	0.02752
Heatload (W)	B5	-0.40559	0.00248
Heatload (W)	B6	0.02336	1.46381E-4
Heatload (W)	B7	-8.44309E-4	5.43198E-6
Heatload (W)	B8	1.73994E-5	1.15333E-7
Heatload (W)	B9	-1.55889E-7	1.06864E-9

Figure 5.1: Total heating power on the cold liner versus temperature during calibration, without beam (black dots) and polynomial fit of 9^{th} order to the measured data (red line).

the second installation. The sum of the power applied to the four heaters located on the cold liner is plotted against the temperature of the sensor located at the cooling connection between cryocooler and liner. A polynomial of 9^{th} order was used to fit the heating power to the temperature. The coefficients of the polynomial are reported in Fig. 5.1. The heating power is measured separately for each heater. The 4-wire measurement technique has been used to account only for the power dissipated in the heaters and not for the power consumed by the feed cables (see Sec. 4.4.6). The total power provided by the power supplies of the heaters was varied from 0 - 20 W in steps of 0.1 W. Figure 5.2 gives a detailed view of the temperature range from 6 K and 8 K of Fig. 5.1, showing the power steps of the heaters. The plateaus visible in the plot of the heating power are caused by a delay of the system reaching a new thermal equilibrium after increasing the power on the heater. In addition, Fig. 5.2 shows the residual of the polynomial fit to the heating power. It can be seen that the residual, representing the error of the calibration, is within +0.23 W and −0.15 W. In Fig. 5.3 the temperature is shown as a function of time. During this calibration, the power was increased every 30 min. This provides enough time to reach thermal equilibrium on the cold liner and to collect enough data points

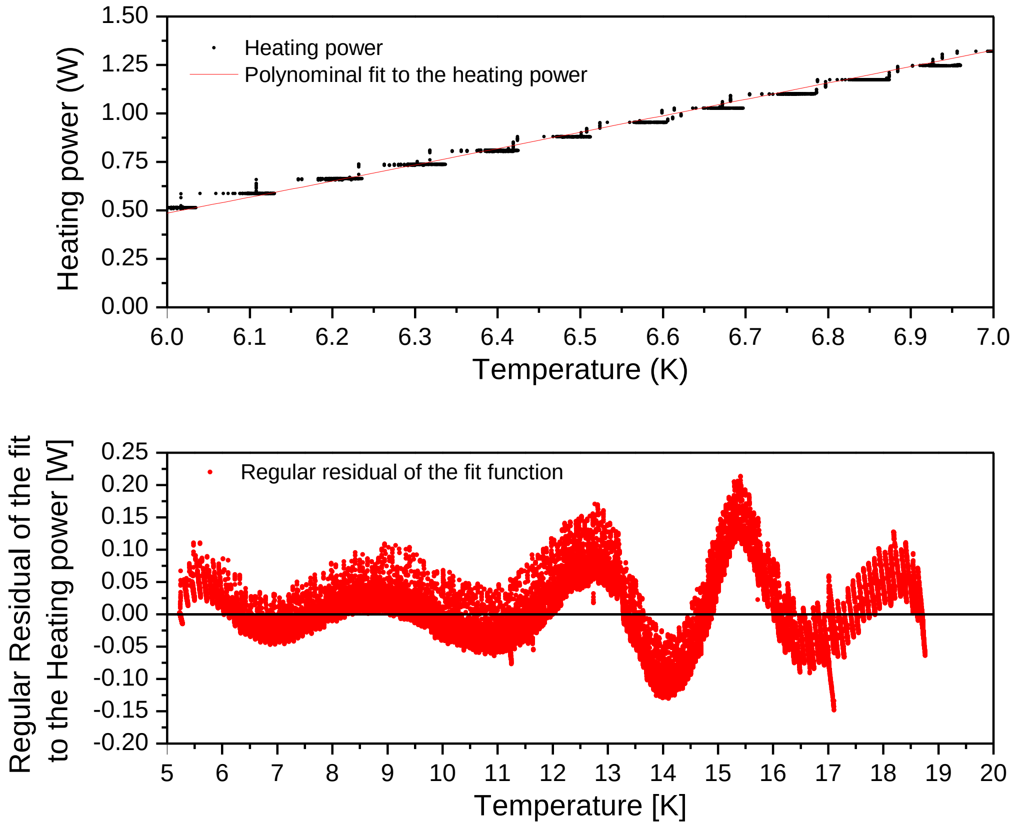

Figure 5.2: Detailed view of Fig. 5.1 between 6 K to 8 K showing the fit function and the power steps (top) and plot of the regular residual of the polynomial fit to the heating power (bottom).

for averaging over small temperature fluctuations. The temperature variations seen in Fig. 5.3 of around 35 mK are either due to electrical noise or caused by the cryocooler compression and expansion cycle. This cycle has a frequency of about 60 Hz, similar to the time between two consecutive readouts of the temperature sensors. A small or varying frequency difference between the cryocooler period and measurement could explain the structure seen in the temperature fluctuations.

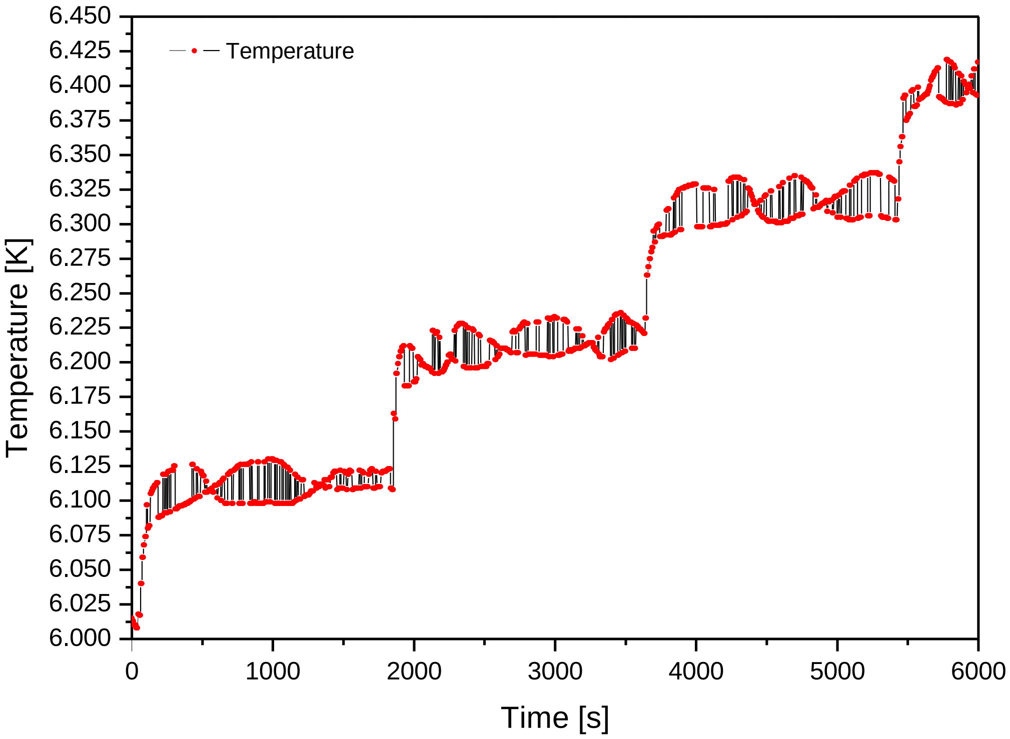

Figure 5.3: Temperature as a function of time during calibration.

5.1.2 Beam current dependence

The beam current dependence is one of the criteria for distinguishing between the different possible sources of beam heat load (see Sec. 3). The raw data of a typical beam current ramp are shown in the Fig. 5.4 for 460 consecutive bunches. The time between two current steps ranges from 15 min for small currents to 30 min for high currents, allowing the cold liner section to reach thermal equilibrium. To obtain the beam heat load from the raw data, only the measured temperature values in thermal equilibrium with constant temperature and constant beam current are needed. These values are chosen by a software selection algorithm. The program only chooses data points which are within a temperature band of ± 50 mK for at least 30 s. A second condition during this time interval is the value of the beam current staying within ± 2 mA. From the selected data only the last 120 temperature values measured in the two minutes before the next step in beam current are used and averaged. The other values are rejected to minimize the influence of the decaying beam and the time the system needs reaching thermal equilibrium. Finally, the 9$^{\text{th}}$ order polynomial obtained from the calibration (see Fig. 5.1.1) is used to determine the beam heat load from the resulting temperature values. As an example, the plot in

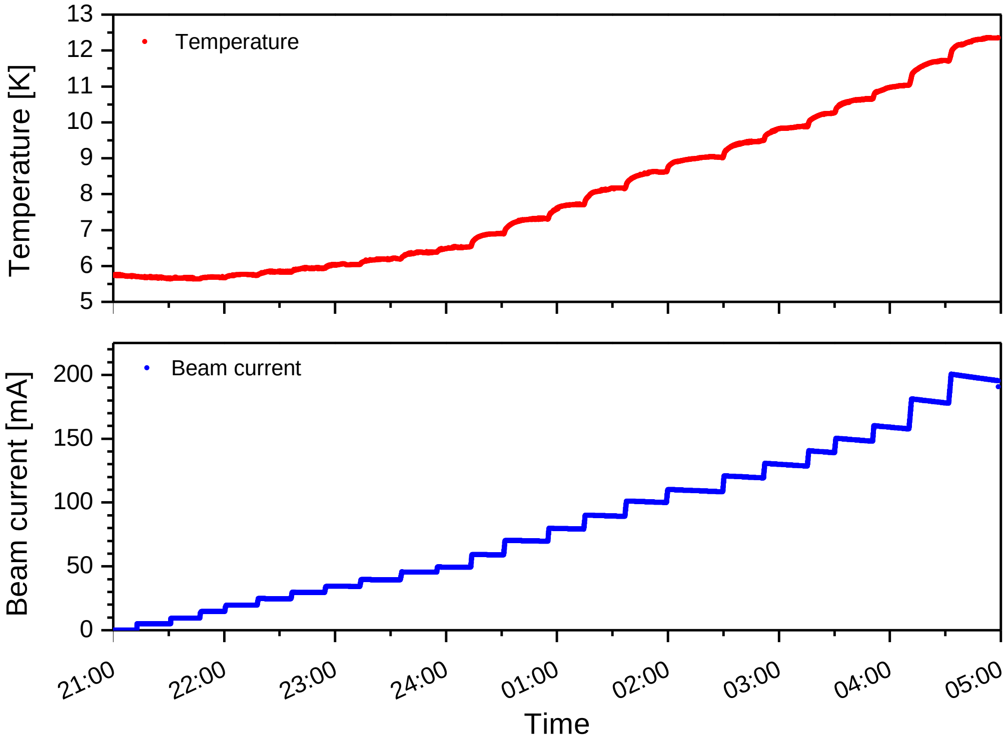

Figure 5.4: Temperature (top) and beam current (bottom) during the 460 bunch current ramp.

Fig. 5.5 shows the beam heat load for different beam currents and a fill pattern of 460 consecutive bunches. The error bars show the uncertainty in the measurement of the beam heat load derived from the calibration data. In section 5.1.7 a possible additional influence on the measurement coming from the thermal transition to the cold liner is discussed. At beam currents above 80 mA, a linear behavior of the beam heat load is observed, which excludes broad band impedance effects as main heating effect. Although the observed linear behavior is expected for synchrotron radiation heating, the quadratic dependence of the beam heat load at low currents, and the fact that the linear fit does not cross the origin of the plot, contradict the synchrotron radiation heating model (see Sec. 3). The plot also shows that the beam heat load expected from resistive wall heating for a RRR of 200 and a RRR of 10 calculated by using Eq. 3.7 is more than one order of magnitude smaller compared to the values measured.

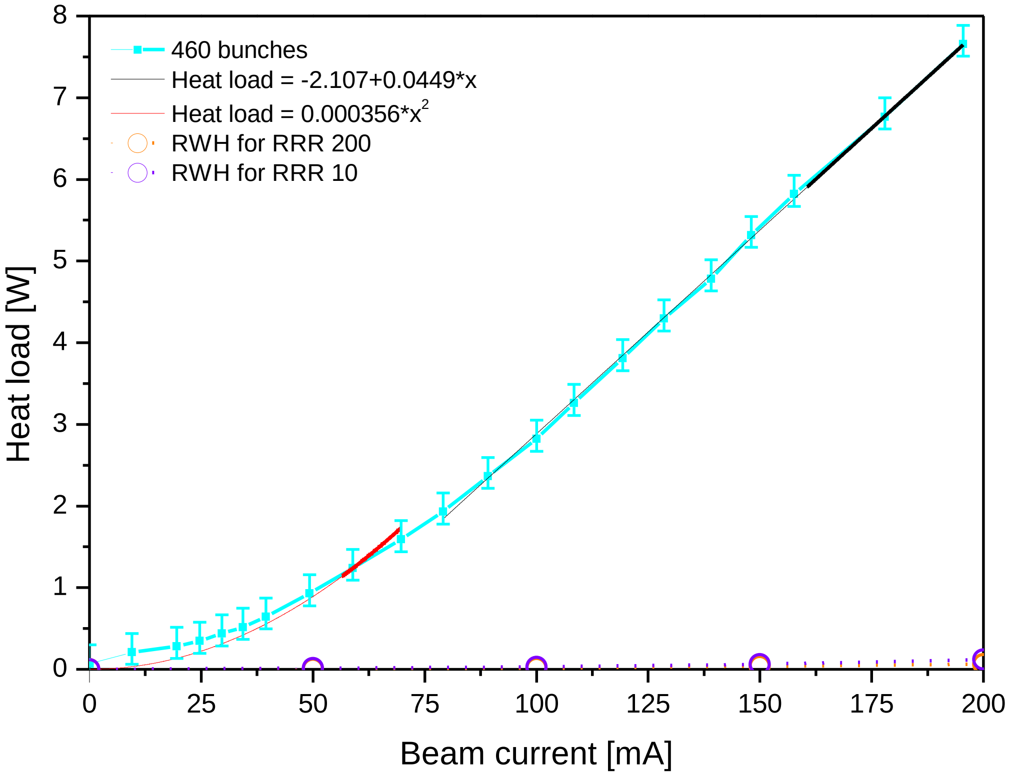

Figure 5.5: Beam heat load for 460 bunches plotted against the beam current (blue) and two fit curves one parabola to the data for beam currents lower than 80 mA (black line) and a linear curve fit to the data from 80 mA to 200 mA (red line). The beam heat load expected from resistive wall heating is also shown for a RRR of 200 (orange dotted line) and a RRR of 10 (blue dotted line).

5.1.3 Comparison between the measurements in 2011 and 2012

During the short installation in November 2011, the beam heat load current dependence for only one fill pattern was measured. Figure 5.6 shows a comparison of this measurement with a measurement obtained after the reinstallation of COLDDIAG in 2012 for the same fill pattern. The black curve displays the beam heat load for 900 consecutive bunches obtained with the old thermal transition in November 2011. During this beam current ramp, the superconducting wigglers were not powered, which results in a smaller energy spread, thus reducing the bunch length by about 5 % from 16.6 ps to 15.8 ps for a beam current of 250 mA [75, 76]. In contrast, for the measurement with the modified COLDDIAG (red curve) the wiggler magnets are powered. In section 5.1.5, the influence of the different bunch lengths with and without the wiggler magnets powered is presented, showing that the shorter bunch length, when the magnets are off, increases the beam heat load by about 11 % for a fill pattern of 686 consecutive bunches and a beam current of 250 mA. Taking into account the different bunch lengths, a comparison of the fill pattern with 900 consecutive bunches measured before and after the reinstallation also shows a difference of

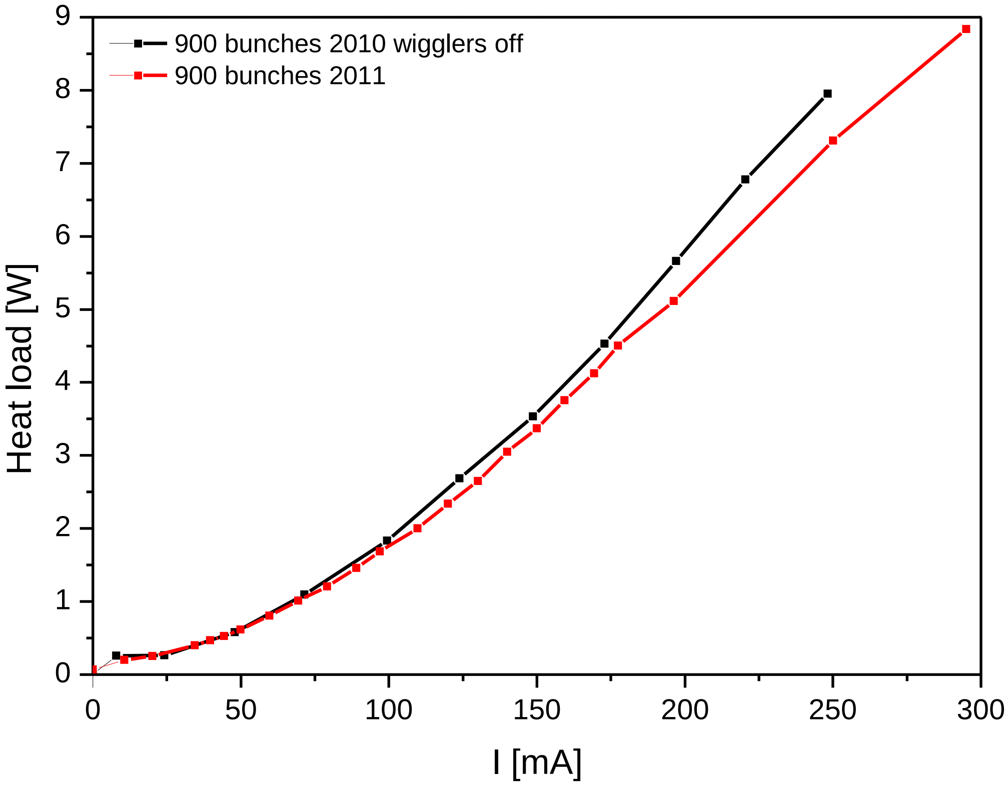

Figure 5.6: Beam heat load for 900 bunches measured 2010 (black curve) and after modification and reinstallation in 2011 (red curve).

about 10 %.

5.1.4 Fill pattern dependence

During the installation, the beam heat load dependence on various fill patterns and different beam currents has been investigated. In order to stay within safe operational parameters of the DLS storage ring, the total beam current was limited to 300 mA and individual bunch charge to 0.82 nC with the possibility to add one special bunch with a charge of upto 3 nC. Furthermore, the sum of the bunch charge Q_b squared (SOCS), defined by $\sum^{N_b} Q_b^2$ had to be below 470 nC^2. These parameters are the maximum values reached during user operation with the so-called hybrid fill pattern consisting of 686 sequent bunches and a single 3 nC bunch after the train. Figure 5.7 shows the beam current dependence for 230, 460 and 900 successive bunches. For all three fill patterns the magnets of the superconducting wigglers installed in the DLS storage ring were powered. For the same current, when the magnets are powered, the energy spread and the length of the stored bunches become larger. Therefore, because of the beam heat load dependence on the bunch length (see Sec. 5.1.5), a direct comparison between the current ramps with different status of the wigglers is not possible. The plots in Fig. 5.7 demonstrate that the beam heat load increases with the current per bunch. However, the beam heat load is not scaling linearly with the inverse number of bunches as expected from broad band impedance effects (see Sec. 3.2). Figure 5.8 shows a comparison of the beam heat load measured for fill patterns with different bunch spacing. The 936 buckets of the DLS are spaced by 2 ns defined by the cavity frequency of 500 MHz. The bunch spacing for consecutive bunches is 2 ns. By filling every second (or fourth) bucket the bunch spacing is 4 ns (8 ns). A significant influence of bunch spacing is not observed. This suggests we can exclude a narrow band resonance as the main heat load source.

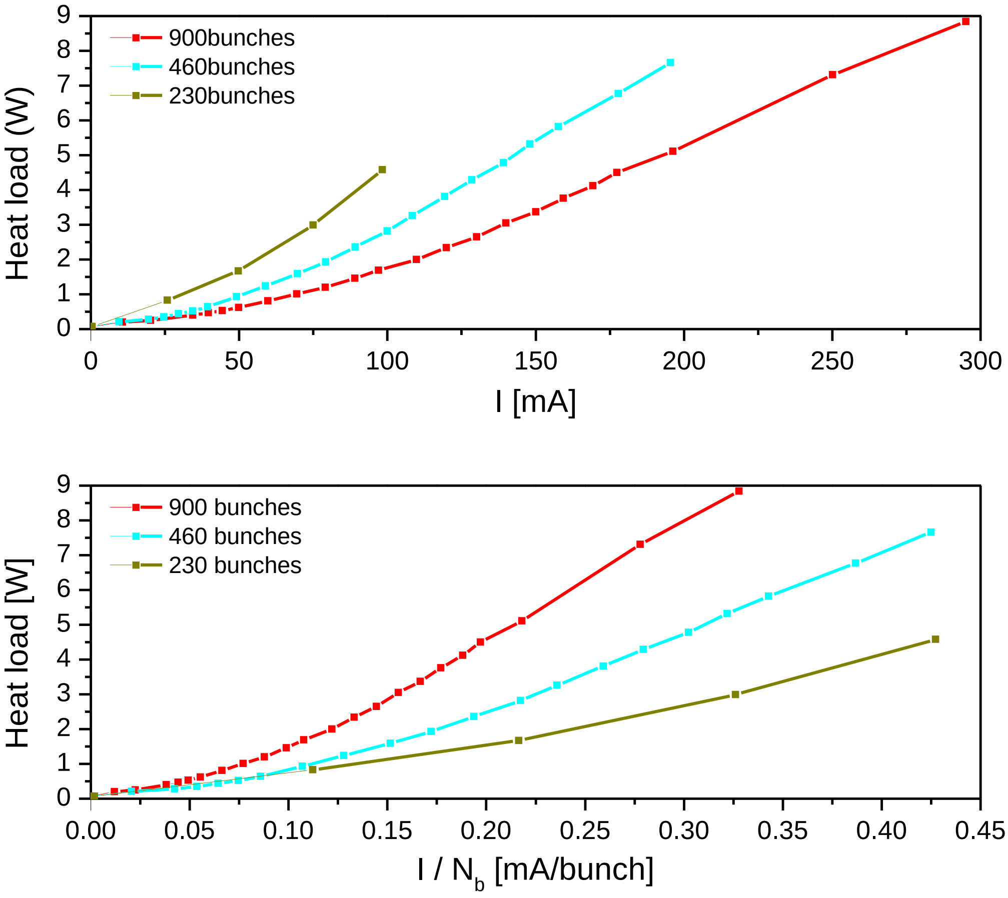

Figure 5.7: Heat load dependence, for fill patterns with 230, 460 and 900 consecutive bunches, on the beam current (top) and on the current per bunch (bottom).

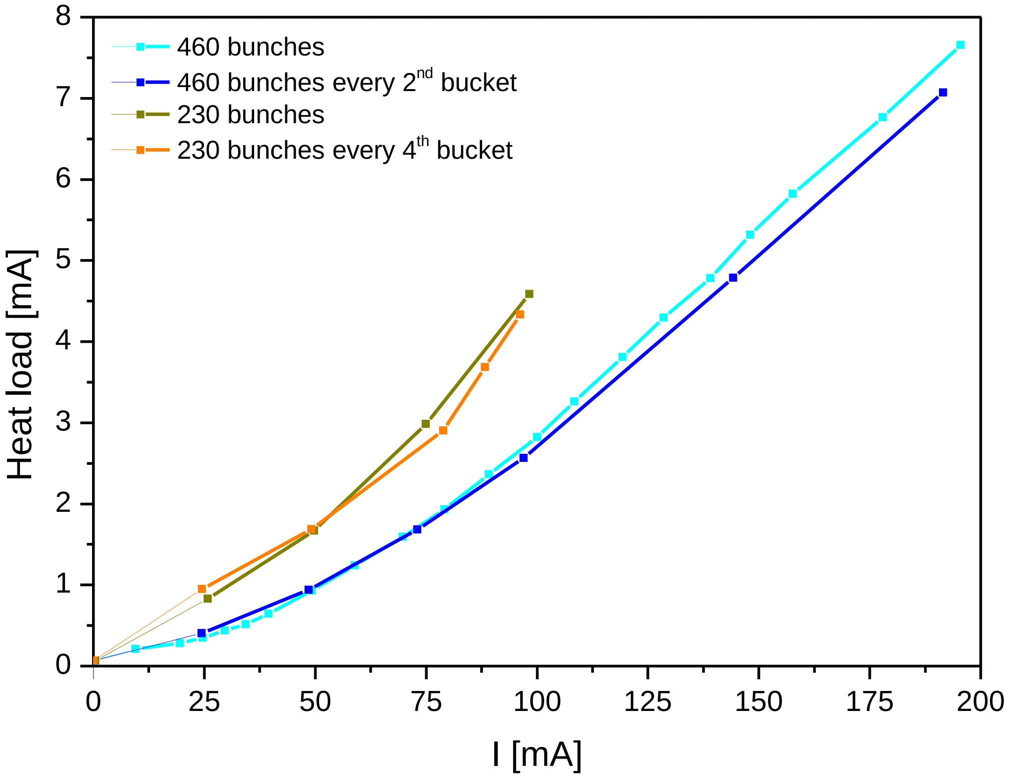

Figure 5.8: Heat load plotted against beam current for fill patterns with different bunch spacings.

5.1.5 Bunch length dependence

Analytical formulas for impedance effects predict a strong dependence of the beam heat load on the bunch length. Within this work, the bunch length was changed by powering the coils in the two superconducting wigglers. In this way, for constant beam current only two different bunch lengths could be investigated. By varying the RF cavity voltage, the bunch length can be changed over a wider range. However, more allocated machine development time is necessary for this measurement. In Fig. 5.9 the difference in beam heat load for a fill pattern of 686 consecutive bunches with the wiggler magnets powered and unpowered is displayed. With the wiggler coils at nominal field, the energy spread of the machine and thereby the bunch length increases by about 5 % from 17.0 ps to 17.9 ps, for a fill pattern of 686 consecutive bunches and 300 mA beam current [75, 76]. The plots show that the heat load at 300 mA is more than 1 W higher with the wigglers off compared with the wigglers on.

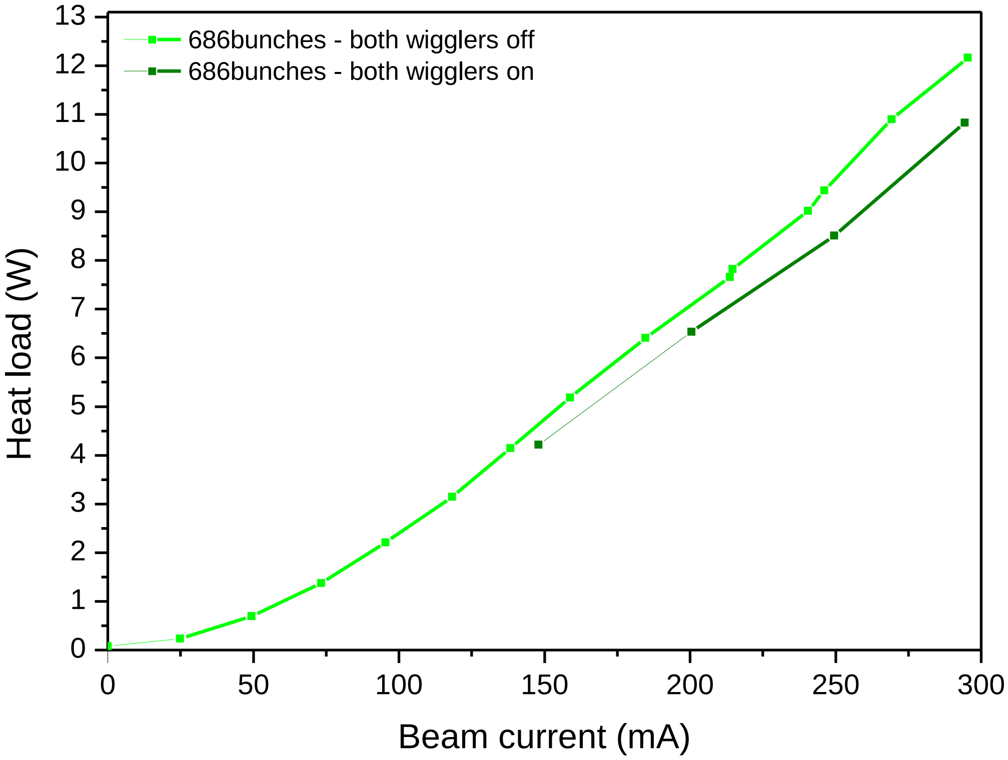

Figure 5.9: Heat load for 686 bunches with wigglers on and off for several beam currents.

In addition to the dependence on the wiggler field, the bunch length also increases with increasing current per bunch. Figure 5.10 shows the bunch length plotted against the current per bunch for a fixed cavity voltage of 2.5 MV. The data in the plot are taken with the wigglers powered and all insertion devices closed. The bunch length was measured with a streak camera by the DLS diagnostic group in June 2012. The fit shown with the data points is used in the following analysis. All data for this work were recorded with a cavity voltage of 2.5 MV. Figure 5.11 shows the beam heat load plotted against

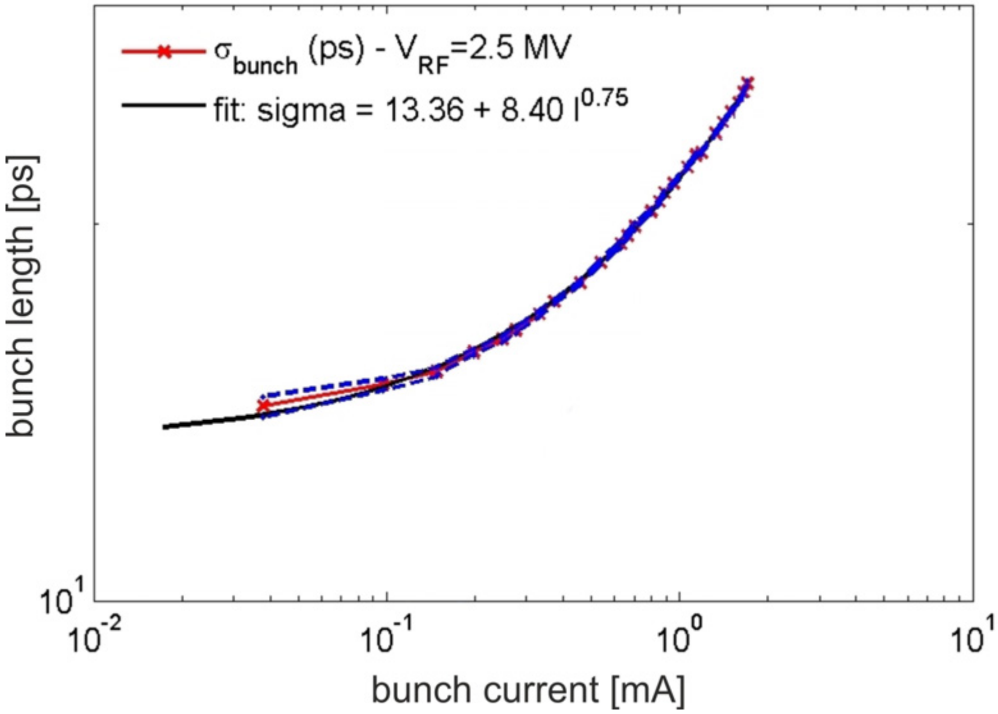

Figure 5.10: Bunch length in ps plotted against the bunch current in mA for a cavity voltage of 2.5 MV. The black curve is a a fit to the measured data. Courtesy of C. Thomas, DLS diagnostic group.

$\frac{I^2}{N_b}$ and different bunch length dependencies: $\frac{1}{\sigma}$, $\frac{1}{\sigma^{3/2}}$ and $\frac{1}{\sigma^{5/3}}$. A dependence on $\frac{I^2}{N_b}\frac{1}{\sigma}$ would indicate a step transition or symmetric tapers as the dominant heating source, while the $\frac{I^2}{N_b}\frac{1}{\sigma^{3/2}}$ dependence is typical for a resistive impedance in the normal skin effect regime, and $\frac{I^2}{N_b}\frac{1}{\sigma^{5/3}}$ for a resistive impedance in the anomalous skin effect regime [36]. However, the plots in Fig. 5.11 show no linear behavior and thus no agreement with a of the three models. Moreover, analytical and numerical calculations taking into account the geometrical and resistive wall impedance for the given structure, predict much smaller values of the beam heat load than the ones observed (by approximately one order of magnitude) [36].

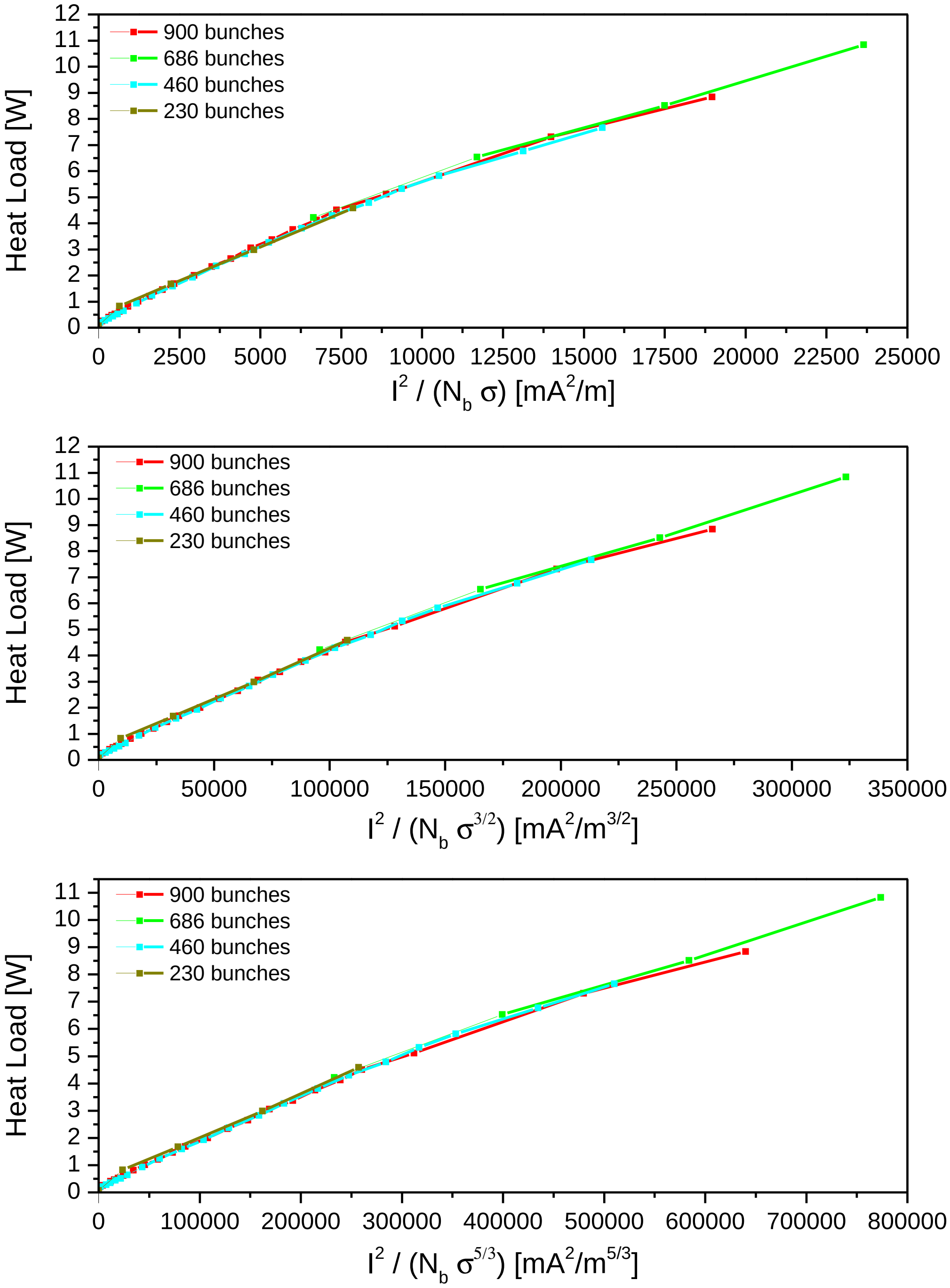

Figure 5.11: Heat load plotted against $\dfrac{I^2}{N_b}\dfrac{1}{\sigma}, \dfrac{I^2}{N_b}\dfrac{1}{\sigma^{3/2}}$ and $\dfrac{I^2}{N_b}\dfrac{1}{\sigma^{5/3}}$.

5.1.6 Beam heat load during user operation

The DLS storage ring is normally run for user operation in top–up mode for 24 h and 6 days per week with a refill every 5 min to 15 min. The data presented in this section have been measured with fill patterns of 686 and 900 sequential bunches and an average beam current of 300 mA. The user run provides the possibility to investigate the beam heat load on the warm sections, which need around 48 h to reach thermal equilibrium, whereas the cold section needs less than 1 h. Additionally, the beam heat load dependence in the cold section over an extended period of time, with similar beam conditions, can be investigated.

Beam heat load in the cold section

Figures 5.12 and 5.13 show the temperature of the cold section during user operation with 900 and 686 bunches. Both plots show that after a fast increase in temperature in the first 30 min after the injection, it then takes around 12 h to 24 h to slowly increase in temperature until the cryostat and the cold section reach thermal equilibrium. The cold section always reaches the same maximum temperature of 15.6 K with a fill pattern of 686 bunches and 14.3 K with 900 bunches, which correspond to a heat load of 12.1 W and 10.4 W, respectively. The values for the long run are about 1 W higher than the values obtained for the same fill patterns during the current ramps (see Fig. 5.9, 5.7). The difference in heat load is most probably due to the fact that the cold section is not perfectly thermally uncoupled from the surrounding cryostat. The components which are connected to the shield at around 50 K and the warm stage of the cryocooler warm up relatively slowly (about 12 h to 24 h) because of their mass and heat capacity. This extra heat load partially flows over the thermal transition from the 50 K shield to the cold mass (see Sec. 4.3). Furthermore the dependence of the cold stage cooling power from the warm stage temperature (see Fig. 4.4) can give a slightly higher temperature of the cold section.

Beam heat load in the warm section

The warm sections of COLDDIAG are thermally isolated from the environment and not actively cooled. This results in a long time of around 48 h being needed to reach thermal equilibrium. Eight temperature sensors are placed on each warm section. Figure 5.14 and 5.15 show the mean temperature measured on the upstream and downstream warm sections. In the upstream warm section, one sensor is shorted to ground so that only seven sensors are used to calculate the average temperature on the liner. A calibration procedure similar to the one performed in the cold section is used for the each of the two warm sections to derive the beam heat load from the measured temperature. For user operation with a fill pattern of 686 consecutive bunches (see Fig. 5.15), the temperature in the downstream warm section saturates at around 310 K. This behavior is probably caused by a thermal contact between the liner and the vacuum chamber at ambient temperature which develops due to thermal expansion of the warm liner. Therefore, the downstream warm section cannot be used to determine the beam heat load.

Using the calibration for the upstream warm section, a heat load of 3.2 W for a fill pattern of 686 consecutive bunches and of 2.8 W for 900 sequential bunches is obtained. Comparing the long run beam heat load values measured in COLDDIAG and taking into account the different lengths of the warm and the cold sections, the beam heat load in the cold section is around twice as big as in the warm sections per unit length. In addition, the beam heat load in the warm section, just as in the cold section, is not proportional to the inverse number of bunches. However, the ratio of the heat intake measured for a fill pattern of 900 and 686 consecutive bunches in the warm sections $\frac{P_{900}}{P_{686}} = 0.86$ and in the cold sections $\frac{P_{900}}{P_{686}} = 0.84$ is very close, which might indicate the same beam heat load dependence.

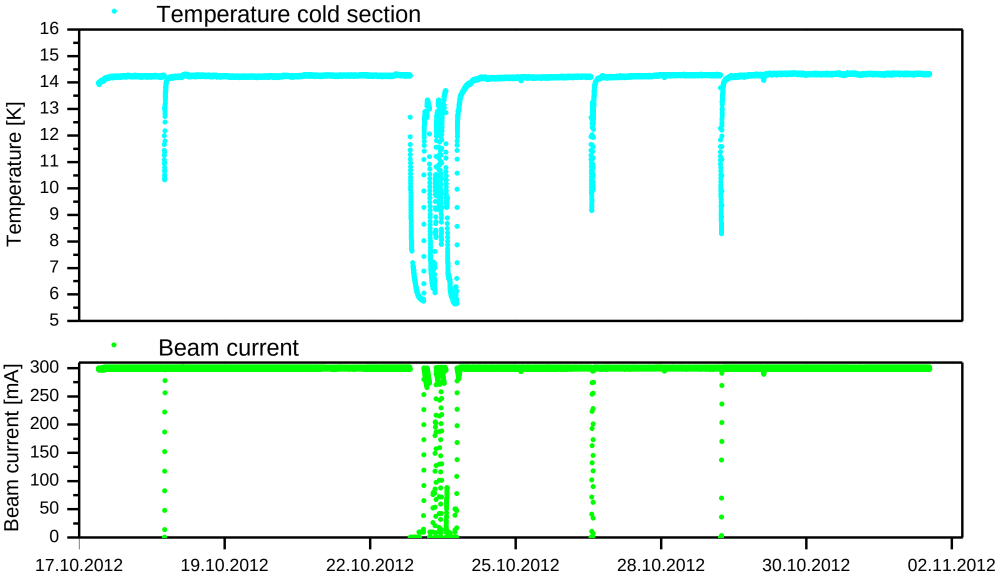

Figure 5.12: Temperature in the cold section measured during user operation with 900 bunches as a function of time.

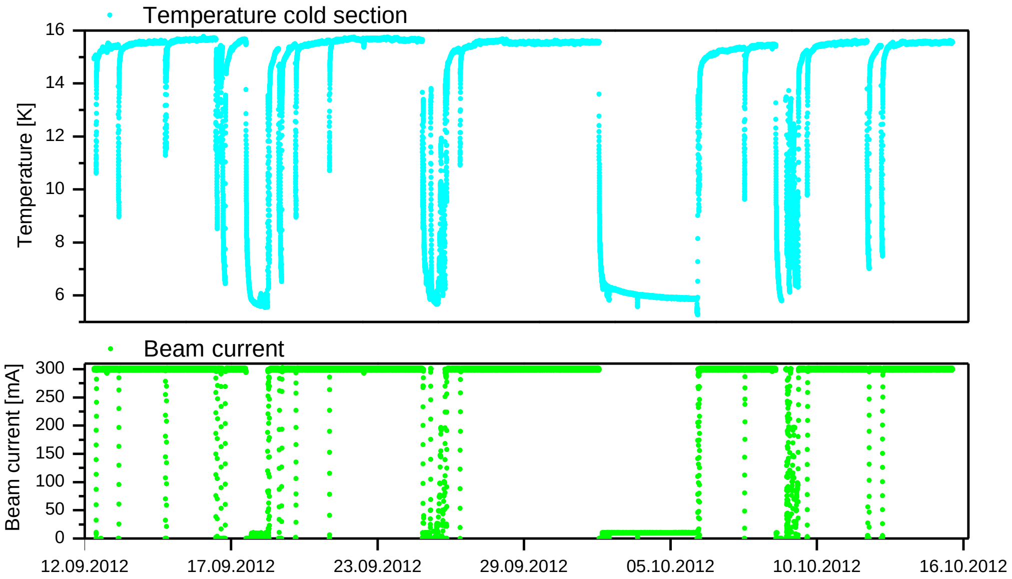

Figure 5.13: Temperature in the cold section measured during user operation with 686 bunches as a function of time.

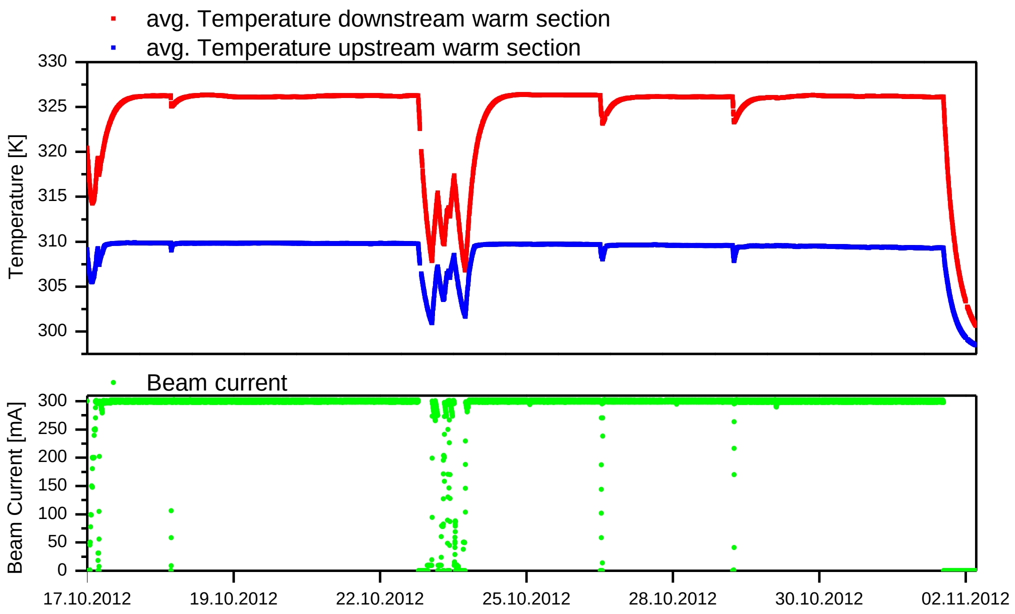

Figure 5.14: Average temperature measured during user operation with a fill pattern of 900 consecutive bunches on the upstream (red) and downstream (blue) warm sections as a function of time.

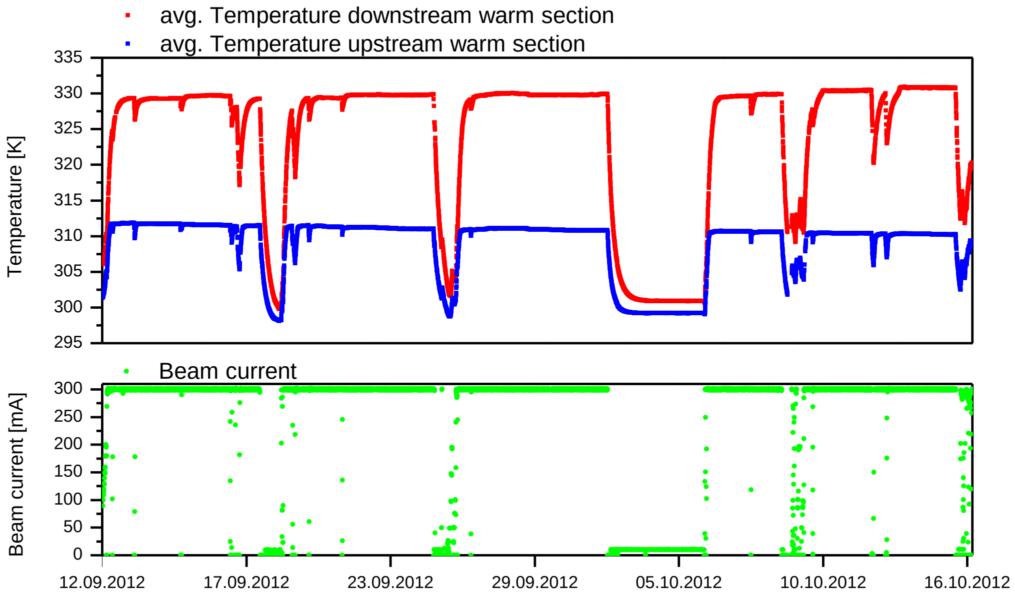

Figure 5.15: Average temperature measured during user operation with a fill pattern of consecutive 686 bunches on the upstream (red) and downstream (blue) warm sections as a function of time.

5.1.7 Possible influence of the thermal transition

The lowest temperatures without beam reached during the first and second installations were 4.02 ± 0.25 K and 5.28 ± 0.25 K, respectively. The higher base temperature in the second installation was caused by the redesigned thermal transition from the RF-bellows at around 50 K to the cold liner section (see Sec. 4.6). To improve and guarantee the electrical contact for the image currents the changes also lead to more point contacts, which resulted in a better thermal link between the RF–bellows and the cold section. Assuming only a negligible heat intake from the thermal transition before the changes were applied, the calibration made in the first installation can be used to determine the additional heat load in the new design. From this calibration, a liner base temperature T_{liner} of 5.28 K corresponds to an extra heat intake Q of 0.64 W from the two thermal transitions at $T_{transition}$ 34 K. With these values, a thermal conductance λ can be defined for the each of the transitions as

$$\lambda_{transition} = \frac{Q}{(T_{transition} - T_{liner})}. \tag{5.1}$$

With the additional assumption that the thermal contact conductance is linear over the temperature range of interest, the heat intake from the transition depends only on the temperature difference $\varDelta T$ between RF–bellows and cold liner and can be calculated by

$$Q = \lambda_{transition} \varDelta T. \tag{5.2}$$

This temperature difference can be measured by the temperature sensors installed on both sides of the transition. Figure 5.16 compares the beam heat load measured with a fill pattern of 686 consecutive bunches as a function of beam current with and without the influence of the transitions. The largest gradient over the thermal transition is observed for this fill pattern.

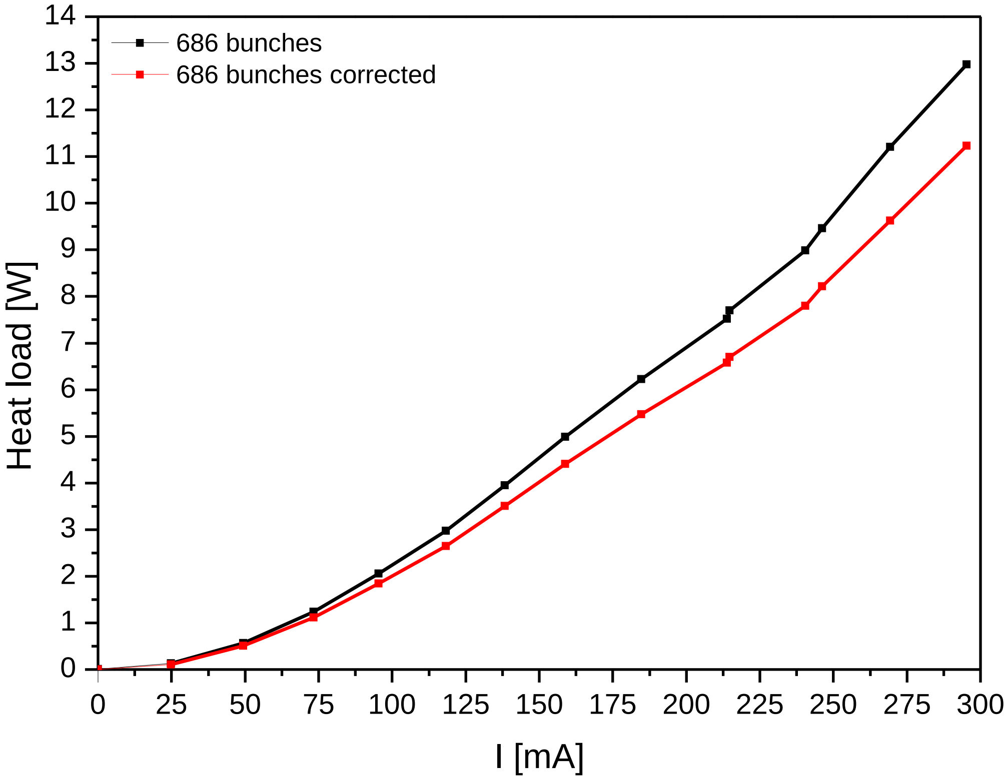

Figure 5.16: Comparison of the beam current ramp with a fill pattern of 686 consecutive bunches, with and without correction for the heat intake from the thermal transition.

For the beam heat load as a function of beam current with a fill pattern of 686 consecutive bunches, a maximum deviation of about 1.8 W results from the correction. The shape of the plot has not changed, which suggest only a small influence from the thermal transitions. However, offline tests with additional heaters on the warm side of the thermal transitions are planned after the removal of COLDDIAG, to experimentally determine the heat intake from the intermediate temperature regions to the cold liner.

5.2 Electron flux and energy spectrum

Three similar retarding field analysers (RFAs) are installed in COLDDIAG: one in the upstream, one in the downstream, and one in the cold section (see Fig. 4.12). The RFAs can be used to measure the energy spectrum of the electrons impinging the chamber wall or the total flux of charged particles, when the retarding grid is grounded. For the measurements of the energy spectrum two different readout techniques - an electrometer and a lock-in amplifier have been used (see Sec. 4.4.1). The results are presented in the following.

5.2.1 Electron flux

The flux of electrons hitting the chamber walls have been measured for various fill patterns and different beam currents. Figure 5.17 shows the electron flux measured on the three RFAs with 900 bunches. The collector was biased with +50 V. The electron current detected on all three RFAs exhibits a linear behavior with beam current. The amount of particles detected with the downstream RFA are almost twice that detected with the upstream RFA. Additionally, the downstream RFA shows a higher signal compared to the one of the cold section. In Fig. 5.18, the measured flux on each RFA is plotted against the beam current for different fill patterns. Similar to the plots in Fig. 5.17, the linear dependence on the beam current can be seen for all fill patterns. For 686 bunches, a difference in electron flux when the wiggler magnets are powered, which increases the bunch length, is observed. This indicates a dependence on the energy spread and/or the bunch length. The data obtained for the fill patterns with wigglers off can be divided in

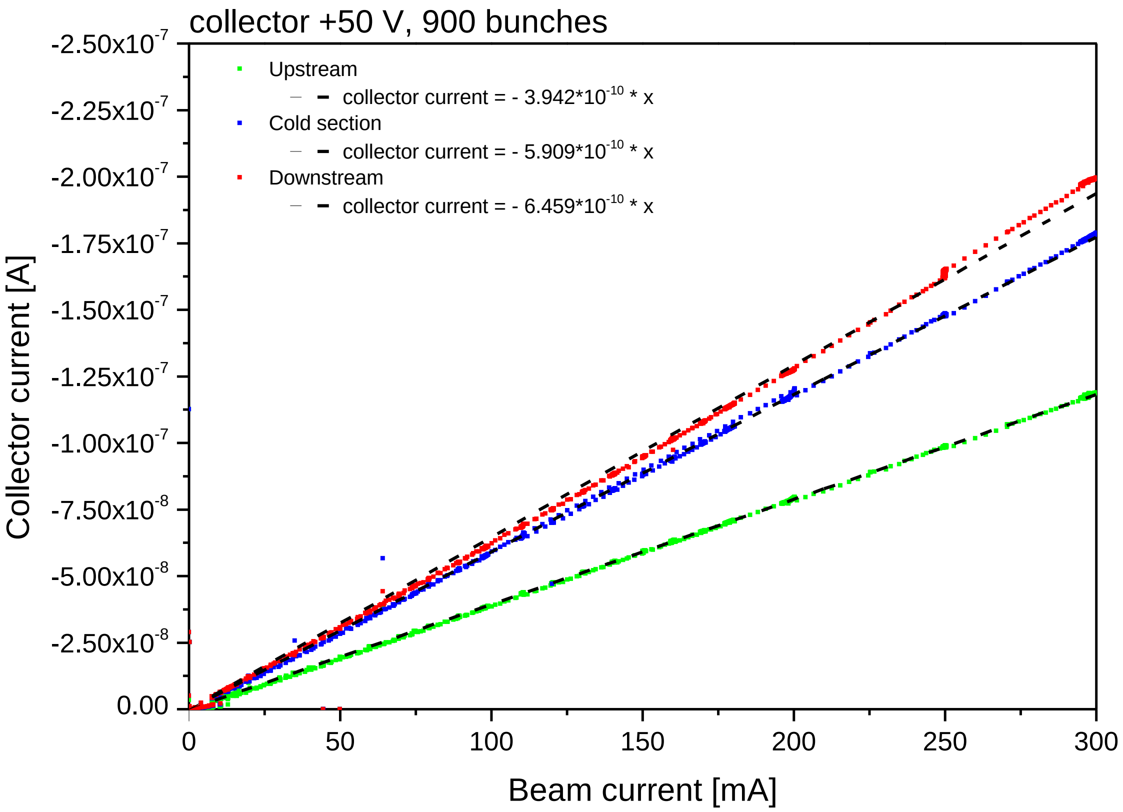

Figure 5.17: Flux of charged particles detected on the three RFAs with positively biased collector (+50V) for a fill pattern with 900 consecutive bunches as a function of the beam current.

two groups which show dissimilarities in the measured electron current. The same electron flux is measured for the fill patterns with 900, 460 and 686 consecutive bunches with the wigglers off. A similar flux is also measured for the second group: the fill patterns with 460 consecutive bunches and every second bucket filled, the 230 bunch fill pattern with every forth bucket filled and the 230 bunch fill pattern with consecutive bunches. Although during the current ramp with a fill pattern of 460 consecutive bunches only a few points have been recorded in the flux measurement mode of the RFA, a larger amount of electrons has been detected compared to the fill pattern with 460 bunches and every second bucket filled. This behavior indicates a dependence of the electrons hitting the collector plate on the bunch spacing. However, for the fill pattern with 230 bunches and every fourth bucket filled and the 230 bunch pattern with successive bunches no significant difference in the electron flux can be found. A dependence of the electron flux on the bunch spacing is not expected for electrons generated by synchrotron radiation (see Sec. 3.1). In contrast, the observed linear dependence of the electron flux with the beam current for all fill patterns is the same as the one predicted for photo electrons from synchrotron radiation.

5.2.2 Electron energy spectrum

To obtain the energy spectrum of the electrons detected by the retarding field analyser, two measurement techniques are available in COLDDIAG. Figure 5.19 and 5.20 show the electron spectra measured with both setups on the three RFAs installed in the upstream and downstream warm sections, and in the cold section of COLDDIAG. At the time of the measurements, the machine was run with a fill pattern of 686 consecutive bunches at 300 mA in top–up operation.

To obtain the data for Fig. 5.19, the negative retarding voltage is changed from 0 V to 250 V in steps of 100 mV. For each retarding voltage, the data are taken for one RFA after the other. The collector plate is biased with +50 V and the current is measured with a Keithley 6514 electrometer. The RFA setup works as a high pass filter, rejecting all electrons with energies below the retarding voltage. To obtain a spectrum, the derivative of the current measured for two consecutive energies has to be calculated. The spectra presented in Fig. 5.20 are obtained with a lock-in amplifier with a frequency of 353 Hz, an amplitude of 100 mV, and a phase of -157.29 deg. The retarding voltage is changed from 0 V to 250 V, in steps of 200 mV for one RFA after the other. The collector plate is biased with +84 V against ground.

The plots in Fig. 5.20 show the absolute value calculated from the real and imaginary part detected by the dual phase lock-in amplifier. Although the measurements performed with the lock-in amplifier have less noise than the spectra measured with the Keithley electrometer, the spectra reveal the same features. The measurements show that most electrons hitting the RFAs have energies below 10 eV. A zoom into the energy range 0-10 eV displays in the upstream and downstream warm section a peak of the spectrum around 1 eV in the inset figure. Similar behavior has been observed with the room temperature RFA installed at ANKA [68]. On the contrary, the RFA spectrum in the cold section shows a broader peak around 3.5 eV. Using Eq. 3.20, a rough estimate of the heating power created by electron bombardment can be obtained by assuming that all electrons hitting the cold RFA have a peak energy of 3.5 eV. By considering the measured energies and flux, the resulting heat load is less than 1 mW. However, the measured energy spectrum and total flux might only show a fraction of the electrons hitting the wall because the maximum detectable energy is limited to 250 eV. Moreover, the location of the RFAs could be unfortunate and the small acceptance angle of the RFA for particles with high energies traveling with a velocity component in beam direction might also limit the number of detected electrons.

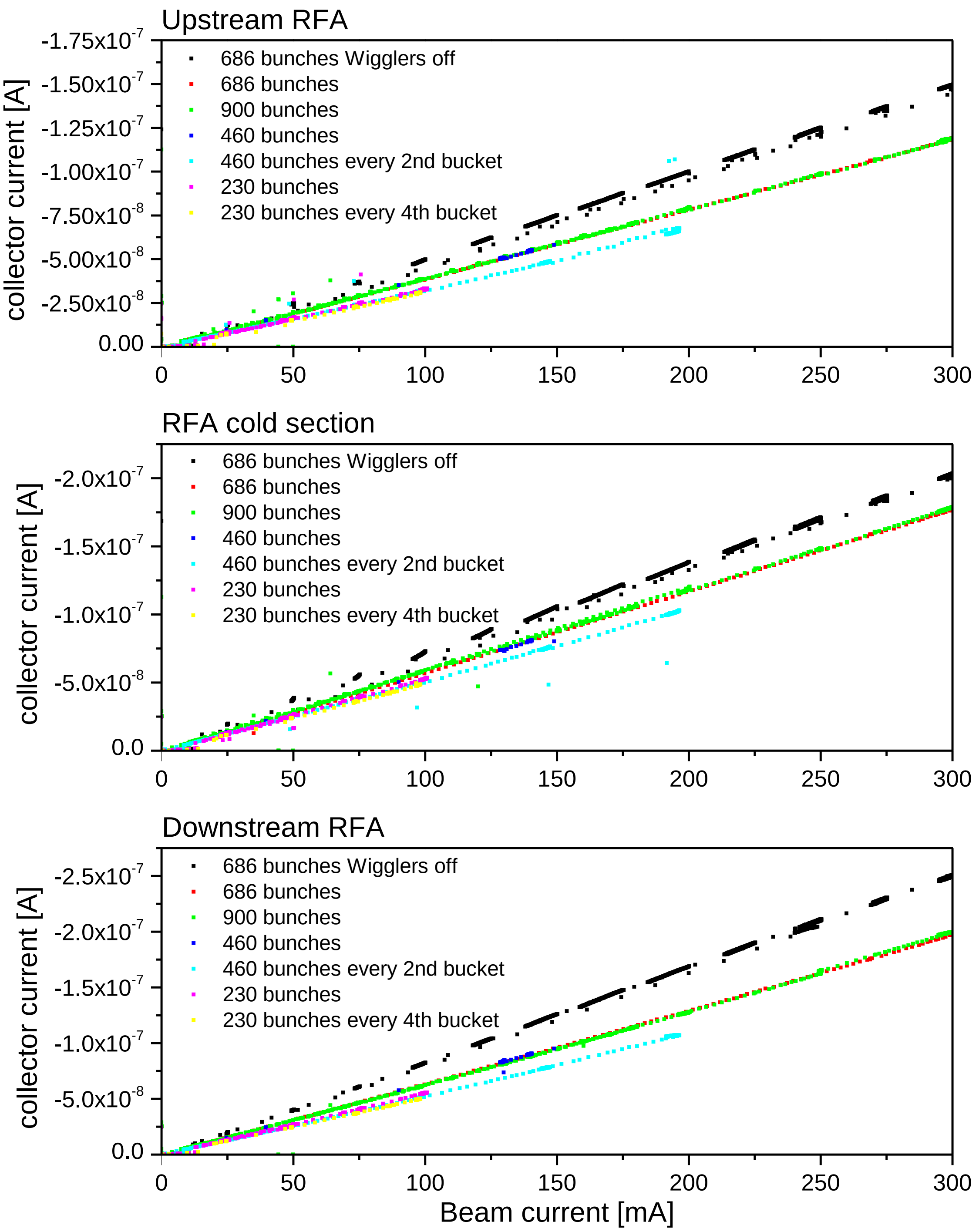

Figure 5.18: Collector current on the three RFAs for different fill patterns. The collector is biased with +50V.

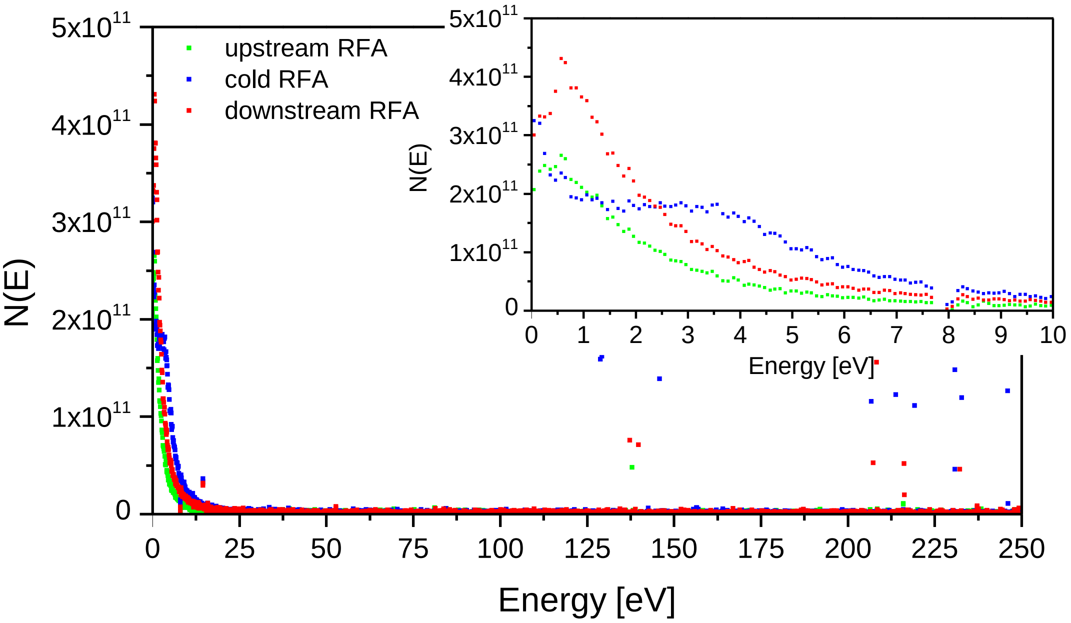

Figure 5.19: Energy spectrum of electrons detected on the three RFA's with the Keithley 6514 electrometer.

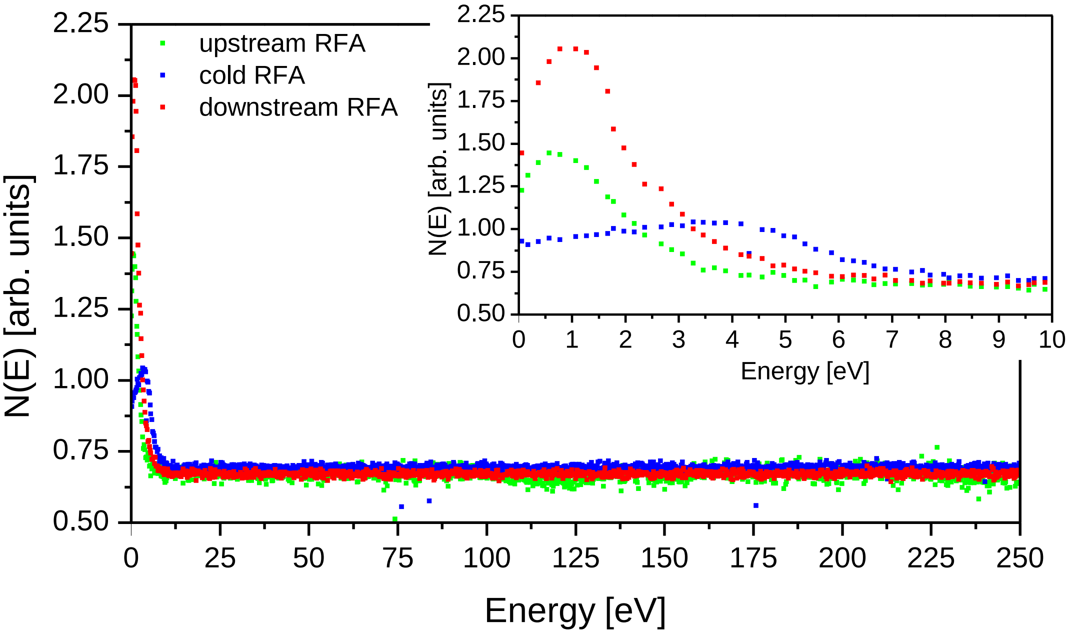

Figure 5.20: Energy spectrum of electrons detected on the three RFA's with the lock-in amplifier technique.

5.3 Influence of the magnetic field of the solenoid

A 160 mm long solenoid, which can produce a maximum magnetic field on axis of about 10 mT, is installed on the downstream arm of the cold six-way cross. This magnet can be used to suppress charged particles impinging the wall by modifying their trajectories (see Sec. 4.4.2). The magnetic field applied is parallel to the beam axis. Depending on the polarity of the electric current, the field is pointing in the beam direction or opposite to it. To measure the particle flux, the retarding grid of the RFA was set to ground and the collector plate was biased with -50 V or +50 V.

Figures 5.21, 5.22, 5.23 and 5.24 show the influence of the solenoidal field on the liner temperature and the flux of charged particles. The flux was measured in the upstream and downstream warm section and in the cold section. For the data presented in Fig. 5.21 and 5.22, the collector is biased negatively whereas for the data in Fig. 5.23 and 5.24 the collector is biased positively. During data acquisition, the storage ring was operated in top-up mode with a nominal beam current of 300 mA, a fill pattern of 686 consecutive bunches and a refill every 10 min. Before the measurement was started, the cryostat did not reach perfect thermal equilibrium. Therefore, during the experiment the temperature is rising about 0.5 K, as can be seen in the plots.

Figure 5.21 shows the flux of positively charged particles during a ramp of the electric current in the solenoid. The collector current measurements show a small enhancement of the particle flux in the cold, while there is no change of the signal from the upstream and downstream warm section. The temperature chart follows the top-up mode of the beam current. A small increase of less than 200 mK is visible at around 16:40. This could be associated with a delay of about 5 min between increasing the collector after increasing the solenoid current.

The data presented in Fig. 5.22 are taken with the collector still biased negatively, but with the magnetic field direction inverted. The flux of positive ions in the cold section is suppressed by the magnetic field, whereas again no influence is visible in the warm parts. Here also a small increase in temperature of around 300 mK is noticeable while the solenoid is powered.

For the measurement shown in Fig. 5.23, the collector is biased positively to collect negatively charged particles. The magnetic field is pointing in the same direction as in figure 5.21. While the upstream RFA shows no response to the increasing magnetic field, in the downstream warm section the flux is slightly increased. However, the current of negative particles measured in the cold section at first increases for small magnetic fields and then decreased. Approximately 200 mK higher temperature can be seen again while the solenoid is powered.

Figure 5.24 presents the flux and temperature for the inverted magnetic field with positive collector voltage. Again, the current on the upstream RFA is not changed while changing the solenoidal field. The flux measured in the cold section shows no maximum at low magnetic fields and is decreased from $7.8 \cdot 10^{-8}$ A to $3.6 \cdot 10^{-8}$ A compared with that measured with the opposite magnetic field direction. In addition, the flux in the downstream section, which was increased in the previous measurement, is now decreased. Again, a temperature change of about 200 mK is observed.

In summary, the magnetic field in either direction clearly decreases the flux of electrons impinging on the chamber walls in the cold section. In the warm sections, only the downstream RFA is affected by the solenoid. The upstream RFA is too far away from the solenoid to show changes in the flux from the (axial) magnetic field. For positive particles, the influence in the cold section is not so strong and there is no visible influence on the flux in the warm sections. Depending on the magnetic field orientation, the flux is either decreased or slightly increased. The small influence on the liner temperature of around 200-300 mK in all four cases is negligible compared to the total temperature increase due to the beam current.

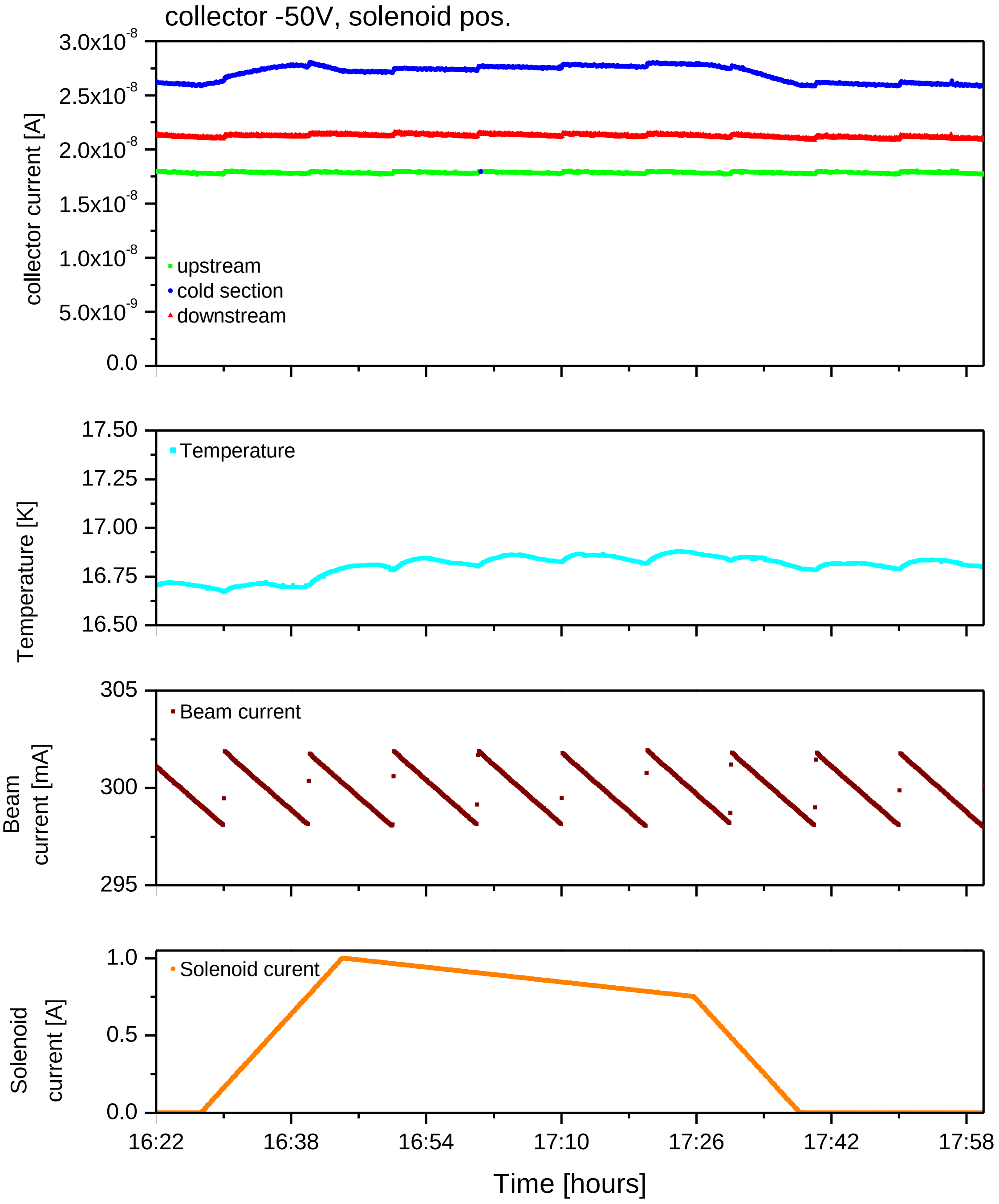

Figure 5.21: Influence of the axial magnetic field produced by the solenoid on the particle flux and the liner temperature. The collector is negatively biased.

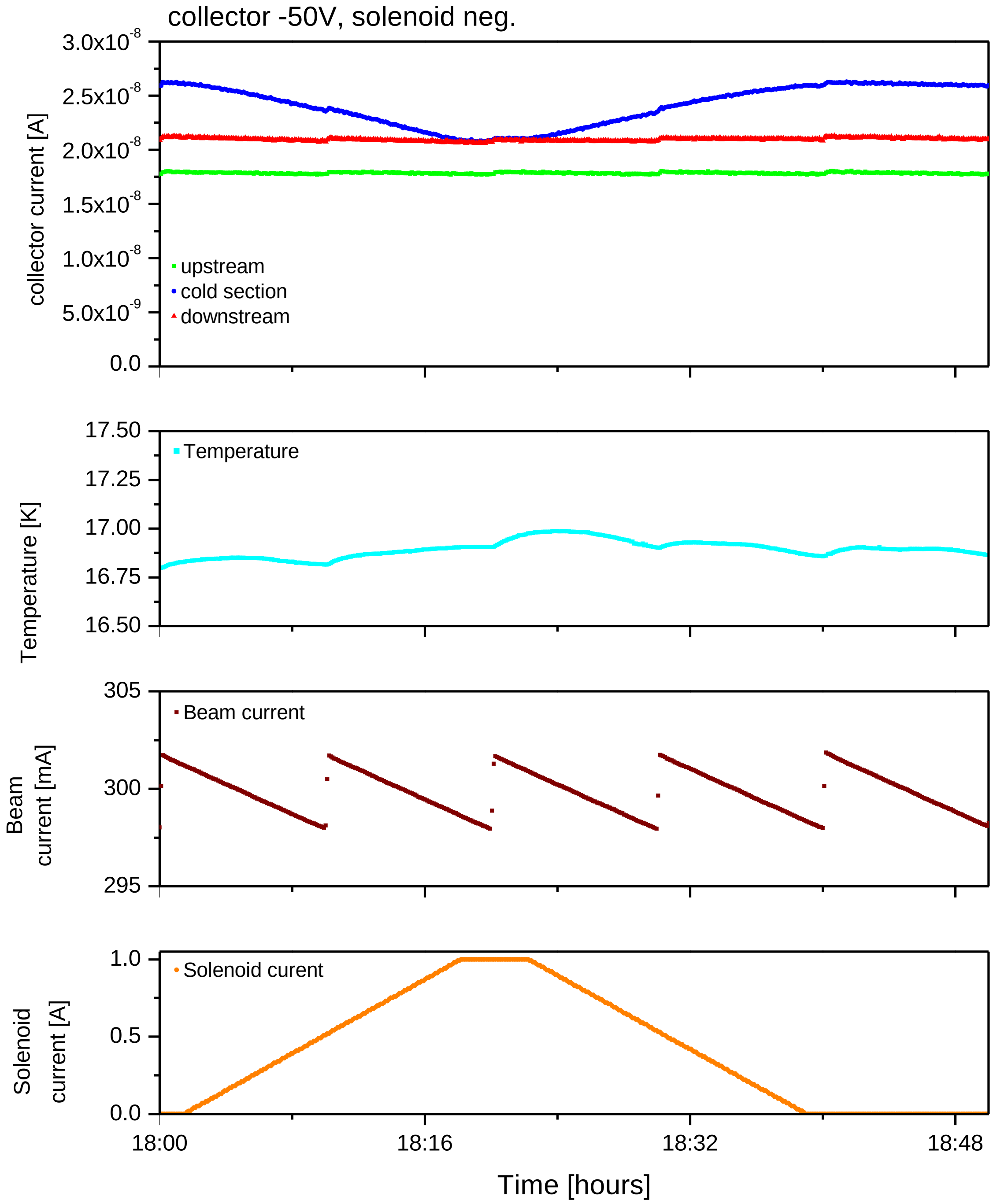

Figure 5.22: Influence of the axial magnetic field produced by the solenoid on the particle flux and the liner temperature. The collector is negatively biased and the axial magnetic field inverted with respect to Fig. 5.21.

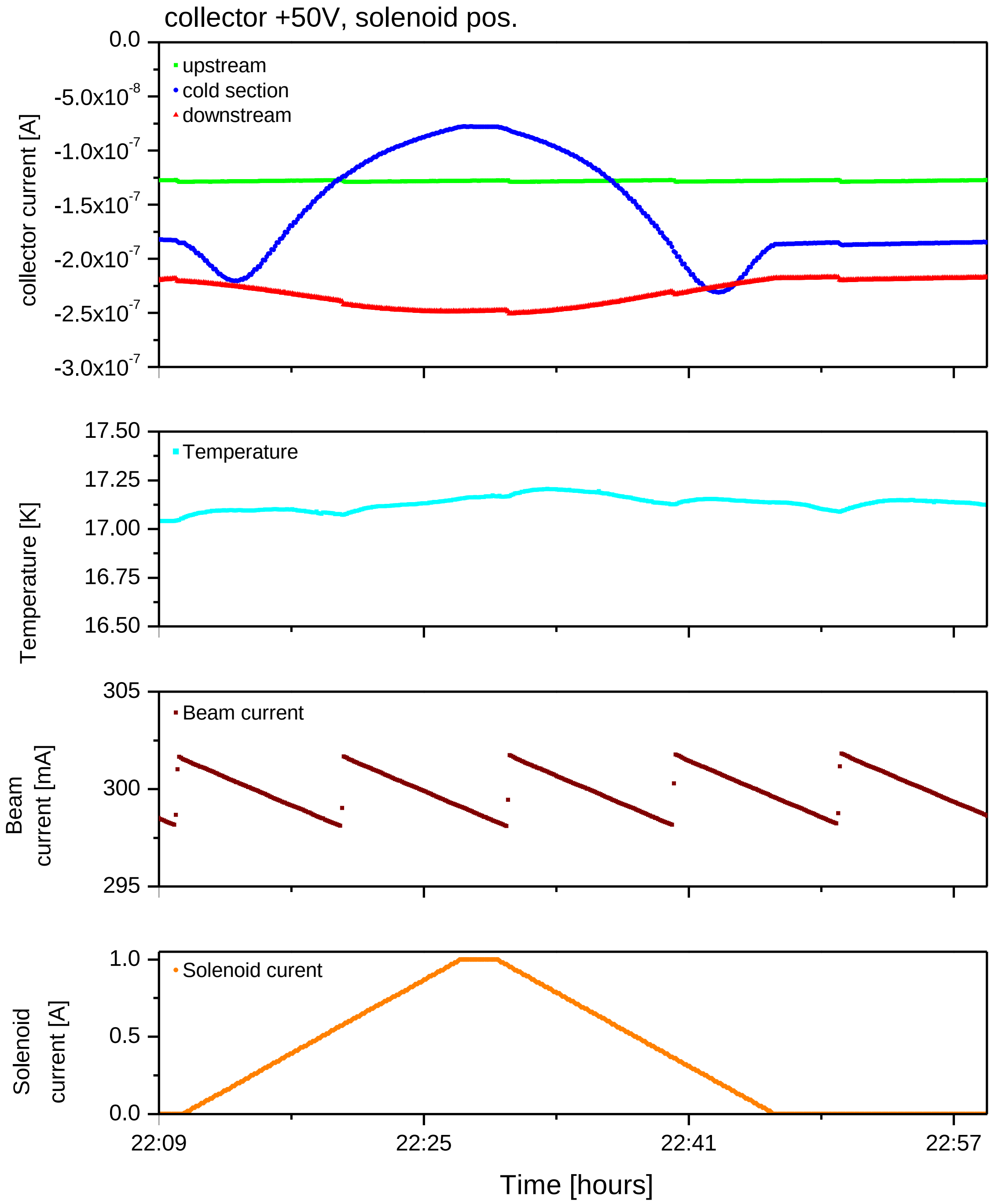

Figure 5.23: Influence of the axial magnetic field produced by the solenoid on the particle flux and the liner temperature. The collector is positively biased.

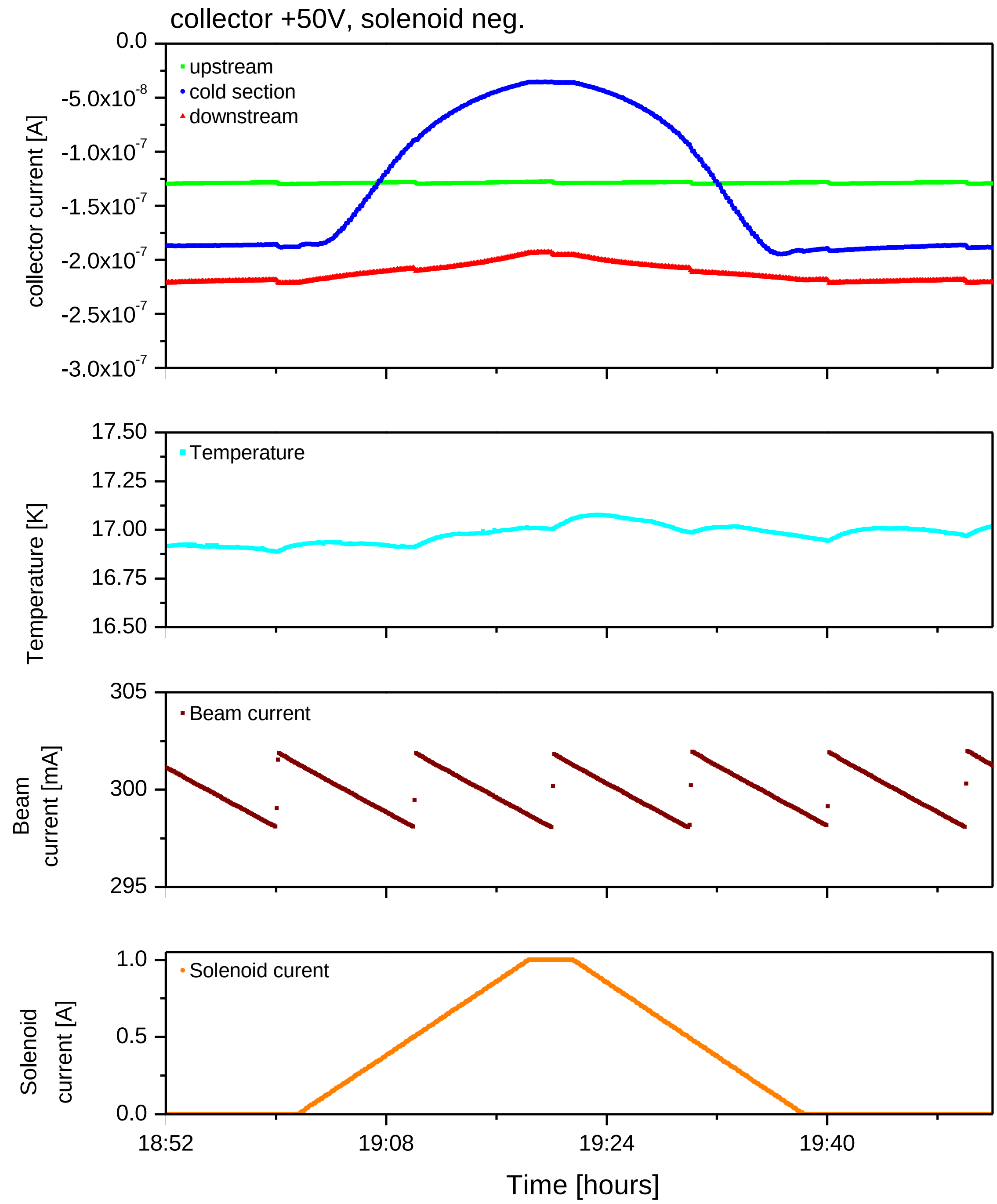

Figure 5.24: Influence of the axial magnetic field produced by the solenoid on the particle flux and the liner temperature. The collector is positively biased and the axial magnetic field inverted with respect to Fig. 5.23.

5.4 Total pressure and residual gas content

COLDDIAG is equipped with three inverted magnetron pressure gauges and three residual gas analysers, one in each diagnostic port (see Sec. 4.4.3). In addition, one gauge is located upstream and one downstream from COLDDIAG in the pumping section of the storage ring. In the sections below, the total pressure during a beam current ramp as well as during user run is presented. Finally, the residual gas content with and without beam is shown.

5.4.1 Total pressure

Figure 5.25 shows the pressure on the five gauges located in the straight section as a function of the beam current. The measurement was performed with 3 GeV and 460 consecutive bunches separated by 2 ns. The pressure measured in the upstream pumping section has a linear dependence on the beam current, in contrast to the pressure measured with the other gauges. This linear behavior is typical for photodesorption. To screen COLDDIAG from the direct synchrotron radiation created by the upstream bending magnet, a taper is installed between the upstream pumping station and the cryostat (see Sec. 3.1). The non-linear pressure increase after the taper demonstrates that the shading is sufficient and no direct synchrotron radiation is hitting the liner of COLDDIAG. Direct synchrotron radiation can therefore be excluded as the dominant beam heat load source in COLDDIAG. However, reflected synchrotron radiation might fill the vacuum chamber without being the dominating mechanism of molecule desorption.

The pressure measured in COLDDIAG during the user run from September to December 2012 can be seen in Fig. 5.26. The upstream warm section shows the highest pressure followed by the downstream warm section, while the cold section exhibits the lowest pressure. During the user run, the pressure is improving in all three sections. The pressure spikes visible in the plots are measured after the machine development days and after the November shutdown, which is indicated by the axis break. In the periods without beam or low beam currents, the cold liner section in COLDDIAG acts as a cryopump. When beam is restored to user conditions, the cryosorbed gas layers are released into the vacuum by photodesorption and thermal desorption, creating pressure spikes in the cold section.

An influence of the pressure or of the cryosorbed gas layer on the beam heat load could not be observed. This might be due to the fact that the pressure spikes have a very short time constant, which is much shorter than the time needed to reach thermal equilibrium and to measure the beam heat load. In addition, the pressure variation during user run is not very large and all effects caused by the pressure might therefore be hidden by effects which have a larger impact on the beam heat load such as different beam currents or different fill patterns.

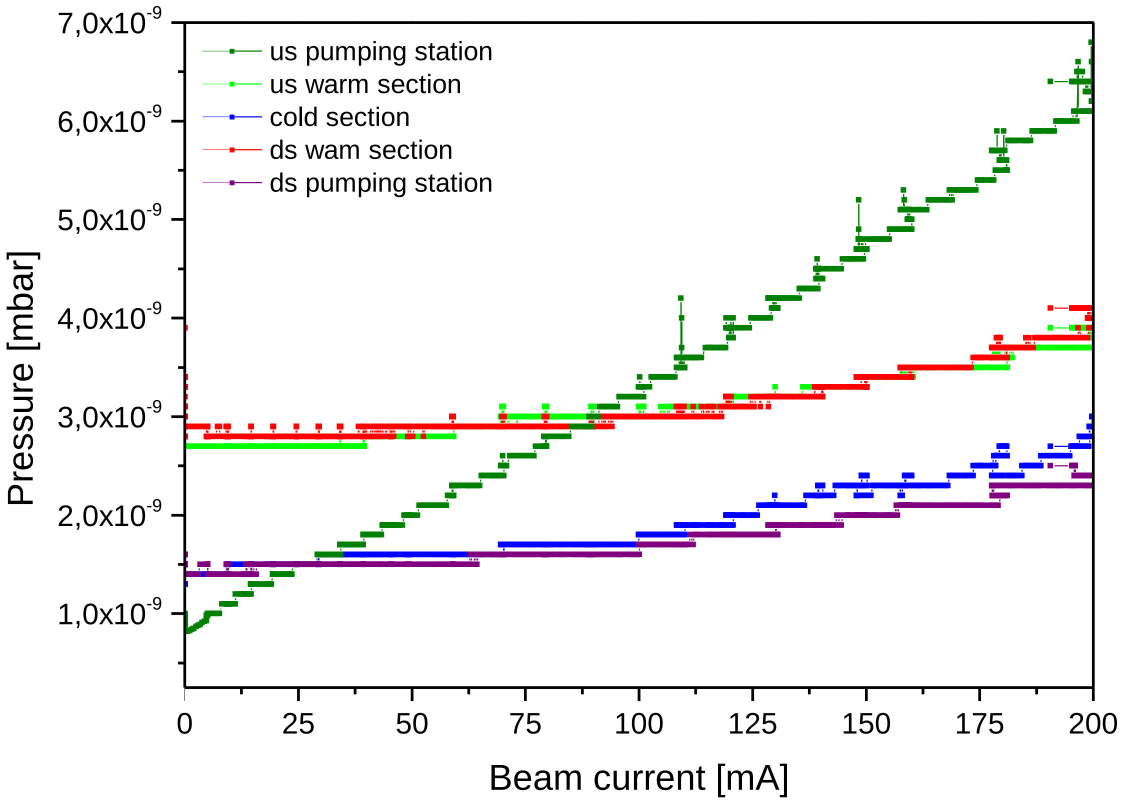

Figure 5.25: Pressure in the COLDDIAG straight section as a function of beam current, with a fill pattern of 460 consecutive bunches.

5.4.2 Residual gas content with and without beam

Figure 5.27 shows the typical residual gas content measured with the three RGAs installed upstream, downstream, and in the cold section of COLDDIAG, with and without beam. The selected spectra show only the range from 0 to 50 amu, as no masses have been detected above this. Similar to what can be seen in Fig. 5.25 and Fig. 5.26, the upstream section reveals the highest pressure, followed by the downstream section, while the lowest pressure is observed in the cold section. The residual gas measured in all three sections exhibits an analogue composition dominated by hydrogen with the main peak at 2 amu and followed by water indicated by the peak at 18 amu. The presence of water is due to the fact that COLDDIAG is not baked. Baking has not been performed to avoid any influence on the purity of the electroplated copper layer on the liner. The relatively high values obtained for carbon monoxide and nitrogen, both with the main peak at 28 amu, as well as oxygen at 32 amu, typically indicate an air leak. However, the COLDDIAG UHV chamber was leak checked several times ad no leak could be found above the detection limit of the leak detector which is $1 \cdot 10^{-12}$ mbar · l/s. This means that the peaks are due to virtual leaks caused by trapped volumes badly pumped inside the cold section, such as the volume between the six-way cold cross and the cold liner section (see Sec. 4). A comparison of the gas content with and without beam shows that the partial pressure of all gases increases almost equally and no particular gas is accumulating.

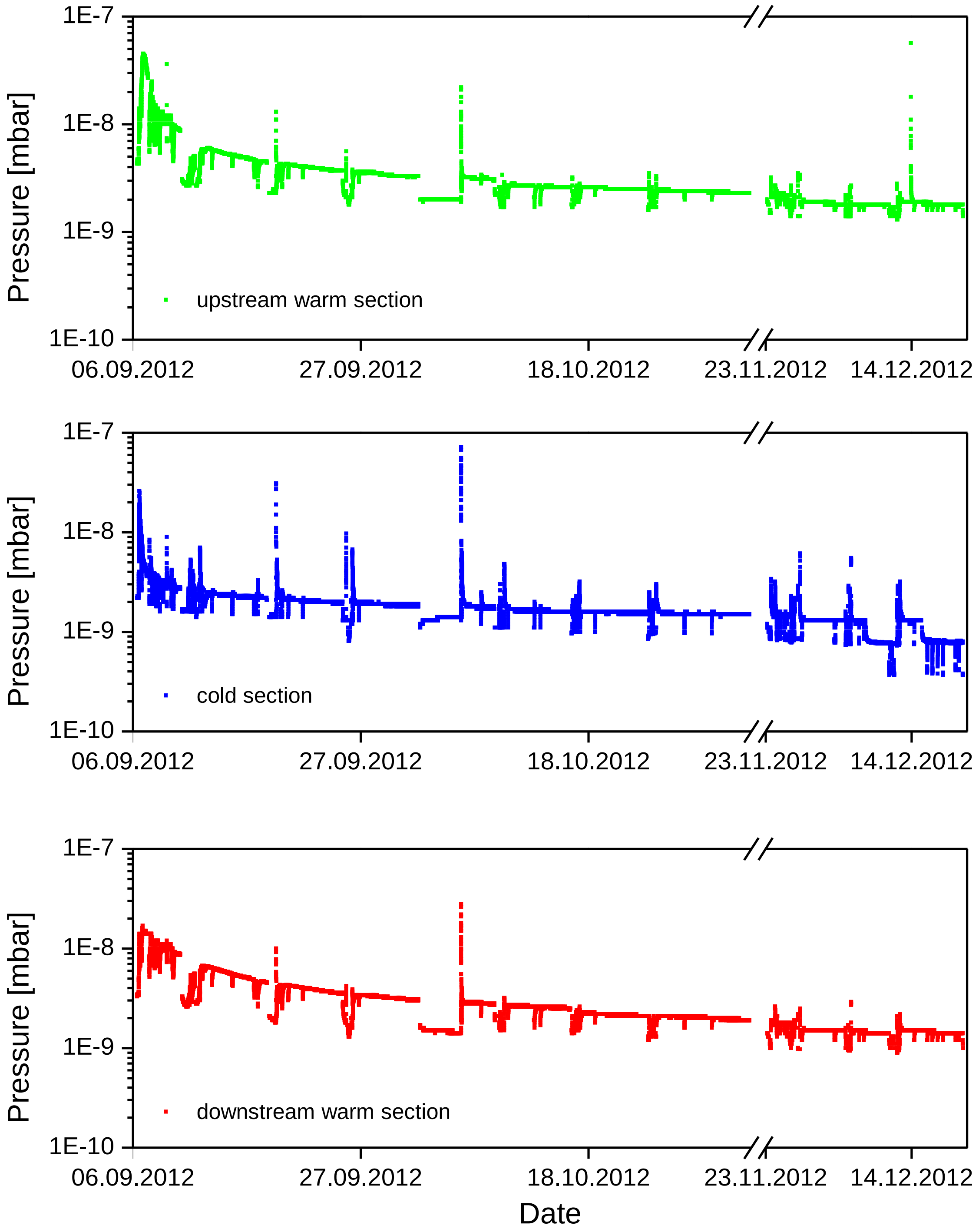

Figure 5.26: Pressure in COLDDIAG as a function of beam current during the user run from September to December 2012.

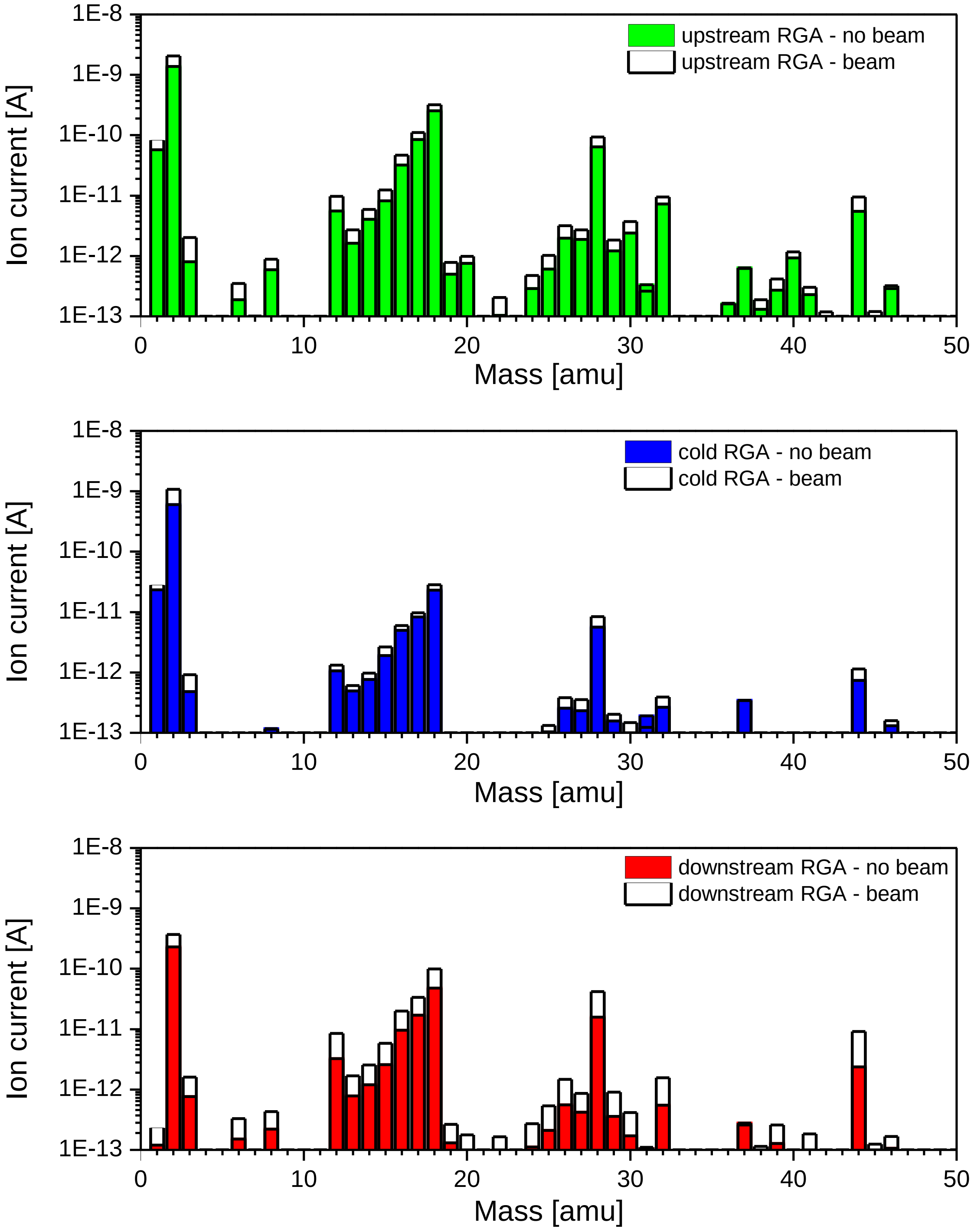

Figure 5.27: Mass spectra measured with the three RGAs installed in the upstream, downstream and cold section of COLDDIAG, with and without beam.

5.5 Discussion and concluding remarks

Good agreement is observed between the measurements performed in 2011 and with the redesigned thermal transition in 2012.

The overall beam heat load of up to 12 W with a beam current of 300 mA and a fill pattern of 686 consecutive bunches measured in the cold liner section is more than one order of magnitude larger than the theoretical predictions for COLDDIAG from resistive wall heating ranging from 0.1 W for a RRR of 200 to 0.2 W for a RRR of 10 (see Sec. 3.2.2). Even though the amount of heat load measured could be around 1.8 W higher than the real beam heat load, due to some heat intake from the new thermal transition (see Sec. 5.1.7). The beam heat load of around 3.2 W measured in the upstream warm section during the user run with a fill pattern of 686 consecutive bunches for a beam current of 300 mA and of around 2.8 W measured during the user run with a fill pattern of 900 consecutive bunches and the same beam current is also much higher than expected from theory.

Assuming resistive wall impedance is the main source of heat load, the heating is proportional to the length of the vacuum chamber (see Sec. 3.2.2). In this case, the beam heat load to the cold and the warm liner sections can be compared after rescaling the measured values of the 0.27 m long warm sections to the length of the 0.5 m long cold section. The resulting beam heat load of 5.9 W in the warm section is still around half the value of the 12 W measured in the cold section for a fill pattern of 686 consecutive bunches and 300 mA beam current. The 5.2 W obtained after rescaling for a fill pattern with 900 consecutive bunches and a beam current of 300 mA in the warm section, is almost half of the 8.9 W measured for the beam heat load in the cold section. However, because of the better electrical conductance at cryogenic temperatures, a lower heat load in the cold section than in the warm section for resistive wall heating is predicted.

Besides the discrepancy in the magnitude of heat load expected from impedance effects, the higher beam heat load measured at cryogenic temperatures compared with room temperature, the non linear dependence on the inverse number of bunches (see Sec. 5.1.4), the squared beam current (see Sec. 5.1.2) and the bunch length (see Sec. 5.1.5) do all point towards something other than resistive wall heating as the dominant heat source.

The electron energy spectrum measured in the cold section, the flux and solenoid measurements are not sufficient to explain the heat load via electron and/or ion bombardment. However, only a fraction of the electrons hitting the wall might be detected. Also of note is the observed dependence of the electron flux on the bunch spacing which is not expected for electrons generated by synchrotron radiation (see Sec. 3.1) and can only be related to beam dynamics effects.

The measurements performed with the total pressure gauges show that the background pressure in front of the radiation mask is dominated by photodesorption. The gauges in COLDDIAG do not indicate any pressure dependence typical for direct synchrotron radiation. However, reflected synchrotron radiation might fill the vacuum chamber, without being the dominant mechanism of molecule desorption.

6

Chapter 6

Summary

Nowadays, the demand for high intensities at short wavelength at electron storage rings is constantly growing. A possibility to fulfill these requirements is the use of superconducting insertion devices. However, the heat intake from the beam which is crucial for the cryogenic design of these devices can still not be predicted as the beam heat load mechanism is not fully understood. Within the framework of this thesis, a cryogen-free cryostat built by the company Babcock Noell GmbH was equipped with diagnostic instrumentation and commissioned. This cryostat was installed at the DLS to measure the beam heat load created by an electron beam on a cold bore in a storage ring.

The diagnostic instrumentation and in particular the heaters and wiring inside the UHV was adapted and had to be developed to be compatible with vacuum and radiation requirements. A gas injection system capable of injecting various small amounts of gases into the UHV of COLDDIAG and a new readout for the retarding field analysers using a lockin-amplifier were developed within this work. To operate the experiment and for data acquisition a LabVIEW™ based control system interacting with the control system of the storage ring of the DLS was programmed.

COLDDIAG was briefly installed in November 2011 in the storage ring of DLS and had to be removed due to a failure of the thermal transitions to the cold liner section. A mechanically more rigid design, which ensures a good electrical contact and still maintains a relatively low thermal conductivity, was developed. The new design introduced a soft soldering step under vacuum into the assembly of the thermal transition. The UHV compatibility of the new pieces was demonstrated and COLDDIAG was reassembled and reinstalled after some other modifications less than one year after the first failure in August 2012.

While COLDDIAG was installed in November 2011 and from August to December 2012 at the DLS, the beam heat load was measured under different beam conditions, including variable beam current, bunch length, beam position and fill pattern. The flux of charged particles impinging on the chamber walls and for electrons the energy spectrum were determined. With the installed solenoid the influence of an axial magnetic field produced by a solenoid on these particles was investigated. Additionally, the residual gas content and the total pressure were measured during the time COLDDIAG was installed.

The measured beam heat load in the cold and in the warm sections of the COLDDIAG setup is much higher than expected from theoretical models. Furthermore, none of the measured dependencies of the heat load on the fill pattern, the bunch current, or the bunch length fit any of the theoretical predictions. The measurements of the beam heat load, as well as the measured total pressure indicate that direct synchrotron radiation from upstream magnets is not the main source of beam heat load. The measured electron energy spectra and total flux are not sufficient for explaining the heat load by electron and/or ion bombardment, though only a fraction of the particles accelerated towards the chamber walls may have been detected. The discrepancies between theory and measurements are still not understood. More work is needed on both the experimental as well as the theoretical side to understand the beam heat load on a cold bore.

Outlook

More experiments are needed to understand the beam heat loads measured with COLDDIAG.

To do so, a software PID control loop was implemented into the control system to maintain a constant temperature on the liner. This will also allow the beam heat load to be measured at different liner temperatures. In this way, additional information about the influence of the cryosorbed gas layer and/or the importance of the conductance of the liner can be gathered.

To investigate the influence of the bunch length in a more controlled way, measurements at constant beam current and different cavity voltages are planned.

In addition, higher beam currents particularly in for the fill patterns with a small number of bunches can provide more information about the beam heat load at high bunch currents.

Furthermore, the influence of the new thermal transition on the measured heat load needs to be investigated more closely. With this aim, offline calibrations after the implementation of additional heaters in the thermal transition region are foreseen.

A controlled increase of the pressure by switching off the ion pumps in the straight section or the injection of different gases like hydrogen, carbon monoxide, carbon dioxide or methane, might give a better understanding of the impact of the residual pressure and cryosorbed gas layer on the beam heat load.

More theoretical work will also be carried out in parallel.

Bibliography

[1] F. Elder, A. Gurewitsch, R. Langmuir, and H. Pollock. Radiation from electrons in a synchrotron. *Physical Review*, 71(11):829–830, 1947. ISSN 0031-899X. doi: 10.1103/PhysRev.71.829.5. (Cited on page 1)

[2] A. C. Thompson, D. Attwood, E. Gullikson, M. Howells, K.-J Kim, J. Kirz, J. Kortright, I. Lindau, Y. Liu, P. Pianetta, A. Robinson, J. Scofield, J. Underwood, G. Williams, and H. Winick. *X-ray data booklet*. Lawrence Berkeley National Laboratory, University of California Berkeley, CA, 2009. (Cited on page 1)

[3] P. Willmott. *An introduction to synchrotron radiation: Techniques and applications*. Wiley, Chichester and West Sussex and U.K, 2011. ISBN 9781283177726. (Cited on page 1)

[4] ESRF. Id2 scientific and industrial applications, 2013. URL `http://www.esrf.eu/UsersAndScience/Experiments/SoftMatter/ID02/ScientificApplications`. (Cited on page 1)

[5] T. Narayanan, O. Diat, and P. Bösecke. Saxs and usaxs on the high brilliance beamline at the esrf. *Nuclear Instruments and Methods in Physics Research Section A: Accelerators, Spectrometers, Detectors and Associated Equipment*, 467–468, Part 2(0):1005–1009, 2001. doi: 10.1016/S0168-9002(01)00553-8. URL `http://www.sciencedirect.com/science/article/pii/S0168900201005538`. (Cited on page 1)

[6] J. Chavanne and P. Elleaume. Latest developments on insertion devices. In *Proceedings of EPAC,(Edinburgh)*, page 969, 2006. (Cited on pages 1 and 8)

[7] T. Hara, T. Tanaka, H. Kitamura, T. Bizen, X. Maréchal, T. Seike, T. Kohda, and Y. Matsuura. Cryogenic permanent magnet undulators. *Physical Review Special Topics - Accelerators and Beams*, 7(5), 2004. ISSN 1098-4402. doi: 10.1103/PhysRevSTAB.7.050702. (Cited on pages 1 and 8)

[8] J. Chavanne, M. Hahn, R. Kersevan, C. Kitegi, C. Penel, F. Revol, and ESRF Grenoble France. Construction of a cryogenic permanent magnet undulator at the esrf. In *Proceedings of EPAC, 2008*, pages 2243–2245, 2008. (Cited on pages)

[9] S. Casalbuoni, T. Baumbach, S. Gerstl, A. Grau, M. Hagelstein, T. Holubek, D. Saez de Jauregui, C. Boffo, and W. Walter. Development of superconducting undulators at

anka. *Synchrotron Radiation News*, 24(3):14–19, 2011. doi: 10.1080/08940886.2011.583885. (Cited on pages 1, 8, and 9)

[10] A. Bernhard, S. Casalbuoni, R. Frahm, B. Griesebock, U. Haake, M. Hagelstein, M. Kläser, B. Kostka, A.S Müller, R. Rossmanith, Th Schneider, F. Schoeck, E. Steffens, M. Weisser, D. Wollmann, and T. Baumbach. Technical report: First beam tests of a superconductive undulator in a storage ring at anka. *Synchrotron Radiation News*, 19(3):9–17, 2006. doi: 10.1080/08940880600755194. (Cited on pages 2 and 9)

[11] A. Bernhard, S. Casalbuoni, R. Frahm, B. Griesebock, U. Haake, M. Hagelstein, B. Kostka, Y. L. Mathis, A. S. Müller, R. Rossmanith, F. Schock, E. Steffens, M. Weiber, D. Wollmann, and T. Baumbach. Performance of the first superconducting cold-bore undulator in an electron storage ring. *IEEE Transactions on Applied Superconductivity*, 17(2):1235–1238, 2007. ISSN 1051-8223. doi: 10.1109/TASC.2007.899029. (Cited on page 2)

[12] S. Casalbuoni, A. Grau, M. Hagelstein, R. Rossmanith, F. Zimmermann, B. Kostka, E. Mashkina, E. Steffens, A. Bernhard, D. Wollmann, et al. Beam heat load and pressure rise in a cold vacuum chamber. *Physical Review Special Topics-Accelerators and Beams*, 10(9):093202, 2007. (Cited on pages 2, 10, and 16)

[13] S. Casalbuoni, A. Grau, M. Hagelstein, R. Rossmanith, F. Zimmermann, B. Kostka, E. Mashkina, E. Steffens, A. Bernhard, D. Wollmann, et al. Beam heat load measurements in the cold bore superconductive undulator in anka. *Nuclear Instruments and Methods in Physics Research Section A: Accelerators, Spectrometers, Detectors and Associated Equipment*, 582(1):34–36, 2007. (Cited on pages 2 and 15)

[14] S. Casalbuoni, T. Baumbach, A. Grau, M. Hagelstein, R. Rossmanith, Forschungszentrum Karlsruhe, V. Baglin, B. Jenninger, R. Cimino, M. Cox, et al. Design of a cold vacuum chamber for diagnostics. In *Proceedings of EPAC, 2008*, page 2240, 2008. (Cited on pages 2, 10, 19, and 20)

[15] J. D. Jackson. *Classical electrodynamics*. Wiley, New York, 3 edition, 1999. ISBN 9780471309321. (Cited on page 3)

[16] V. C. Kempson et al. Diamond light source: Moving from commissioning to full machine operation. In *Proceedings of EPAC, 2008*, volume 8, page 2051, 2008. (Cited on page 4)

[17] R. P. Walker et al. Overview of the status of the diamond project. In *Proceedings of EPAC,(Edinburgh)*, pages 2718–2722, 2006. (Cited on page 4)

[18] I. P.S. Martin, C. P. Bailey, R. Bartolini, E. C. Longhi, and R. P. Walker. Top-up safety simulations for the diamond storage ring. In *Proceedings of EPAC, 2008*, 2008. (Cited on page 4)

[19] R. P. Walker et al. Recent developments at diamond light source. In *Proceedings of PAC,(Vancouver)*, 2009. (Cited on page 4)

[20] J. A. Clarke. *The science and technology of undulators and wigglers*. Oxford University Press, Oxford, 2004. ISBN 9780198508557. (Cited on pages 5, 6, and 7)

[21] K. Wille. *Physik der Teilchenbeschleuniger und Synchrotronstrahlungsquellen: Eine Einführung*. Teubner, Stuttgart, 2 edition, 1996. ISBN 9783519130871. (Cited on page 6)

[22] C. Benabderrahmane, P. Berteaud, N. Bechu, M.E Couprie, J.M Filhol, et al. Development of cryogenic undulator cpmu at soleil. *Conf.Proc.*, 0806233:WEPC098, 2008. (Cited on page 8)

[23] S. Sasaki, M. Petra, I. B. Vasserman, Ch L. Doose, E. R. Moog, and N. V. Mokhov. Radiation damage to advanced photon source undulators. In *Proceedings of the Particle Accelerator Conference, 2005*, pages 4126–4128, 2005. (Cited on page 9)

[24] P. Elleaume, J. Chavanne, and B. Faatz. Design considerations for a 1å sase undulator. *Nuclear Instruments and Methods in Physics Research Section A: Accelerators, Spectrometers, Detectors and Associated Equipment*, 455(3):503–523, 2000. (Cited on page 9)

[25] S. Prestemon, D. Arbelaez, T. Koettig, A. Madur, S. Marks, and D. Schlueter. Development of superconducting undulators. In *Proceedings of the 33rd Free Electron Laser Conference, 2011*, volume 33, 2011. (Cited on page 9)

[26] M. Tavlet. Aging of organic materials around high-energy particle accelerators. *Nuclear Instruments and Methods in Physics Research Section B: Beam Interactions with Materials and Atoms*, 131(1–4):239–244, 1997. ISSN 0168-583X. doi: 10.1016/S0168-583X(97)00151-1. URL `http://www.sciencedirect.com/science/article/pii/S0168583X97001511`. (Cited on page 9)

[27] K. Humer, H. Schoenbacher, B. Szeless, M. Tavlet, and H. W. Weber. Radiation tests at cryogenic temperature on selected organic materials for lhc. *Advances in cryogenic engineering*, 42:219–226, 1997. (Cited on page 9)

[28] Y. Ivanyushenkov, Ch L. Doose, J. Fuerst, Q. Hass, M. Kasa, V. Lev, N. Mezentsev, V. Syrovatin, E. Trakhtenberg, V. Tsukanov, I. Vasserman, and E. Gluskin. Development of a superconducting undulator for the aps. *Journal of Physics: Conference Series*, 425(3):032007, 2013. URL `http://stacks.iop.org/1742-6596/425/i=3/a=032007`. (Cited on page 9)

[29] S. Prestemon, D. Dietderich, S. Bartlett, M. Coleman, S. Gourlay, A. Lietzke, S. Marks, S. Mattafirri, R. Scanlan, R. Schlueter, B. Wahrer,

and B. Wang. Design, fabrication, and test results of undulators using<tex>*rmnb_3rmsn*</tex>superconductor. *IEEE Transactions on Appiled Superconductivity*, 15(2):1236–1239, 2005. ISSN 1051-8223. doi: 10.1109/TASC.2005.849540. (Cited on page 9)

[30] E. Mashkina, A. Grau, C. Boffo, M. Borlein, T. Baumbach, S. Casalbuoni, M. Hagelstein, R. Rossmanith, E. Steffens, and W. Walter. Test of an electromagnetic shimming concept for superconducting undulators. *Applied Superconductivity, IEEE Transactions on, title=Test of an Electromagnetic Shimming Concept for Superconducting Undulators*, 19(3):2329–2332, 2009. ISSN 1051-8223. doi: 10.1109/TASC.2009.2019038. (Cited on pages)

[31] D. Wollmann, A. Bernhard, P. Peiffer, T. Baumbach, E. Mashkina, A. Grau, and R. Rossmanith. Experimental demonstration of the induction-shimming concept in superconductive undulators. *Physical Review Special Topics - Accelerators and Beams*, 12 (4), 2009. ISSN 1098-4402. doi: 10.1103/PhysRevSTAB.12.040702. (Cited on pages)

[32] A. Madur, F. Trillaud, D. Dietderich, S. Marks, S. Prestemon, R. Schlueter, R. Garrett, I. Gentle, K. Nugent, and S. Wilkins. Superconducting switch concept applied to superconducting undulator phase-error correction. *AIP Conference Proceedings*, 1234 (1):552–555, 2010. doi: 10.1063/1.3463264. URL `http://link.aip.org/link/?APC/1234/552/1`. (Cited on page 9)

[33] E. Mashkina, A. Grau, Th Schneider, A. Bernhard, S. Casalbuoni, M. Hagelstein, B. Kostka, R. Rossmanith, E. Steffens, D. Wollmann, and T. Baumbach. Casper-a magnetic measurement facility for superconducting undulators. In *Journal of Physics: Conference Series*, volume 97, page 012020, 2008. (Cited on page 9)

[34] A. Grau, T. Baumbach, S. Casalbuoni, S. Gerstl, M. Hagelstein, and D. Saez de Jauregui. Instrumentation for local and integral field measurements of superconducting undulator coils. *Applied Superconductivity, IEEE Transactions on*, 21(3):2312–2315, 2011. (Cited on page 9)

[35] S. Casalbuoni, M. Hagelstein, B. Kostka, R. Rossmanith, M. Weisser, E. Steffens, A. Bernhard, D. Wollmann, and T. Baumbach. Generation of x-ray radiation in a storage ring by a superconductive cold-bore in-vacuum undulator. *Phys. Rev. ST Accel. Beams*, 9(1):010702, 2006. doi: 10.1103/PhysRevSTAB.9.010702. URL `http://link.aps.org/doi/10.1103/PhysRevSTAB.9.010702`. (Cited on page 9)

[36] S. Casalbuoni, M. Migliorati, A. Mostacci, L. Palumbo, and B. Spataro. Beam heat load due to geometrical and resistive wall impedance in colddiag. *Journal of Instrumentation*, 7(11):P11008, 2012. (Cited on pages 10, 12, 13, 20, and 68)

[37] E. Wallen and G. LeBlanc. Cryogenic system of the max-wiggler. *Cryogenics*, 44(12):879–893, 2004. ISSN 0011-2275. doi: 10.1016/j.cryogenics.

2004.06.003. URL http://www.sciencedirect.com/science/article/pii/S0011227504001547. (Cited on pages 11 and 14)

[38] A. Hofmann. Characteristics of synchrotron radiation; 1990 ed, 1989. (Cited on page 11)

[39] A. Chao and Wu. *Physics of collective beam instabilities in high energy accelerators.* Wiley, 1993. (Cited on page 12)

[40] L. Palumbo, V. G. Vaccaro, and M. Zobov. Wake fields and impedance. *Proceedings of CAS CERN Accelerator School CERN 95-06 (*, 1995. URL http://arxiv.org/pdf/physics/0309023. (Cited on pages 12 and 13)

[41] M. A. Furman, H. Lee, and B. Zotter. *Energy Loss of Bunched Beams in RF Cavities.* SSC Central Design Group, c/o Lawrence Berkely Laboratory, 1986. (Cited on page 12)

[42] R. M. Jones. Hom mitigation, 2010. URL http://cas.web.cern.ch/cas/Denmark-2010/Lectures/Jones-1.pdf. (Cited on page 13)

[43] A. Chao and M. Tigner. *Handbook of accelerator physics and engineering.* World Scientific, River Edge and N.J, 1999. ISBN 9789810238582. (Cited on page 13)

[44] K. L. F. Bane. Wakefields of sub-picosecond electron bunches. *International Journal of Modern Physics A*, 22(22):3736–3758, 2007. doi: 10.1142/S0217751X07037391. (Cited on page 13)

[45] G. V. Stupakov. Impedance of small obstacles and rough surfaces. *Phys. Rev. ST Accel. Beams*, 1(6):064401, 1998. doi: 10.1103/PhysRevSTAB.1.064401. URL http://link.aps.org/doi/10.1103/PhysRevSTAB.1.064401. (Cited on pages)

[46] A. Mostacci, F. Ruggiero, M. Angelici, M. Migliorati, L. Palumbo, and S. Ugoli. Wakefields due to surface waves in a beam pipe with a periodic rough surface. *Phys. Rev. ST Accel. Beams*, 5(4):044401, 2002. doi: 10.1103/PhysRevSTAB.5.044401. URL http://link.aps.org/doi/10.1103/PhysRevSTAB.5.044401. (Cited on page 13)

[47] G. Rehm. private communication, 2012. (Cited on page 13)

[48] W. Chou and F. Ruggiero. Anomalous skin effect and resistive wall heating, 1995. (Cited on pages 13 and 14)

[49] Ch Gerthsen and D. Meschede. *Gerthsen Physik.* Springer, Berlin and Heidelberg and New York and Barcelona and Hongkong and London and Mailand and Paris and Tokio, 22 edition, 2004. ISBN 3540026223. (Cited on page 14)

[50] N. W. Ashcroft and N. D. Mermin. *Solid state physics.* Holt, Rinehart and Winston, New York, 1976. ISBN 9780030493461. (Cited on page 14)

[51] D. Saez de Jauregui, T. Baumbach, S. Casalbuoni, A. Grau, S. Gerstl, M. Hagelstein, C. Heske, T. Holubek, B. Krause, A. Seiler, S. Stankov, L. Weinhardt, C. Boffo, C. Antoine, and Y. Boudigou. Characterization of vacuum chamber samples for superconducting insertion devices. In *Proceedings of the International Particle Accelerator Conference (IPAC)*, 2012. (Cited on page 14)

[52] A. B. Pippard. The surface impedance of superconductors and normal metals at high frequencies. ii. the anomalous skin effect in normal metals. *Proceedings of the Royal Society A: Mathematical, Physical and Engineering Sciences*, 191(1026):385–399, 1947. ISSN 1364-5021. doi: 10.1098/rspa.1947.0122. (Cited on page 14)

[53] H. London. The high-frequency resistance of superconducting tin. *Proceedings of the Royal Society A: Mathematical, Physical and Engineering Sciences*, 176(967):522–533, 1940. ISSN 1364-5021. doi: 10.1098/rspa.1940.0105. (Cited on page 14)

[54] G. E. H. Reuter and E. H. Sondheimer. The theory of the anomalous skin effect in metals. *Proceedings of the Royal Society A: Mathematical, Physical and Engineering Sciences*, 195(1042):336–364, 1948. ISSN 1364-5021. doi: 10.1098/rspa.1948.0123. (Cited on page 14)

[55] R. G. Chambers. The anomalous skin effect. *Proceedings of the Royal Society A: Mathematical, Physical and Engineering Sciences*, 215(1123):481–497, 1952. ISSN 1364-5021. doi: 10.1098/rspa.1952.0226. (Cited on page 14)

[56] V. Baglin. Cold/sticky systems. In D. Brandt, editor, *CAS CERN Accelerator School, vacuum in accelerators*, volume 2007-003 of *CERN*, page 18 p, Geneva, 2007. CERN. ISBN 9290832940. (Cited on page 15)

[57] K. Harkay and R. Rosenberg. Properties of the electron cloud in a high-energy positron and electron storage ring. *Physical Review Special Topics - Accelerators and Beams*, 6(3), 2003. ISSN 1098-4402. doi: 10.1103/PhysRevSTAB.6.034402. (Cited on page 15)

[58] M. A. Furman. Electron-cloud build-up: Summary. In *Proceedings of ECLOUD 07, Daegu, S. Korea*, 2007. (Cited on page 15)

[59] S. Casalbuoni, S. Schleede, D. Saez de Jauregui, M. Hagelstein, and P. F. Tavares. Can electron multipacting explain the pressure rise in a cold bore superconducting undulator? *Physical Review Special Topics - Accelerators and Beams*, 13(7), 2010. ISSN 1098-4402. doi: 10.1103/PhysRevSTAB.13.073201. (Cited on page 15)

[60] O. Grobner. Beam induced multipacting. In *Particle Accelerator Conference, 1997. Proceedings of the 1997*, volume 3, pages 3589–3591, 1997. (Cited on pages 15 and 16)

[61] Bilfinger Berger. Babcock noell gmbh, 2013. URL `http://www.bng.bilfinger.com/fahrenheit/index.php?lang=de`. (Cited on page 17)

[62] CST - Computer Simulation Technology AG. Cst particle studio, 2012. URL `https://www.cst.com/Content/Products/PS/Overview.aspx`. (Cited on page 20)

[63] Babcock Noell GmbH. Drawing is based on a picture from the technical design review of colddiag, 2010. (Cited on pages 22, 24, 25, 26, 27, 28, 30, and 103)

[64] Agilent Technologies. Vacion plus 150, 2013. URL `http://www.chem.agilent.com/en-US/products-services/Instruments-Systems/Vacuum-Technologies/High-Vacuum-Pumps/VacIon-Plus-150/Pages/default.aspx`. (Cited on page 21)

[65] Ltd Sumitomo Heavy Industries. Shi cryogenics group - 4k cryocoolers, 2013. URL `http://www.shicryogenics.com/index.php?option=com_content&task=blogcategory&id=22&Itemid=169`. (Cited on pages 23 and 103)

[66] V. Baglin, I. R. Collins, and B. Jenninger. Performance of a cryogenic vacuum system (coldex) with an lhc type beam. *Vacuum*, 73(2):201–206, 2004. ISSN 0042-207X. doi: 10.1016/j.vacuum.2003.12.005. URL `http://www.sciencedirect.com/science/article/pii/S0042207X03002288`. (Cited on page 24)

[67] Tektronix GmbH. Keithley instruments inc., 2013. URL `http://www.keithley.de/`. (Cited on page 32)

[68] D. Saez de Jauregui, S. Casalbuoni, A. Grau, M. Hagelstein, Forschungszentrum Karlsruhe, R. Cimino, M. Commisso, E. Mashkina, and R. Weigel. Spectrum of the low energy electrons bombarding the wall in the anka storange ring. In *Proceedings of PAC,(Vancouver)*, 2009. (Cited on pages 32 and 77)

[69] AMETEK Inc. Homepage, 2013. URL `http://www.signalrecovery.com/`. (Cited on page 32)

[70] Pfeiffer Vacuum. Prismaplus™ qmg 220 m mit c-sem-detektor, 2013. URL `http://www.pfeiffer-vacuum.de/produkte/analysegeraete/restgasanalyse/restgasanalyse-im-ultrahochvakuum/prismaplus-qmg-220-m-mit-c-sem-detektor`. (Cited on page 34)

[71] VSE VacuumTechnology. Vse vacuumtechnology, 2008. URL `http://www.vseworld.com/leakvalve_highlights.html`. (Cited on page 34)

[72] Lakeshore. Home | lake shore cryotronics, inc., 2013. URL `http://www.lakeshore.com/Pages/Home.aspx`. (Cited on page 35)

[73] J. E. Jensen, R. B. Stewart, and W. A. Tuttle. *Selected cryogenic data notebook*. Brookhaven National Laboratory, Bubble Chamber Group, 1966. (Cited on pages 37 and 50)

[74] Gamma Vaccum. Ion pumps : Ultra high vacuum : Xhv : Uhv: Gammavacuum.com, 2013. URL `http://www.gammavacuum.com/`. (Cited on page 48)

[75] R. Bartolini. Head of accelarator physics group, diamond light source, private communication, 2012. (Cited on pages 63 and 67)

[76] C. Thomas. Beam diagnostics group, diamond light source, personal communication, 2012. (Cited on pages 63 and 67)

List of Figures

Danksagung

Am Ende dieser Arbeit möchte mich bei allen bedanken die in irgendeiner Form zum Gelingen beigetragen haben. Mein ganz besonderer Dank gilt hierbei:

- Herrn Prof. T. Baumbach für die Möglichkeit diese Arbeit an seinem Institut anzufertigen.
- Frau Prof. A.–S. Müller für die spontane und nette Übernahme des Korreferats.
- Sara für die nette Betreuung und die zahlreichen Diskussionen während dieser Arbeit.
- Matthew Cox and Richard Walker to make it possible to install COLDDIAG at Diamond.
- Günther Rhem, Riccardo Bartolini and all the others for the fruitful discussion during the COLDDIAG meetings.
- Tobi, Hugo, Sol and Andy for the accommodation in the office and the very nice atmosphere, which made my stay at Diamond a pleasure.
- The Diamond vacuum group and especially Richard and Bill for their help during installation.
- Emily for the nice time and support during my stay and the help while tightening the impossible screw.
- Jim Clarke for providing some of the parts of the vacuum equipment.
- Bruno Spataro, Andrea Mostacci and Mauro Migliorati for the Impedance calculations for COLDDIAG.
- Prof. Dr. Hilbert v. Löhneysen und besonders Oliver Berg für die Untertützung bei der Kalibrierung der Temperatursensoren.
- Der Institutswerkstatt und besonders Sven für das Herstellen meiner beliebten ”Sonderteile”.
- Andreas Völker und Tomas Fischböck für die Unterstützung bei allen Vakuumbelangen.

- Robert für die Weiterführung des Projekts in England während des Zusammenschreibens.
- Andreas für die Milch und die Hilfe beim Zusammensetzen des Cryostaten.
- David für die Warnung... (auch wenn ich sie nie ernstgenommen habe) und die vielen abendlichen Diskussionen.
- Den Mitarbeitern der Firma Babcock Noell GmbH für ihre nette Arbeitsumbegung beim Zusammenbau des Cryostaten.
- Günther für die unzähligen Stunden die wir zusammen vor der Werksabnahme in Würzburg verbracht haben, um den Kryostaten fertig zu bekommen und die unvergesslichen Diskussionen bei den anschließenden Abendessen. Und am Ende wird alles gut...
- Johanna dafür, dass du nur manchmal auf COLDDIAG eifersüchtig warst und mich immer bedingungslos unterstützt hast.

- Zuletzt möchte ich mich auch beim Karlsruhe House of Young Scientists (KHYS) für die Förderung des Auslandsaufenthalt an der Diamond Light Source bedanken.